Deuterium and Helium Retention in ITER Specification Tungsten before and after Plastic Deformation

Deuterium- en heliumretentie in wolfraam naar ITER-specificatie, voor en na plastische vervorming

Anastasiia Bakaeva

Promotoren: prof. dr. ir. J.-M. Noterdaeme, dr. D. Terentyev
Proefschrift ingediend tot het behalen van de graad van
Doctor in de ingenieurswetenschappen: toegepaste natuurkunde

UNIVERSITEIT
GENT

Vakgroep Toegepaste Fysica
Voorzitter: prof. dr. ir. C. Leys
Faculteit Ingenieurswetenschappen en Architectuur
Academiejaar 2018 - 2019

ISBN 978-94-6355-179-3
NUR 971
Wettelijk depot: D/2018/10.500/97

Members of the examination board

Chairman:	**em. prof. Hendrik Van Landeghem** Ghent University, Belgium
Secretary:	**prof. dr. Roumen Petrov** Ghent University, Belgium
Reading committee:	**prof. dr. ir. Dagmar D'hooge** Ghent University, Belgium
	prof. dr. Igor E. Garkusha Kharkov Institute of Physics and Technology, Ukraine
	prof. dr. Evgeny E. Zhurkin Peter the Great St. Petersburg Polytechnic University, Russia
	dr. Yevhen Zayachuk University of Oxford, United Kingdom
Further members of the examination board:	**prof. dr. ir. Jean-Marie Noterdaeme** Ghent University, Belgium
	dr. Dmitry Terentyev SCK•CEN, Belgium

This research was performed at the
Belgian nuclear research centre SCK·CEN
in collaboration with Ghent University

SCK·CEN
Nuclear Materials Science Institute
Boeretang 200
2400, Mol
Belgium

Ghent University
Faculty of Engineering and Architecture
Department of Applied Physics
St. Pietersnieuwstraat 33
9000, Ghent
Belgium

Table of Contents

Acknowledgements ..... **i**

List of the symbols and abbreviations ..... **iii**

List of publications ..... **v**

English summary ..... **vii**

Nederlandse samenvatting (Dutch summary) ..... **xi**

1. Introduction **1**

1.1. Fundamental principles of nuclear fusion **1**

1.2. Tungsten as material for ITER divertor **6**

1.3. Plasma – wall interaction **7**

1.4. Objectives of the present thesis **13**

2. Methodology and investigated material **15**

2.1 Investigated materials **15**

2.2 Mechanical deformation **16**

2.3 Specimen preparation **17**

2.4 High flux plasma exposure on PILOT-PSI **18**

2.5 Thermal Desorption Spectroscopy (TDS) **20**

2.6 Nanoindentation (NI) **21**

2.7 Scanning Electron Microscopy (SEM), Electron Backscatter Diffraction (EBSD) and Focused Ion Beam (FIB) **21**

2.8 Transmission Electron Microscopy (TEM) **22**

2.9 Nuclear reaction analysis (NRA) **23**

3. Experimental results and discussion **25**

3.1 Microstructure of reference and deformed tungsten **25**

3.2 Influence of microstructure on gas retention (TDS) **27**

3.2.1. Impact of plastic deformation and exposure fluence on D retention and surface microstructure, studied at baseline exposure temperature (470 K) **27**

3.2.2. Impact of plastic deformation and exposure temperature on D retention, studied at fixed fluence (10^{26} D/m^2) **33**

3.2.3. Impact of plastic deformation and plasma composition, studied at baseline exposure conditions (T=470 K, fluence 5×10^{26}- 1×10^{27} D/m^2) **39**

3.3 Complementary experiments – SEM, NI, NRA, TEM **47**

3.3.1. Modification of surface hardness revealed by nanoindentation **48**

3.3.1.1 Modification of surface hardness induced by D plasma **48**

3.3.1.2 Modification of surface hardness induced by plastic deformation and annealing **53**

3.3.1.3 Modification of surface hardness induced by mixed beam and He plasma **58**

3.3.2. Surface blistering induced by plasma exposure **59**

3.3.3. TEM investigation of the effect of plasma exposure on microstructure **63**

3.3.3.1 Microstructure before exposures **64**

3.3.3.2 Microstructure after exposure to D plasma **66**

3.3.3.3 Microstructure after mixed beam and pure He plasma exposure **68**

4. Conclusions and outlook **73**

4.1. Summary and conclusions **73**

4.2. Outlook **76**

References **77**

Paper 1. Dislocation-mediated trapping of deuterium in tungsten under high-flux high-temperature exposures **85**

Paper 2. Impact of plastic deformation on plasma induced damage and deuterium retention in tungsten **97**

Paper 3. Impact of plastic deformation on retention under pure D or He high flux plasma expose **105**

Acknowledgements

During this PhD I had the opportunity to expand my knowledge and to learn new things in a wide range of areas, to work at different outstanding research institutions and to travel. But most importantly, I met people, without whose support it would not been possible to conduct this research.

First of all, I would like to thank my SCK•CEN mentor dr. Dmitry Terentyev for his guidance over the years and for sharing his knowledge. I am deeply grateful for your time, help, motivation, patience and invaluable support.

I am very grateful to my university promoter prof. dr. ir. Jean-Marie Noterdaeme and the members of the examination board: em. prof. Hendrik Van Landeghem, prof. dr. Roumen Petrov, prof. dr. ir. Dagmar D'hooge, prof. dr. Igor E. Garkusha, prof. dr. Evgeny E. Zhurkin and dr. Yevhen Zayachuk for your valuable comments, questions and suggestions, which helped me to improve the manuscript.

My sincere thanks to my colleagues from SCK•CEN who were closely involved in this research. I am very grateful to Andrii Dubinko for TEM work included in this thesis, and to Wouter Van Renterghem and Konstantza Lambrinou for sharing their knowledge and expertise on microscopy. Many thanks to Boris Minov, Danny Penneman and Milan Konstantinovic for showing me around the lab in the very beginning of my PhD, for all-around conversations, support and a positive environment to work in. I would also like to acknowledge Giovanni Bonny and Andrew Cea for revising the Dutch and English in my manuscript.

This work would not be possible without the collaboration with FOM Institute DIFFER. I would like to say thanks to Thomas Morgan and Kirill Bystrov for plasma exposures and Long Chen and Jordy Vernimmen for their help with TDS measurements and solving technical problems.

Special thanks to Thomas Pardoen, Sophie Ryelandt and Audrey Favache from UCL for the collaboration and help with nanoindentation measurements and always being ready to answer expected and probably unexpected questions.

I am sincerely grateful to my collaborators from UGent for their support with EBSD measurements: Linsey Lapeire and Kim Verbeken for pleasant collaborations, Leandro Tanure for always willing to help, and for interesting discussions.

Thanks to Mikhail Zibrov from IPP Garching for his assistance with NRA.

I would like to thank Lily, Angela, Oksana, Tamara for always being good friends, sharing the struggles of PhD life, being always ready to help during all these four years and just for your smiles. I will never forget all the moments we shared together.

Last but not the least, I am sincerely grateful to my family, for their love, and for encouraging me to go forward. Thank you mom for the moral support during the hardest of times when writing this thesis and your constant faith in me. Thanks to August and Juliana for giving me the warm feeling of being home during the most challenging year of my PhD. Words fail me to express my appreciation to Jo for his love, for sharing pleasant and difficult moments of the last year of my PhD, for strengthening me when I was about to lose hope to finish this work, for his endless support and for always being by my side.

Thank you all!

List of the symbols and abbreviations

CSM	Continuous stiffness mode
D	Deuterium
DEMO	Demonstration Power Station
DF	Double Forged
DFT	Density functional theory
EBSD	Electron Backscatter Diffraction
EDM	Electric Discharge Machine
ELM	Edge Localized Mode
FIB	Focused Ion Beam
GND	Geometrically necessary dislocations
H	Hydrogen
He	Helium
IG	ITER-Grade
ITER	International Thermonuclear Experimental Reactor
MD	Molecular Dynamics
NI	Nanoindentation
NRA	Nuclear reaction analysis
PD	Plastically deformed
PFC	Plasma facing components
QMS	Quadrupole mass spectrometer
QSPA	Quasi steady-state plasma accelerator
REF	Reference recrystallized
SEM	Scanning Electron Microscopy
SSD	Statistically stored dislocations
T	Tritium
TDS	Thermal desorption spectroscopy
TEM	Transmission Electron microscopy
W	Tungsten

List of publications

1. **A. Bakaeva**, D. Terentyev, G. De Temmerman, K. Lambrinou, T.W. Morgan, A. Dubinko, P. Grigorev, K. Verbeken, J.M. Noterdaeme, *Dislocation-mediated trapping of deuterium in tungsten under high-flux high-temperature exposures*, Journal of Nuclear Materials, 479 (2016) 307-315

2. **A. Bakaeva**, D. Terentyev, A. Dubinko, *Impact of plastic deformation on plasma induced damage and deuterium retention in tungsten*, MRS Advances, 2 (55) (2017) 3347-3352

3. **A. Bakaeva**, D. Terentyev, T.W. Morgan, A. Dubinko, W. van Renterghem, L. Tanure, K. Verbeken, *Impact of plastic deformation on retention under pure D or He high flux plasma expose*, Nuclear Materials and Energy, 15 (2018) 48-54

4. D. Terentyev, X. Xiao, A. Dubinko, **A. Bakaeva**, H. Duan, *Dislocation-mediated strain hardening in tungsten: Thermo-mechanical plasticity theory and experimental validation*, Journal of the Mechanics and Physics of Solids, 85 (2015) 1-15

5. P. Grigorev, L. Buzi, **A. Bakaeva**, D. Terentyev, G. De Temmerman, G. Van Oost, J.-M. Noterdaeme, *Numerical analysis of TDS spectra under high and low flux plasma exposure conditions*, Physica Scripta, T167 (2016) 014039

6. A. Dubinko, **A. Bakaeva**, M. Hernández-Mayoral, D. Terentyev, G. De Temmerman, J.-M. Noterdaeme, *Microstructural modifications in tungsten induced by high flux plasma exposure: TEM examination*, Physica Scripta, T167 (2016) 014030

7. P. Grigorev, D. Matveev, **A. Bakaeva**, D. Terentyev, E.E. Zhurkin, G. Van Oost, J.-M. Noterdaeme, *Modelling deuterium release from tungsten after high flux high temperature deuterium plasma exposure*, Journal of Nuclear Materials, 481 (2016) 181-189

8. D. Terentyev, **A. Bakaeva**, T. Pardoen, A. Favache, E.E. Zhurkin, *Surface hardening induced by high flux plasma in tungsten revealed by nano-indentation*, Journal of Nuclear Materials, 476 (2016) 1-4

9. A. Dubinko, D. Terentyev, **A. Bakaeva**, T. Pardoen, M. Zibrov, T.W. Morgan, *Effect of high flux plasma exposure on the micro-structural and -mechanical properties of ITER specification tungsten*, Nuclear Instruments and Methods in Physics Research Section B: Beam Interactions with Materials and Atoms, 393 (2017) 155-159

10. A. Dubinko, D. Terentyev, **A. Bakaeva**, M. Hernández-Mayoral, G. De Temmerman, L. Buzi, J.-M. Noterdaeme, B. Unterberg, *Sub-surface microstructure of single and polycrystalline tungsten after high flux plasma exposure studied by TEM*, Applied Surface Science, 393 (2017) 330-339

11. A. Dubinko, D. Terentyev, **A. Bakaeva**, K. Verbeken, M. Wirtz, M. Hernández-Mayoral, *Evolution of plastic deformation in heavily deformed and recrystallized tungsten of ITER specification studied by TEM*, International Journal of Refractory Metals and Hard Materials, 66 (2017) 105-115

12. D. Terentyev, J. Riesch, S. Lebediev, **A. Bakaeva**, J.W. Coenen, *Mechanical properties of as-fabricated and 2300°C annealed tungsten wire tested up to 600°C*, International Journal of Refractory Metals and Hard Materials, 66 (2017) 127-134

13. A. Bakaev, P. Grigorev, D. Terentyev, **A. Bakaeva**, E.E. Zhurkin, Yu. A. Mastrikov, *Trapping of hydrogen and helium at dislocations in tungsten: an ab initio study*, Nuclear Fusion, 57 (2017) 126040

14. D. Terentyev, A. Dubinko, **A. Bakaeva**, G. De Temmerman, B. Unterberg, *Microstructure and nano-hardness of single crystal tungsten exposed to high flux deuterium plasma*, Physica Scripta, T170 (2017) 014064

15. D. Terentyev, A. Dubinko, **A. Bakaeva**, G. De Temmerman, *Strong sub-surface plastic deformation induced by high flux plasma in tungsten*, Fusion Engineering and Design, 124 (2017) 405-409

16. L. Tanure, **A. Bakaeva**, L. Lapeire, D. Terentyev, M. Vilémová, J. Matějíček, K. Verbeken, *Nano-hardness, EBSD analysis and mechanical behavior of ultra-fine grain tungsten for fusion applications as plasma facing material*, Surface and Coatings Technology, (2018) In press

17. D. Terentyev, J. Riesch, S. Lebediev, T. Khvan, A. Dubinko, **A. Bakaeva**, *Strength and deformation mechanism of tungsten wires exposed to high temperature annealing: Impact of potassium doping*, International Journal of Refractory Metals and Hard Materials, 76 (2018) 226-233

18. W. Van Renterghem, A. Dubinko, **A. Bakaeva**, D. Terentyev, *TEM investigation of the effect of He-seeding on plasma induced defects in tungsten*, Journal of Nuclear Materials, 508 (2018) 74-81

19. C. Yin, D. Terentyev, T. Pardoen, **A. Bakaeva**, R. Petrov, S. Antusch, M. Rieth, M. Vilémová, J. Matějíček, T. Zhang, *Tensile properties of baseline and advanced tungsten grades for fusion applications*, International Journal of Refractory Metals and Hard Materials, 75 (2018) 153-162

English summary

Nuclear fusion, where light elements react to form heavier elements, is an alternative to nuclear fission and fossil fuels. Among its advantages are high fuel power density, no highly active long-lived nuclear waste, no emission of harmful gases like carbon dioxide. It is also important to mention, that nuclear fusion is potentially an inexhaustible source of energy, due to the availability of deuterium in sea water (about 30 mg per liter), while the technology for tritium breeding is under development.

One of the most ambitious fusion projects nowadays is ITER – the International Thermonuclear Experimental Reactor under construction in Cadarache, France. ITER is not designed to convert fusion energy into electricity. Its main goal is to demonstrate the possibility to perform controlled nuclear fusion (with a plasma discharge of a given duration and density) and use it for energy generation. ITER's experience will be very important for the following step in fusion energy generation – the construction of the demonstration fusion power plant DEMO.

The majority of the interaction of plasma with the fusion chamber wall will happen in the divertor – the special component situated at the bottom of the chamber. It serves to extract heat and ash produced by the fusion reaction, and to minimize plasma contamination. Due to a number of advantages (the main of them is the high melting point – 3695 K), tungsten is chosen as a plasma-facing material for the ITER divertor. Among other attractive characteristics of tungsten, the following should be mentioned: high thermal conductivity, low erosion rate and low neutron irradiation swelling. During the operation in fusion environment, the surface of divertor components will be subjected to cyclic heat loads, and as a result a certain plastic deformation will accumulate in the material.

This thesis is focused on the study of the impact of plastic deformation, given variable exposure conditions i.e. fluence and temperature, on deuterium and helium trapping and retention in tungsten.

Polycrystalline tungsten provided by the Austrian company Plansee AG was exposed to plasma in linear plasma generator Pilot-PSI, Nieuwegein, the Netherlands. In particular, the material was studied in two conditions: reference (according to ITER specification) and plastically deformed (mimicking the effect of long term operation under cyclic load). Pilot-PSI allows one to perform exposures to a high-density low-temperature plasma mimicking the 'sub-displacement threshold' plasma-wall interaction conditions expected in the ITER divertor. The following plasma compositions were studied within this project:

pure deuterium, pure helium and mixed beam (helium-deuterium) plasmas. The exposure temperature was varied in the range of 460-1000 K, the particle flux – (1-3) $\times 10^{24}$ ions /m^2/s and the total fluence - 5×10^{25} – 10^{27} ions/m^2. Thermal Desorption Spectroscopy (TDS) was used to measure the retention of plasma particles, the temperature ramp was kept at 0.5 K/s and the maximum (technically achievable) temperature was 1273 K. A few complementary techniques were used to support the results and discussion of the results of TDS, namely scanning electron microscopy (SEM), nanoindentation (NI), nuclear reaction analysis (NRA) and transmission electron microscopy (TEM).

This thesis consists of four chapters. The first one provides a general introduction to the fundamental principles of fusion and plasma-wall interaction. It is also discussed why tungsten was chosen as plasma-facing material.

Chapter 2 describes the materials studied in this project, the procedures of sample preparation and experimental facilities used for plasma exposure and subsequent analysis.

Chapter 3 reports the experimental results and contains their discussion. It is divided into three sections which report (i) the details of the microstructure of the materials before the plasma exposure, (ii) results of TDS measurements, and (iii) complementary experimental analysis performed on the plasma exposed samples.

Pure deuterium plasma exposure revealed that plastic deformation leads to the complex interplay in the intensity of three main deuterium release peaks. The total deuterium retention was progressively increasing with the fluence, and it is about 50% higher in plastically deformed samples compared to the reference material. Comparison of the retention in the samples exposed at similar temperatures revealed, that in the case of low temperature exposure (600 K and below) plastic deformation enhanced the total retention, while at high temperatures (800 K and above) it reduced it.

Addition of helium in the plasma beam increased the integral retention of He significantly as the fraction of He raised from 80% to 100%. He seeding into the plasma also enhanced the integral retention of D in both reference recrystallized and plastically deformed samples. It was concluded that He seeding played a more important role in the D trapping than plastic deformation under mixed beam exposure. Comparison of pure deuterium and pure helium plasma exposures revealed a significant influence of the plastic deformation on the total retention of helium (the pre-straining suppressed He retention by a factor of three). However, a certain amount of helium may still remain in the samples, since TDS measurement was performed up to 1300 K, thus high temperature TDS is needed to confirm the conclusion.

Complementary techniques were used to support the discussion of TDS results. Nanoindentation demonstrated that plasma exposure significantly increased the resistance to plastic penetration of the indenter in the sub-surface region affected by the exposure. Spatially resolved nanoindentation coupled with EBSD analysis was also applied to investigate the sensitivity of grains with different crystallographic orientations. It was demonstrated that <111> oriented grains are more prone to the plasma exposure than others. SEM analysis revealed the presence of raptured blisters only on the surface of plastically deformed samples and not on the reference samples. The latter was attributed to the influence of the dislocation networks which led to a shallower nucleation of bubbles compared to the reference material. TEM was used to investigate the microstructure on the surface and in the sub-surface region after pure and mixed plasma exposures. A strong increase of the dislocation density (at least one order of magnitude higher) was revealed irrespective of the composition of the plasma. He exposure mainly induces sub-surface damage (within 5 μm), while for D exposure the damage extends to 15-20 μm in depth.

The last chapter concludes and summarizes the main experimental observations reported in Chapter 3 and provides the outlook for further study.

Nederlandse samenvatting (Dutch summary)

Kernfusie, de fusie van lichte elementen om zwaardere te vormen, is een alternatief voor kernsplijting en fossiele brandstoffen. Tot de voordelen behoren een hoge brandstofsdichtheid, geen hoogactief langlevend kernafval en geen uitstoot van schadelijke gassen zoals kooldioxide. Het is ook belangrijk om te vermelden dat kernfusie een potentieel onuitputtelijke bron van energie is, vanwege de beschikbaarheid van deuterium in zeewater (ongeveer 30 mg per liter), terwijl de technologie voor de generatie van tritium in ontwikkeling is.

Op heden is een van de meest ambitieuze fusieprojecten ITER - International Thermonuclear Experimental Reactor, die in aanbouw is in Cadarache, Frankrijk. ITER is niet bedoeld om fusie-energie om te zetten in elektriciteit. Het hoofddoel is om de mogelijkheid van gecontroleerde kernfusie te demonstreren (d.w.z. plasma-ontlading van een gegeven duur en dichtheid) en deze te gebruiken voor de opwekking van energie. De opgedane ervaringen van de bouw en uitbating van ITER is zeer belangrijk zijn voor de volgende stap in de ontwikkeling van fusie-energie - de bouw van de demonstratie-kerncentrale DEMO.

Het grootste deel van de interactie tussen plasma en wand van de fusiekamer vindt plaats in de divertor - een specifiek onderdeel dat zich onderaan in de fusiekamer bevindt. Het onderdeel dient voor de extractie van warmte en as die geproduceerd worden door de fusiereactie en om plasmaverontreiniging te minimaliseren. Vanwege een aantal voordelen (het belangrijkste is het hoge smeltpunt - 3695 K), is wolfraam gekozen als materiaal voor de ITER-divertor. Andere aantrekkelijke eigenschappen van wolfraam zijn: hoge thermische geleidbaarheid, lage erosie en weinig zwelling. Tijdens de werking in een fusie-omgeving, zal het oppervlak van de divertor worden onderworpen zijn aan cyclische warmtebelastingen, met als resultaat dat het materiaal plastisch zal vervormen.

Dit proefschrift richt zich op de studie van de impact van plastische vervorming, onder verschillende bestralingscondities, d.w.z. de impact dosis en temperatuur op de deuterium- en heliumretentie in wolfraam.

Polykristallijn wolfraam, geleverd door het Oostenrijks bedrijf Plansee AG, werd blootgesteld aan plasma in de lineaire plasmagenerator Pilot-PSI, Nieuwegein in Nederland. In het bijzonder werd het materiaal onderzocht onder twee omstandigheden: de referentie (volgens ITER-specificatie) en plastisch vervormd (het nagebootste effect van langdurige werking onder cyclische thermische belasting). Pilot-PSI maakt het mogelijk om blootstellingen uit te

voeren aan een plasma met lage dichtheid en lage temperatuur, die de verwachte omstandigheden in de ITER-divertor nabootst. De volgende plasmasamenstelling werden binnen dit project bestudeerd: puur deuterium, puur helium en gemixte helium-deuterium plasma's. De temperatuur werd gevarieerd in het interval 460-1000 K, met deeltjesflux - (1-3) x 10^{24} ionen/m^2/s en totale dosis - 5 x 10^{25} - 10^{27} ionen/m^2. Thermische Desorptie Spectroscopie (TDS) werd gebruikt om de retentie van de plasmadeeltjes te meten, het temperatuurstijgingstempo werd constant gehouden op 0,5 K/s en de maximale (technisch haalbare) temperatuur was 1273 K. Er werden verscheidene complementaire technieken gebruikt om de resultaten en bespreking van de resultaten van TDS, namelijk scanning elektronenmicroscopie (SEM), nanoindentatie (NI), kernreactieanalyse (NRA) en transmissie-elektronenmicroscopie (TEM).

Dit proefschrift bestaat uit vier hoofdstukken. Het eerste biedt een algemene inleiding tot de fundamentele principes van fusie en plasma-wandinteractie. Er wordt ook besproken waarom wolfraam werd gekozen als aan plasma blootgesteld materiaal.

Hoofdstuk 2 beschrijft de materialen die in dit project zijn bestudeerd, procedures voor de monsterbereiding en experimentele faciliteiten die worden gebruikt voor plasmablootstelling en de daaropvolgende analyse.

Hoofdstuk 3 rapporteert de experimentele resultaten en hun bespreking, en is onderverdeeld in drie secties die (i) de details van de microstructuur van de materialen vóór de plasmablootstelling, (ii) de resultaten van de TDS-metingen en (iii) de complementaire experimentele analyse beschrijven die is uitgevoerd op de aan plasma blootgestelde monsters.

Pure deuterium plasma-blootstelling toonde aan dat plastische vervorming leidt tot een complex samenspel in de intensiteit van drie belangrijke deuterium-pieken. De totale deuteriumretentie nam progressief toe met de fluentie en is ongeveer 50% hoger in plastisch vervormde monsters in vergelijking met het referentiemateriaal. De vergelijking van de retentie in de monsters die blootgesteld werden bij vergelijkbare temperaturen onthulde dat in het geval van een lage temperatuurblootstelling (600 K en lager), de plastische vervorming de totale retentie verhoogde, terwijl bij hoge temperaturen (800 K en hoger) het omgekeerde effect werd waargenomen.

De toevoeging van helium aan de plasmabundel toonde aan dat de integrale retentie van He sterk toenam naarmate de fractie van He steeg van 80% tot 100%. Het toegevoegde He verbeterde ook de integrale retentie van D in zowel referentie-gerekristalliseerde als plastisch vervormde monsters. Er werd geconcludeerd dat de toevoeging van He aan de plasmabundel een belangrijkere

rol speelde in de retentie van D dan plastische vervorming. De vergelijking van een blootstelling aan zuiver deuterium en zuiver heliumplasma onthulde dat er een significante invloed is van de plastische vervorming op de totale retentie van helium (de plastische vervorming onderdrukte de retentie van He met een factor drie). Er kan echter nog steeds een bepaalde hoeveelheid helium in de monsters achterblijven, aangezien de TDS-meting slechts tot 1300 K werd uitgevoerd. TDS op hoge temperatuur is dus nog nodig om deze conclusie te bevestigen.

Complementaire technieken werden gebruikt om de bespreking van de TDS-resultaten te ondersteunen. Nanoindentatie toonde aan dat de plasmablootstelling de weerstand tegen plastische penetratie van de indenter in het onderoppervlak dat door de blootstelling werd beïnvloed aanzienlijk verhoogde. Ruimtelijk gescheiden nanoindentatie gekoppeld aan EBSD-analyse werd ook toegepast om de gevoeligheid van de resultaten aan korrels met verschillende kristallografische oriëntaties te onderzoeken. Er werd aangetoond dat <111> georiënteerde korrels vatbaarder zijn voor de plasmablootstelling dan de andere. SEM-analyse onthulde de aanwezigheid van gebroken bellen alleen op het oppervlak van plastisch vervormde monsters en niet op de referentiemonsters. Dit laatste werd toegeschreven aan de invloed van de dislocatienetwerken, die kiemvorming van bellen veroorzaakten dichter onder het oppervlak in vergelijking met het referentiemateriaal. TEM werd gebruikt om de microstructuur in het oppervlak en onderoppervlak te onderzoeken na pure en gemengde plasmablootstellingen. Een sterke toename van de dislocatiedichtheid (minstens één grootteorde) werd vastgesteld, ongeacht de samenstelling van het plasma. De blootstelling veroorzaakt hoofdzakelijk schade aan het oppervlak (< 5 μm), terwijl blootstelling aan D-schade tot op een diepte van 15-20 μm veroorzaakt.

Het laatste hoofdstuk vat de belangrijkste experimentele waarnemingen beschreven in hoofdstuk 3 samen, evenals de vooruitzichten voor verder onderzoek.

1

Introduction

1.1. Fundamental principles of nuclear fusion

The increasing human population and life standards lead to higher energy demands. The majority of electricity is now produced by burning fossil fuels, which are limited and result in environmental deterioration. Nuclear fission energy production is an alternative to fossil fuels, but unfortunately there are a number of fundamental problems. The most undesirable one is nuclear waste which, due to its high half-life time (4.5×10^9 years for U and 8.0×10^7 years for Pu), has to be stored in special mines for hundreds of thousands of years. The possible solution for this problem proposed in the fifties is nuclear fusion – the reaction between light elements form heavier elements.

Nuclear fusion offers some advantages in comparison with other energy sources, among them are:

- higher fuel power density (controlled fusion reaction reactions releases about four times as much energy as nuclear fission and nearly four million times more than a chemical reaction of burning of coal, oil or gas)
- no high activity long-lived nuclear waste (none of the products of a fusion reaction are radioactive, fusion neutrons can induce radioactivity, but a clever choice of structural and other materials can minimize the induced activity, thereby only short lived radioactivity is produced [1])
- no emission of harmful gases like carbon dioxide or other greenhouse gases into the atmosphere

- inexhaustible source of energy (about 30 mg of deuterium can be found in each liter of sea water [2], while the initial amount of tritium to launch the reaction can be produced using currently operating fission powerplants).

The principle behind fusion reaction is the following: two light high energetic nuclei collide, overcome the repulsive Coulomb forces and are attracted by strong interaction forces at short distances of about 10^{-15} m. Accordingly to the laws of conservation of mass and energy, a new nucleus is formed which is accompanied by a large amount of released energy. Figure 1 demonstrates the dependence of charged nuclei interaction energy on the distance between them, with the Coulomb potential barrier which needs to be overcome in order to undergo a nuclear reaction.

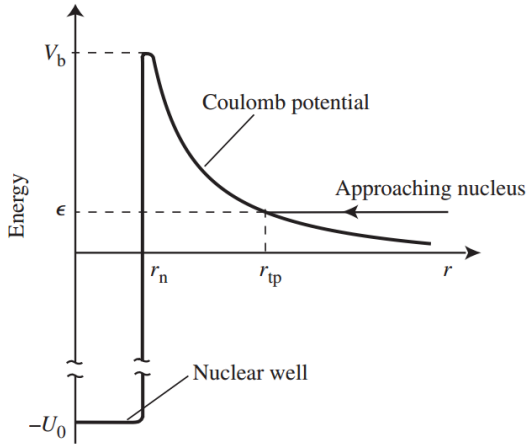

Figure 1 Potential energy as function of distance between two charged nuclei [3]

There are several fusion reactions possible, among them are:

$$ {}_1^2D + {}_1^2D \rightarrow {}_1^3T\ (1.01\ MeV) + {}_1^1H\ (3.02\ MeV) \quad (1) $$

$$ {}_1^2D + {}_1^2D \rightarrow {}_2^3He\ (0.82\ MeV) + n^0\ (2.45\ MeV) \quad (2) $$

$$ {}_1^2D + {}_2^3He \rightarrow {}_2^4He\ (3.6\ MeV) + {}_1^1H\ (14.7\ MeV) \quad (3) $$

But the reaction with the highest cross-section is the fusion of deuterium and tritium producing helium and an energetic neutron [1]:

$$ {}_1^2D + {}_1^3T \rightarrow {}_2^4He\ (3.05\ MeV) + n^0\ (14.1\ MeV) \quad (4) $$

The nuclei of deuterium and tritium have the lowest binding energy per nucleon, so the kinetic energy for the highest fusion probability is the lowest [1]. It can be seen from Figure 2 that D-T reaction has the highest cross-section at

around 100 keV, while the largest probability for the other reactions is still lower than the one of D-T and occurs at much higher temperatures.

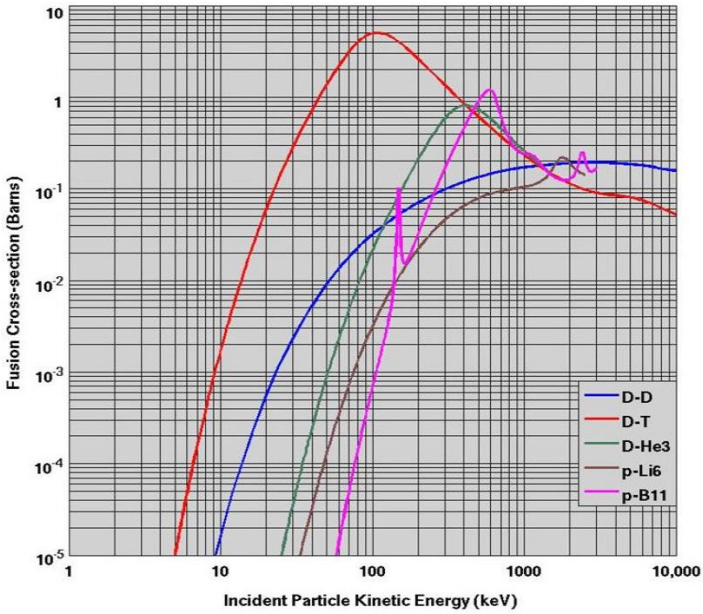

Figure 2 Fusion cross-sections of various fusion reactions as a function of kinetic energy of an incident D or p on a stationary target [1]

Fusion fuels, contrary to fission ones, are widely available in nature and nearly inexhaustible. Deuterium can be easily extracted from all forms of water, while naturally occurring tritium is extremely rare on Earth. It can be produced by neutron activation of lithium-6 or lithium-7. The typical reactions are listed below [2]:

$$^{6}_{3}Li + n \rightarrow {}^{4}_{2}He + {}^{3}_{1}T + 4.8\ MeV \quad (5)$$

$$^{7}_{3}Li + n \rightarrow {}^{4}_{2}He + {}^{3}_{1}T + n - 2.5\ MeV \quad (6)$$

There are a number of technological challenges which have to be fulfilled in order for light atoms to react at a high enough rate: very high temperature (an order of 100 million degrees) to provoke high-energy collisions; sufficient plasma particle density (2-3 × 10^{20} particles/m^3) to ensure sufficient number of fusion events; and sufficient confinement time (1-2 s) to ensure that the energy used to start and maintain the reaction is not wasted too quickly [4]. These conditions led researchers to the principle of magnetic confinement: in order to keep the hot plasma remote from the wall, it is generated inside a toroidal vacuum chamber and confined by a strong magnetic field.

The most promising candidates for the fusion reaction to be realized by magnetically confining thermonuclear plasmas are tokamaks and stellarators [5] (Figure 3). The toroidal and poloidal fields needed for the confinement of plasma in stellarator are produced by the complex configuration of external magnets. Due to the engineering complexity less efforts were made in the stellarator research program and fusion research has been mainly focused on the development of tokamaks.

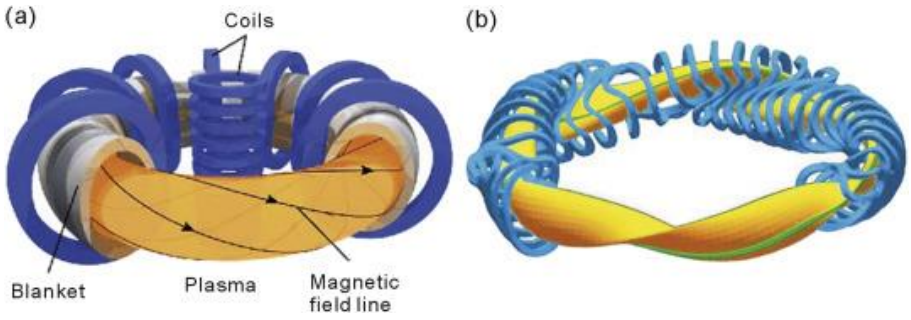

Figure 3 Schematics of magnetically confined plasmas in (a) tokamaks; (b) stellarator configurations [5]

The word "tokamak" comes from Russian acronym that stands for "toroidal chamber with magnetic coils", which has been developed in the 1960's in Russia. Plasma confinement in tokamak is possible due to the combination of a toroidal magnetic field and the magnetic field induced by a plasma current, which in turn is induced by changing current in a central solenoid.

Scientific feasibility of both types of confinements has been demonstrated by a number of existing devices. Major examples of stellarators include Wendelstein 7-X in Germany, the Helically Symmetric Experiment (HSX) in the USA, and the Large Helical Device in Japan. Among the most well-known tokamaks should be mentioned: JET in United Kingdom (1983 [6]), DIII-D (1986 [7]) and Alcator C-Mod (1993 [8]) in USA, TEXTOR (1981 [9]) and ASDEX Upgrade (1991 [10]) in Germany, WEST (1988 [11]) in France, Globus-M (1999 [12]) in Russia and EAST in China (2006 [13]).

The next step towards the commercial fusion power plant is the construction of a fusion power installation ITER – International Thermonuclear Experimental Reactor (Figure 4) currently under construction in Cadarache, France. The construction is scheduled to be completed in the mid-2020s, and the reactor is expected to run for approximately 20 years [14]. It will produce about 500 MW of fusion power in nominal operation, for pulses of 400 seconds and longer, while the typical plasma heating levels during the pulse are expected to

be about 50 MW, so thermal efficiency Q=10 [15], thus during the pulse the ITER plasma will create more fusion energy than the heating energy put into the plasma. Fusion energy will be withdrawn by transfer of kinetic energy of neutron (which takes 75% of total energy release) into heat. But ITER is not designed to convert the fusion energy into electricity. The main goal of ITER is to test the technologies necessary for future commercial power plants and to demonstrate the possibility to perform controlled nuclear fusion and use it for the energy generation. Its experience is very important for the following step in fusion energy generation – construction of the demonstration fusion reactor plant DEMO. DEMO, expected to start the operation in the early 2040s [16], with its main aim to demonstrate the production of net electricity and operation with a closed fuel-cycle, will be the single step between ITER and a commercial fusion reactor.

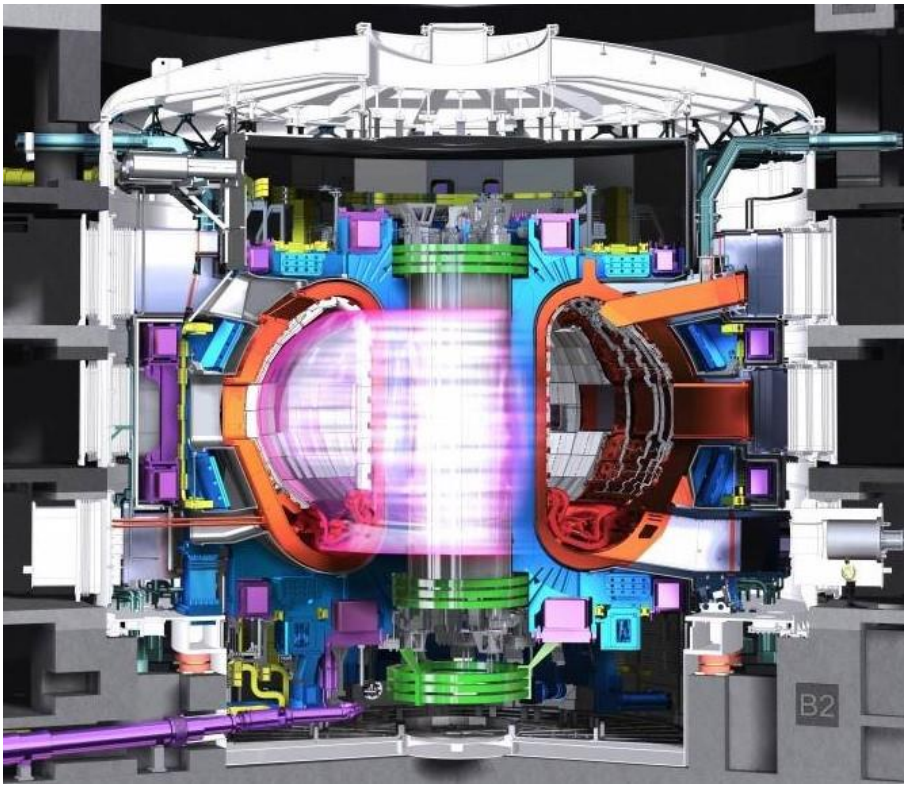

Figure 4 The model of the ITER tokamak with plasma [17]

The production of tritium will occur in ITER's chamber during its operation due to the presence of lithium in the in-vessel component called tritium blanket module. Note that the generation of fusion energy and production of fuel is

related to the operation with fast neutrons, therefore intrinsically, fusion reactors should be classified as a nuclear installation and all necessary measures to protect from nuclear hazards need to be taken.

One of the main challenges of ITER (as well as of DEMO) construction is selection and development of suitable materials for the plasma facing components (PFC) for safe and reliable operation within fusion environment for the planned 30 years of the ITER operation. PFC of the wall and divertor will be subjected to high thermal, mechanical and electromagnetic loads, as well as high fluxes of plasma particles.

1.2. Tungsten as material for ITER divertor

Tungsten, with the highest melting point of all the metals, was chosen as plasma-facing material for the ITER divertor - the special ITER component, where the majority of plasma-wall interaction will happen. It will be situated at the bottom of the fusion chamber, and its aims are: to extract heat via a pressurized water flow and ash produced by the fusion reaction, to minimize plasma contamination, and to protect the surrounding walls from thermal and neutronic loads [18-20]. The plasma ions reaching the divertor target plates will be neutralized into gas which can then be pumped away by the vacuum system [20].

Each of the 54 cassettes of the divertor has stainless steel supporting structure and three plasma-facing components: the dome and the inner and outer vertical targets (Figure 5). The two last ones are positioned where the particle bombardment will be particularly intense in ITER. Current design of the divertor uses a tungsten monoblock geometry for the inner and outer vertical targets and a flat tile geometry for the dome umbrellas and the particle reflector plates [18]. The tungsten monoblocks are required to withstand 5000 stationary load cycles at a power flux density of 10 MW/m^2 as well as 300 transient (less than ten seconds) cycles up to 20 MW/m^2 [21, 22]; peak particle flux is expected to be about 10^{24} $m^{-2}s^{-1}$ and operation temperature window is 200-1000°C.

Since the PFC will be subjected to high neutron and ion fluxes causing erosion, high cyclic heat fluxes causing thermal fatigue, plasma disruptions and vertical displacement events causing thermal shocks, the plasma facing material has to fulfill many various requirements to withstand high energy and particle fluxes and ensure desired lifetime. Among the criteria for PFC material selection were high melting point, high thermal conductivity, high fracture toughness, low erosion rate, low activation, low swelling, etc.

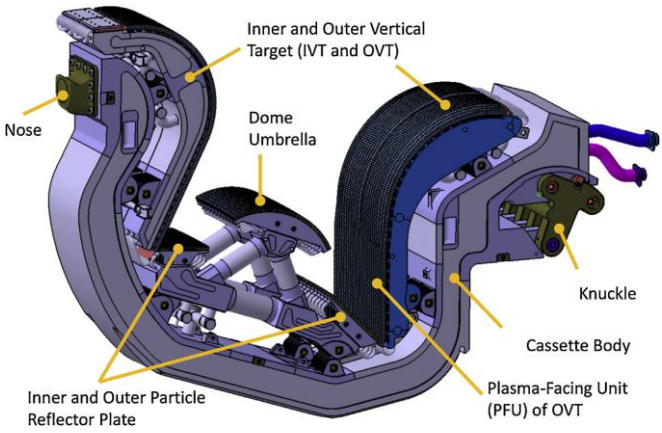

Figure 5 Schematic view of a remotely removable cassette of the ITER divertor [23]

As the ideal material suited for the purpose does not exist in nature, a number of compromises had to be reached in order to select the best candidate. Due to the high melting point (3695 K) [24], high thermal conductivity at room temperature [25], low erosion rate [26] and low neutron irradiation swelling [25] tungsten was selected to be the plasma facing material for ITER divertor [18]. But, along with advantages, tungsten has a number of negative features which can have a strong impact on its structural integrity under plasma operation conditions. Among the negative aspects are: high atomic number Z which does not allow high tungsten concentration in plasma, relatively low temperature of recrystallization, high ductile-to-brittle transition temperature which imposes limitations on coolant temperature, and neutron irradiation embrittlement [25]. All these features give an explanation as to why so many studies are dedicated to tungsten and its performance under fusion operation conditions.

1.3. Plasma – wall interaction

During both normal operation (with Edge Localized Modes (ELMs)) and the off-normal events (such as disruptions and Vertical Displacement Events) PFCs will be subjected to the heat loads. This means that tungsten as PFC material must withstand the superposition of steady state and cyclic heat loads.

Heat loads in ITER and DEMO will result in “thermal shock” which is expressed as surface roughening and cracking. The extend of material degradation depends on the material microstructure (grain size, dislocation density, texture, chemical composition) and exposure conditions (energy, pulse duration, surface temperature).

Compressive stresses, which occur in the sub-surface area due to the temperature gradient during exposure, can be high enough to generate irreversible plastic deformation. During the cooling phase it can lead to the appearance of tensile stresses, which in turn might be sufficient to initiate crack formation. An example of a cracking under the surface is presented in Figure 6 [25].

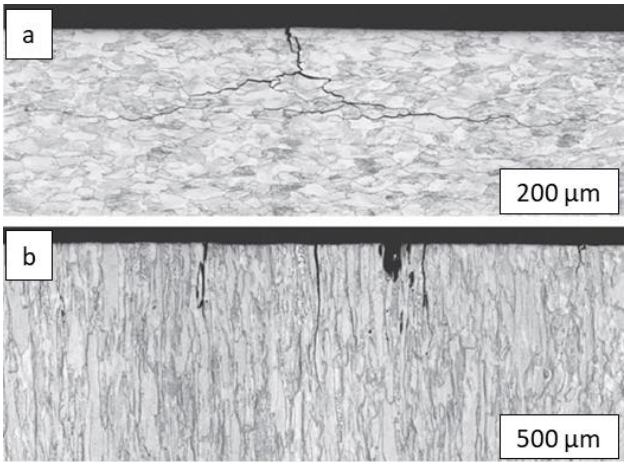

Figure 6 Light microscopy images of the etched cross-sections of thermal shock-loaded specimens with grains oriented (a) parallel and (b) perpendicular to the loaded surface; cracks follow the grain orientation/deformation direction [25]

3D elastic-plastic finite element analysis of a tungsten monoblock geometry (28×28×12 mm) during a cycle of plasma discharge is described in [18]. The result of this work (temperature and stress distribution) is demonstrated on Figure 7: there is a steep temperature gradient at the end of heat pulse (10 s) which in turn generated thermal stresses and plastic strain (Figure 7 (a)); the maximum stress was found to be compressive stress after 10 s (Figure 7 (b)) and tensile stress after 20 s (Figure 7 (c)).

The defects generated in the crystal structure due to neutron irradiation will lead to the swelling and hardening of the material, which depends on the exposure temperature [27, 28]. It has been demonstrated that the effect of swelling can be mitigated by annealing, and complete recovery of microstructure should occur above 1200°C [29]. The irradiation induced hardening might represent a challenge in using the tungsten at operational temperature below 800°C and at irradiation dose exceeding 0.1 dpa [30].

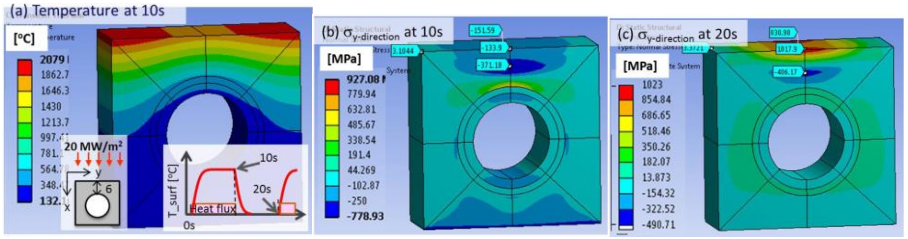

Figure 7 (a) Temperature distribution at 10 s (end of thermal pulse) in the loading case as illustrated in the sketch, (b) distribution of stress in y-direction at 10 s, (c) distribution of stress in y-direction at 20 s (end of cooling phase) [18]

Another important subject to study regarding plasma-wall interaction is gas retention – the process when helium and hydrogen isotopes atoms are lost from the plasma and penetrate into the wall material. Retention affects the fuel usage efficiency and plasma control, which in turn affect particle and energy confinement. Thus, helium and hydrogen isotope retention leads to the degradation of PFC material properties and lowers their performance under exposure to plasma. Another danger is possible permeation of tritium through the PFC into the cooling system, leading to safety issues. Tritium is a toxic and radioactive material, and in order to limit possible undesirable environmental consequences of the unlikely case of tritium release, safety authorities set a limit of 700 g of tritium accumulated in the vacuum chamber of ITER [31] in order to limit possible environmental consequences in case of unlikely even of tritium release.

The retained helium and hydrogen isotopes accumulate on 'natural' (pre-existing) microstructural defects such as dislocations and grain boundaries [32] and therefore suppress the ability of the material to relieve thermal stress by plastic deformation.

While it is known from [33], that at the low temperature (i.e. ~450 K) the bulk permeation of hydrogen isotopes is suppressed and the formation of gas bubbles and cavities occurs mainly in the sub-surface region, at the temperatures of 1000 K and higher, a significant contribution of the bulk retention at a depth up to a millimeter is to be accounted for. Another important point is that the sub-surface trapping is a non-equilibrium process primarily defined by the combination of plasma flux, surface temperature (and its gradient towards the bulk) and material microstructure [34]. Material microstructure plays a crucial role because it defines the density and the strength of the trapping sites inducing the formation of clusters of hydrogen isotopes that cannot nucleate in the perfect bulk due to the absence of hydrogen self-trapping in body-centered cubic tungsten [35, 36]. Plasma-induced defects (such as bubbles [37]), neutron irradiation lattice defects (Frenkel pairs and their clusters [38]) and thermal

fatigue-induced defects (dislocation pile-ups and slip bands [39]) will be formed in the material. Due to this, the initial microstructure of the PFC material will undergo a constant modification.

The following naturally existing and radiation-induced defects are of special relevance with respect to hydrogen isotope retention: vacancies, small vacancy clusters, grain boundaries, dislocations and voids. Trapping at dissolved interstitial impurities (C, O) is also possible, but usually considered to be too weak for the initiation of nucleation of hydrogen isotope bubbles at temperatures above 450 K [34]. Therefore, focus is put on understanding of the role played by each type of the above mentioned defect microstructures.

To extend the understanding of the role played by plastic deformation in the hydrogen isotopes diffusion, trapping and release processes, it is important to screen the effect of temperature and in particular to reveal whether the dislocation-enhanced retention also occurs above 800 K, where the retention in low-dislocation density material (i.e. coarse-grained and recrystallized samples) strongly decreases [40].

Addition of helium in deuterium plasma influences the mechanisms of hydrogen isotope trapping. As it was demonstrated in [41], the depth at which helium and hydrogen bubbles were found after non-damaging ion irradiation (i.e. the kinetic energy of impinging ions was too low to directly displace W atoms from their sites), is very different. The fundamental reason is the different self-trapping mechanism of the gas ions in the target. The density functional theory (DFT) calculations and molecular dynamics (MD) simulations showed that two hydrogen atoms trap each other weakly with the binding energy of < 0.3 eV, whereas helium atoms form strong binding pairs with the binding energy of about 1 eV [41]. Correspondingly, the seeding of He ions into the D plasma at elevated temperatures (440–650 K) significantly reduces the D concentration under the high fluence exposure [42, 43]. He/D ratio in the later works was 10/90, and the effect of a higher content of He still should be investigated.

Thermal desorption analysis (TDS) after high flux pure D and helium-seeded plasma exposures of recrystallized pure tungsten was performed previously and reported in [44]. The energies of D and He ions were fixed at 38 eV and 76 eV respectively. The TDS analysis revealed three major release stages at 550, 650 and 800 K. Seeding of He ions into the plasma at exposure temperatures below 350 K did not have a big influence on D retention, while at temperatures above 400 K D retention decreases significantly in comparison with the pure D plasma exposure. After plasma exposures above 600 K, the D retention was found to be about 10^{19} $D \cdot m^{-2}$ independently of the He ion concentration. Nuclear reaction analysis (NRA) showed a good agreement with the TDS data with respect to the integral retention. This was taken as an

argument indicating that He seeding stipulates the formation of bubbles in the subsurface region and therefore results in the confinement of D retention in the sub-surface region preventing long range diffusion of D in bulk (hence reducing the retention). It was also found that He retention does not depend on the He ion concentration in plasma. He retention was increased from about 2×10^{19} He·m^{-2} to 3×10^{20} He·m^{-2} with raising the exposure temperature from 340 K up to 810 K. This was interpreted as thermally activated diffusion, which apparently is enhanced above 550-650 K, being the temperature of the release stage of He as measured by TDS [44].

Helium and deuterium retention in pure tungsten under low and high fluence exposure conditions was studied in [43]. He seeding into D plasma was found to increase the D retention in the low fluence range (below 10^{23} D/m^2), presumably due to the trapping of D at He clusters which form near the surface [43]. The opposite effect was observed in the high fluence range – He seeding reduced D retention. This feature was attributed to the reduction of the D diffusion deeper into the bulk. TDS results show that the positions of the major D release peaks are similar with and without He seeding in all investigated tungsten grades. It was therefore concluded that the principal structure of the defects where D is trapped is not modified by the presence of He in the plasma [43].

It was demonstrated in [45], that the addition of He in D plasma results in the reduction of D retention at 300 and 500 K for all probed He/D ion range ratios. He retention is affected by ion energy and temperature, but not by He-to-D ratio. The release peak of D, located around 500 K, slightly shifts towards lower temperature due to the addition of He in the plasma, which can be attributed to the modification of the binding energy profile in the mixed He-D-vacancy clusters. It was also shown, in line with earlier experiments, that the addition of He greatly decreases D diffusion and increases D trapping up to 1 μm depth, similar to the results reported in [43, 44].

In-situ transmission electron microscopy and TDS measurements were performed in [46], where pure tungsten was exposed to the high flux He plasma to simulate ITER divertor conditions. Three major peaks around 550, 800 and 1400 K were identified by TDS. The TEM measurements reported that the major part of He bubbles was observed directly after exposure, while during TDS almost all bubbles disappeared before reaching 1200 K. Hence, the release peak around 1400 K could be attributed to the deep diffusion of He and diffusion controlled (accounting for the re-trapping at the sub-surface) release at high temperature [46].

Besides the low energy ion and plasma exposure of single and poly-crystalline tungsten grades, high energy ion accelerators were also used to

expose pre-irradiated samples. Pure polycrystalline tungsten, pre-damaged by 20 MeV ions, was exposed to plasma with a flux up to 10^{22} ion/m^2/s at 440-720 K and the ion energy of 76 eV (i.e. for D_2^+)[42]. He/D ratio was 10/90. NRA measurements allowed to conclude that He seeding significantly reduces D retention within the sub-surface region (up to 6 μm). This conclusions in general is line with other studies of non-damaged tungsten [43, 44], where low flux plasmas were used. Based on the existing data, it is believed that He co-implantation enhances nucleation of sub-surface bubbles which then act as barriers for D permeation and deep diffusion.

Besides He, the impact of natural defects present in the commercial tungsten grades on the retention of hydrogen isotopes should also be highlighted.

From the experience learned on other metals exposed to hydrogen environment, the role of dislocations in hydrogen embrittlement phenomenon is generally acknowledged as crucial (see e.g. [47]). *Ab initio* calculations [48] were applied to characterize the interaction of hydrogen with a ½<111> screw dislocation in tungsten, which is considered as the dominating and key microstructural feature of polycrystalline tungsten. This study revealed strong affinity of hydrogen atoms to the core of screw dislocation. Moreover, ability to form compact multiple clusters by means of 1D glide along dislocation core and eventual trapping on dislocation imperfections (e.g. dislocation intersections or jogs) was observed. Once a cluster accumulates its eighth hydrogen atom, the reconstruction of the dislocation segment occurs resulting in the displacement of tungsten atoms, creating an open volume for the H8 cluster. The currently available information obtained by *ab initio* calculations point to the fact that dislocation networks may serve as efficient agents to provoke nucleation of stable hydrogen nanoclusters. In that perspective, the progressive accumulation of the sub-surface plastic deformation, induced by heat cycle fatigue, should promote the uptake of hydrogen isotopes – to be seen as negative effect.

The importance of the mechanisms responsible for subsequent sub-surface embrittlement of tungsten under ITER-relevant exposure conditions remain uncertain and the synergy of the hydrogen isotopes uptake/diffusion and progressive accumulation of the plastic deformation may affect the properties of material, otherwise studied in the reference conditions. The current thesis, motivated by this study, is to reveal the impact of tungsten microstructure, and in particular microstructure induced by the plastic deformation, on hydrogen isotopes retention.

1.4. Objectives of the present thesis

As it was shown above, plasma-wall interaction is a complicated process. During the operation in a fusion environment, the plasma facing material is expected to undergo cyclic thermal loads, which will cause stress and temperature gradients, finally leading to cyclic deformation. Such process will lead to the accumulation of deformation inside the plasma facing material. Importantly, heavy plastic deformation has an impact on both mechanical properties and gas trapping due to the increase of dislocation density and possible grain refinement [49]. Hence, the investigation of the impact of the heavy plastic deformation on the interaction of the high flux plasma with the material is an important subject, because it addresses the question how the "aged" material will perform as compared to the "fresh" one. In addition, such study is important to provide experimental information on such fundamental problems as the interaction of dislocations with hydrogen isotopes, their diffusion in the field of dislocation networks and finally nucleation and growths of blisters.

To achieve that, the technical objectives of this thesis were formulated as follows:

- to perform dedicated high flux deuterium plasma exposures of tungsten in the conditions relevant for ITER divertor using reference tungsten of ITER specification, recrystallized tungsten of ITER specification and plastically deformed tungsten of ITER specification. The chemical composition of the material should be fixed, while the microstructure can be varied by applying dedicated heat treatment and/or plastic deformation
- to study the effect of plastic deformation on deuterium trapping and mechanical properties of tungsten surface exposed to plasma
- to reveal the influence of exposure temperature on deuterium trapping in reference and plastically-deformed samples
- to investigate the difference in helium and deuterium trapping under pure helium and deuterium exposure respectively in reference and plastically-deformed material
- to study the influence of plasma composition in case of mixed D-He exposures on the trapping of its components in reference and plastically-deformed samples.

2

Methodology and investigated materials

2.1 Investigated materials

Two commercially produced tungsten grades provided by the Austrian company Plansee AG were investigated in this work. Both grades are polycrystalline tungsten of at least 99.97% purity with the same specification on residual impurities which are listed in Table 1.

Table 1 Impurity content of tungsten used in this study, as specified by the material supplier [50]

Impurity	**Ag**	**Ba**	**Co**	**Fe**	**Mn**	**Ni**	**Ti**	**Mo**	**C**	**O**
(µg/g)	10	5	10	30	5	5	5	100	30	20
Impurity	**Si**	**Al**	**Ca**	**Cr**	**Na**	**Pb**	**Zn**	**H**	**K**	**As**
(µg/g)	20	15	5	20	10	5	5	5	10	5
Impurity	**Cd**	**Cu**	**Mg**	**Nb**	**Ta**	**Zr**	**N**	**S**		
(µg/g)	5	10	5	10	20	5	5	5		

The first grade was produced by hot double forging (the last production step), and was followed by a thermal stress relief treatment at 1270 K and annealing at 1870 K for one hour. Annealing resulted in a more uniform grain size distribution and a lower dislocation density. Hereafter, this material, which was used in a few earlier works, e.g. [51, 52], will be referred as Double Forged (DF) tungsten.

The second grade was fabricated by double hammering. This treatment resulted in the appearance of elongated "carrot-like" grains. After the production, material was annealed at 1273 K for one hour in inert environment. This material was only used, when DF tungsten was not anymore available and will be referred as ITER-Grade (IG) tungsten.

Different fabrication methods and post-heat treatment to reduce the stress and release remaining gaseous impurities (i.e. O, H, N) result in different microstructure and presence/lack of texture in the material, which is shown on Figure 8 to demonstrate the difference in the appearance of grains between 1600C-annealed and as received material.

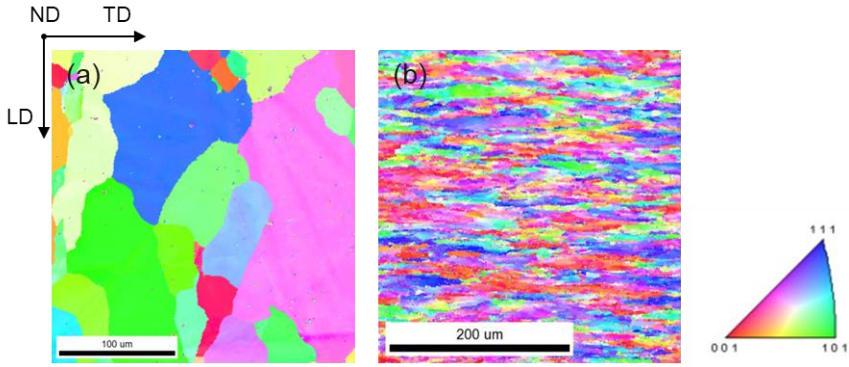

Figure 8 Inverse pole figure maps of the EBSD scan of the initial microstructure of investigated materials: (a) DF tungsten and (b) IG tungsten

In accordance with ITER specification, DF and IG grades adhere to the regulation for chemical composition, microstructure, hardness, density and grain size. Their microstructure will be discussed in section 3.1.

2.2 Mechanical deformation

Mechanical deformation was used to obtain different microstructure, expressed in different dislocation density and grain shape. The tensile samples (shown on Figure 9) were cut and re-annealed at 1273 K for 1 hour in an argon (Ar) atmosphere to release stress possibly introduced by electric discharge machining (EDM). Plastic deformation was applied by performing tensile loading on a mechanical test bench [53] at 873 K in air with a deformation rate of 0.2 mm/min to reach up to 28% deformation, which approximately corresponds to the ultimate tensile strength of the studied tungsten grade at 873 K (after recrystallization).

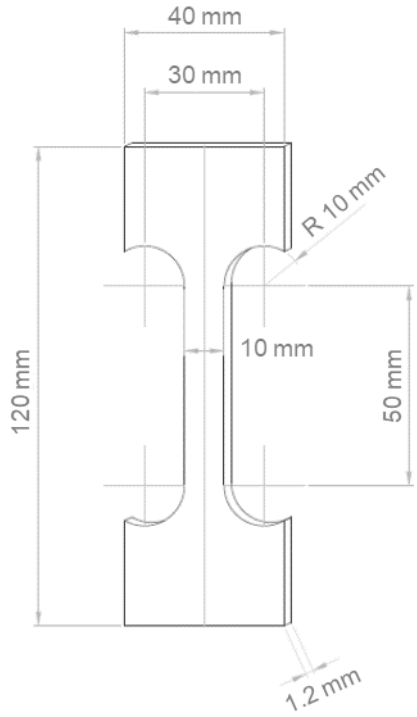

Figure 9 Flat sample geometry for mechanical deformation

2.3 Specimen preparation

After the application of the tensile load, the samples of 10x10x1 mm and 10x3x1 mm (for Transmission Electron Microscopy (TEM)) were cut with EDM (The scheme is shown on Figure 10) and polished prior to any experimental technique was applied.

The polishing procedure includes grinding with *Struers* silicon carbide (SiC) polishing papers (grits of 220, 500, 1200, 2000, 4000 consecutively), polishing with a *Struers TegraPol-11* machine, and subsequent polishing with a diamond polishing suspension (diamond grain size of 3 μm and 1 μm consecutively). Samples for Electron Backscatter Diffraction (EBSD) were additionally electrochemically polished with a NaOH solution at 7 V for 12 seconds using *Struers Tenupol-3*.

The first step of TEM samples preparation is manual mechanical grinding as described in the previous paragraph. As soon as the desirable thickness of 100-130 μm is achieved, the *Well Diamond Wire Saws model 3242* was used to

cut the samples into 1.8×2.4 mm pieces. The last step was to perform electro-chemical polishing using a *Struers Tenupol-3* automatic electrolytic thinning machine and using the solution of 0.15 wt. % NaOH in water with the voltage set at 30V. Since we expect that plasma induced damage in the specimen structure can be located in a layer much thinner than 50-100 μm, so called "back-side" electro-chemical polishing technique was used to study sub-surface layer. Applying the procedure only from the back side of the specimen we do not destroy the surface layer and investigate the very thin sub-surface layer of about 100 μm.

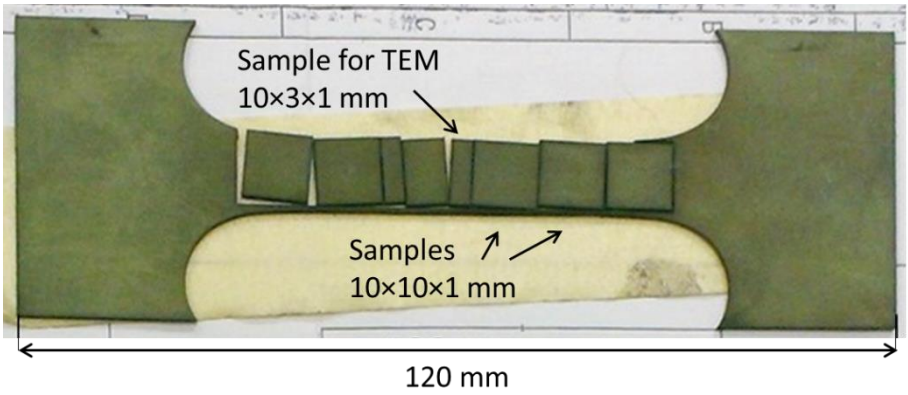

Figure 10 Flat tensile sample after EDM cutting

2.4 High flux plasma exposure on PILOT-PSI

High flux plasma exposures were performed in linear plasma generator Pilot-PSI, which delivers a high-density (~10^{21} m^{-3} [54]) low-temperature (~1 eV [54]) plasma mimicking the 'sub-displacement threshold' plasma-wall interaction conditions expected in the ITER divertor. The schematic overview of the setup is demonstrated on Figure 11.

The plasma beam is generated by a cascaded arc source which can be operated under either steady-state or pulsed mode. Constant gas flow rate is in the range 1.5-3.0 slm (standard liters per minute, which corresponds to 4.5×10^{20} particles per second), which ensures a discharge channel pressure in a range of 10^{3}-10^{4} Pa. Plasma is formed in the discharge channel by an ionizing current of 100 – 220 A and then enters the cylindrical vacuum vessel (Ø 0.4 m and 1 m long). Plasma is confined by an axial magnetic field which can be varied between 0.2 T and 1.6 T. The pressure in the vessel during plasma operation is determined by the inflow of the residual neutrals from the source and the pumping and is

typically of the order of several Pa. The plasma beam, aimed at a solid, actively cooled target, is 56 cm away from the exit of the source discharge channel.

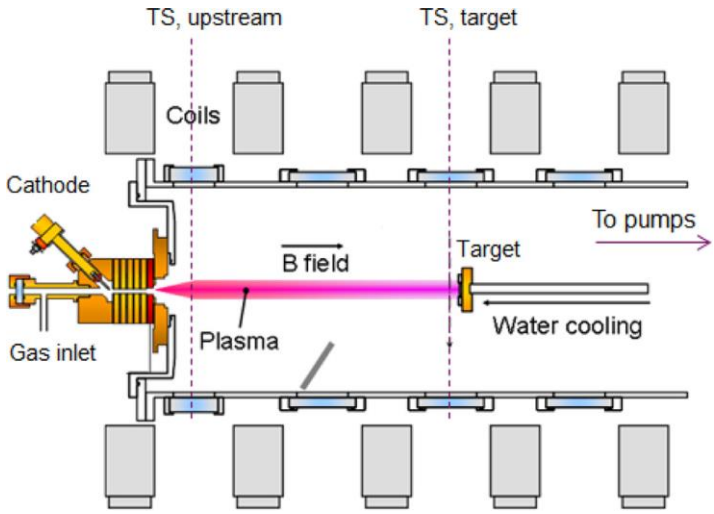

Figure 11 Schematic layout of the Pilot-PSI device [54]

The target (sample) is installed perpendicularly to the plasma beam and is clamped onto a water-cooled (295 K)) copper holder. The cooling water flow is usually in the range of 1-6 l/min. To improve the thermal contact, a layer of GRAFOIL flexible graphite is added between the sample and the holder. The sample surface temperature is defined by the variation of the strength of magnetic field and heat removal and it is measured with a fast infrared camera (FLIR A645 sc) and a spectral pyrometer. Since the surface temperature is not actively controlled, it is impossible to perform absolutely equivalent exposures, but good thermal contact, stable water flow and similar specimen preparation allow to minimize the temperature deviation (±25°C).

Due to the very fast cooling process (2-3 s up to room temperature after the end of plasma exposure), all implanted atoms trapped at weak traps cannot reach the surface and escape from the material. This can result in detrapping (measured by Thermal desorption spectroscopy (TDS)) at the temperatures lower than the temperature of exposure and will be discussed in section 0.

Pure deuterium, pure helium and mixed He-D plasmas were used in this study, the exposure parameters were:

- temperature: 460-1000 K

- flux: (1-3) $\times 10^{24}$ ions /m^2/s
- fluence: 5×10^{25} - 10^{27} ions/m^2.

2.5 Thermal Desorption Spectroscopy (TDS)

TDS is used to estimate the amount of He and D retained in the material after plasma exposures. It is also known as temperature programmed desorption, and it measures the desorption of molecules from a material during a heating cycle. The basics of this method can be found in [55].

Deuterium atoms while heating with a linear temperature ramp gain enough energy to detrap and diffuse in the lattice until they reach the surface and are released.

The TDS setup used here is located in Differ-FOM, the Netherlands. The sample was clamped to a ceramic heater, placed inside the vacuum vessel maintained at a high vacuum of < 5×10^{-7} mbar. The Balzers QMA125 quadrupole mass spectrometer (QMS) monitors the mass 4 (D_2) and mass 3 (HD) partial pressure in the vacuum chamber. Calibration is performed using a deuterium (calibration of mass 4 signal) calibrated leak. The temperature ramp was 0.5 K/s for all the measurements performed, and the maximum temperature was 1273 K. All samples were measured 7-9 days after the exposure to plasma.

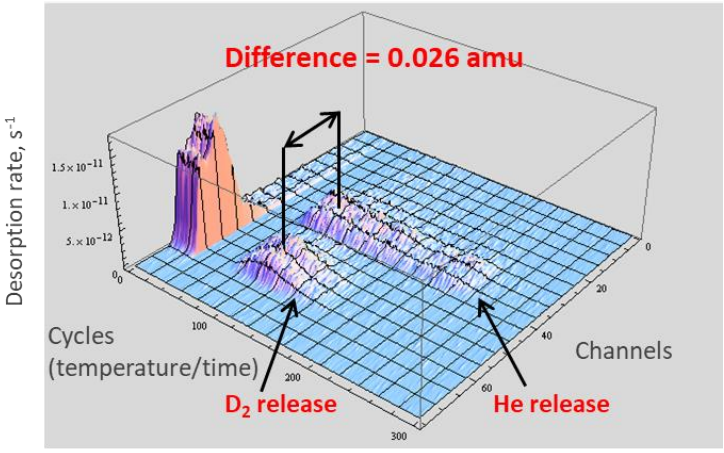

Figure 12 Trial TDS using high resolution QMS

Part of the measurements were performed using high resolution QMS which is sensitive enough to distinguish between He and D_2 masses, although

they are distant by 0.026 amu only (which is about 20 channels in the applied QMS). The calibration using He and D_2 leak allowed one to clearly resolve the Gaussian spectra due to D_2 and He release, such as shown on Figure 12. The 3D plot shows signal counts versus a number of time cycles measured during the TDS. The measurement was made using the reference sample exposed to the trial mixed He/D beam (60%/40%) at 500 K. Due to the limited availability of the high resolution TDS and busy schedule, the interval of 7-9 day after exposures was not possible to maintain, thus the measurements were performed after 0-11 days.

2.6 Nanoindentation (NI)

The purpose of nanoindentation (NI) is to measure the hardness of materials within a very shallow depth when the spatial resolution of conventional mechanical tests are not applicable. Nanoindentation gives the possibility to perform measurements in a very small volumes of material and with a very high precision. This feature is very important for current project, since plasma induced damage affects the material within few μm from the surface.

The samples were tested using an Agilent G200 nanoindenter in order to obtain the Young's modulus and hardness. The indentation measurements were performed in the continuous stiffness mode (CSM) [56] with the standard XP head equipped with a Berkovich diamond tip. The oscillation amplitude and frequency were respectively 2 nm and 45 Hz. The indentation strain rate was set to 0.05 s^{-1} and the specimens were indented down to a penetration depth h=1.5 μm. At least 25 indents spaced by 40 μm have been performed on each specimen, and the hardness estimated using the classical Oliver & Pharr method [56]. The tip area function was calibrated by performing a series of indents in a reference fused silica sample.

2.7 Scanning Electron Microscopy (SEM), Electron Backscatter Diffraction (EBSD) and Focused Ion Beam (FIB)

Scanning electron microscopy (SEM) was applied in order to investigate surface modification induced by plasma exposure, such as possible roughening and blistering. Surface imaging was performed at SCK•CEN using SEM JEOL 6610 with secondary electron detector (accelerating voltage 15 kV and working

distance of 10-11 mm), which is based on the interaction of a focused monochromatic electron beam with material. The details about this technique can be found in [57].

EBSD allows one to study grain size and crystallographic orientation. It is based on recording and indexing of so-called Kikuchi lines that are produced by the backscattered electrons that are subsequently diffracted by the crystal planes. The detailed description of EBSD technique can be found in [58]. A Field Emission Gun Quanta-450 FEI SEM with 20 kV acceleration voltage located in the Department of Materials, Textiles and Chemical Engineering of Ghent University was used to scan the samples. The step size was 1.2-2.0 μm. The specimen was mounted with 70° tilt in order to reduce the path length of the backscattered electrons and to increase the intensity of electron backscatter patterns. During the image post-processing using OIM Analysis software, points with Confidence Index lower than 0.1 were removed.

Focused ion beam (FIB) allows one to prepare micro cross-section cuts in situ in the electron microscope, which can then be imaged with the electron beam without moving the specimen. *FEI Helios Nanolab 650* was used to study microstructure of material, when the preparation of TEM sample was not efficient due to the high surface roughness.

2.8 Transmission Electron Microscopy (TEM)

Light optical microscopes are not suitable to perform investigations at a nanoscale level due to its resolution being limited by a range of visible light wave lengths. Transmission electron microscopes use high energy electrons with wavelength several orders of magnitude shorter, and therefore are capable of imaging at a significantly higher resolution, than light microscopes.

A high energy beam of electrons in transmission electron microscope interacts with a thin sample usually less than 100 nm thick. Signals generated by elastic scattering are used for diffraction patterns and contrast on TEM images. A signal generated by inelastic scattering is needed for Electron Energy Loss Spectroscopy and Energy-dispersive X-ray Spectroscopy. In this work, we have integrated several TEM images which were done for the investigated samples to characterize the microstructure before and after plasma exposure. The samples were studied on a JEOL 3010 TEM working at a voltage of 300 kV. The TEM images were done in a frame of another PhD project which ran in parallel in the same laboratory. All details regarding the technique can be found in that work [59].

The method, described in [60], was used to calculate the dislocation density. A circle was drawn randomly on a TEM image and the number of intersections of it with dislocation lines was counted (an example is shown on Figure 13). Dislocation density was then calculated using the following equation:

$$\rho = \frac{2 \cdot N}{L \cdot t} \quad (7)$$

where N is the number of intersections of the circle with dislocation lines, L – length of the circle, t – local thickness of the specimen at the area of the image. A correction factor was applied for the extinction conditions assuming that all dislocations were a/2<111> type.

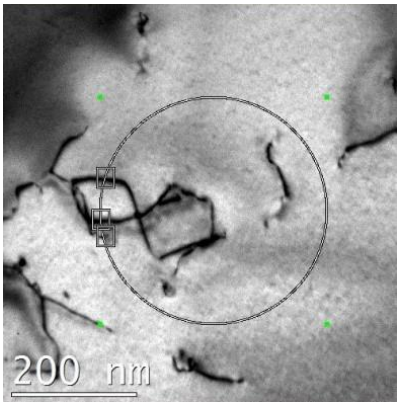

Figure 13 TEM image with a randomly drawn circle showing the process of calculation the dislocation density

2.9 Nuclear reaction analysis (NRA)

Nuclear reaction analysis (NRA) is a non-destructive method which allows one to obtain quantitative deuterium depth profiles in tungsten (or light elements in a heavy material in general). A 3MV tandem accelerator located in IPP-Garching, Germany was used in this study. The nuclear reaction $D(^3He,p)\alpha$ is initiated by bombarding the tungsten samples with ^3He ion beam. The energy distribution and scatter cross-sections of the products of the reaction (p,α) give information about the D depth profile in the material.

The proton detector, with energy resolution around 100 keV, is installed at the scattering angle of 165°C. It is equipped with a parabolic slit which limits the detection solid angle to ~30 msr and with a stopping foil which lets through the high-energy protons but blocks the backscattered He^3 particles.

The detector for alpha particles, only used for the primary beam energy below about 1 MeV, is located at the scattering angle of 102°C. It is equipped with a rectangular slit limiting the detection solid angle to ~9 msr and has no stopping foil.

The depth profiles of retained deuterium were obtained from the measured proton energy distributions using the NRA-DC program [61]. The ^{3}He beam spot limits the analyzed area to about 1×1 mm.

3

Experimental results and discussion

This chapter presents experimental results and their discussion. The chapter is subdivided into three sub-sections. Firstly, the microstructure of the material prior to the plasma exposure is presented. Then the results of TDS measurements done after exposures to plasma with different characteristics are discussed. Afterwards, the supporting modelling and experimental data of SEM, NI, NRA and TEM obtained within this PhD project and other projects is presented to substantiate the discussion and conclusions given in this and the following chapters.

3.1 Microstructure of reference and deformed tungsten

Prior to plasma exposure, the microstructure of the material used in this study was characterized using EBSD and TEM. EBSD analysis of the reference recrystallized sample revealed the presence of randomly oriented grains with a grain size (average grain diameter) in the range of 50-150 μm (Figure 14 (a)), separated mainly by high-angle grain boundaries (with misorientation angle larger than 15 °). The dislocation density measured by TEM was found to be (2-4)×10^{12} m^{-2}, the typical images of dislocation lines and sub-grains are shown on Figure 15 (a, b).

Plastic deformation was applied by performing tensile loading at 873 K in air with a deformation rate of 0.2 mm/min to reach about 25-30% deformation. This approximately corresponds to the ultimate tensile strength of the studied tungsten grade at 873 K (after recrystallization). An example of EBSD inverse

pole map of plastically deformed sample is given on Figure 14 (b). Grains become elongated in the direction of applied load. The average calculated grain diameter decreased to 25-80 μm. The TEM microstructure is demonstrated on Figure 15 (c, d).

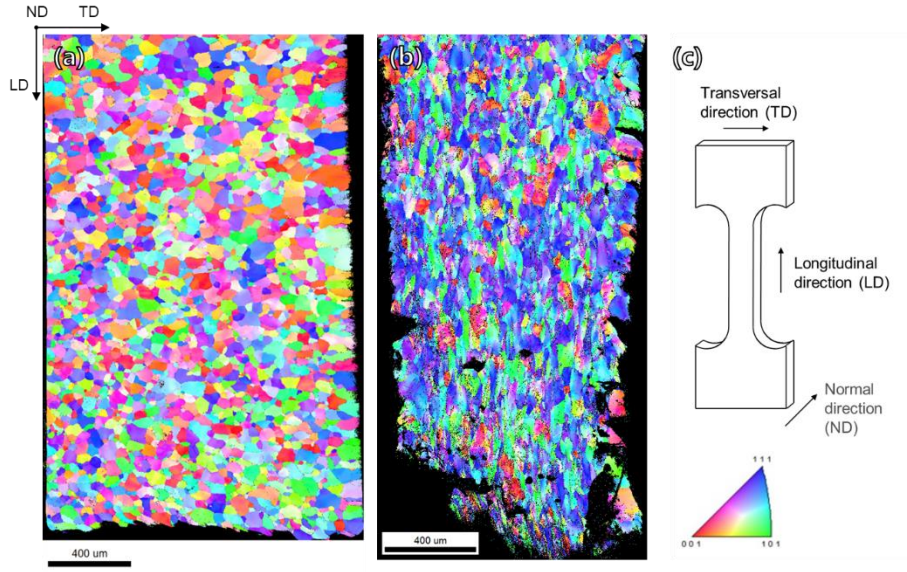

Figure 14 Inverse pole figure map of the EBSD scan of the (a) reference and (b) plastically deformed samples. A sketch in (c) shows the tensile sample and the direction of the applied load

After plastic deformation, TEM samples were extracted from the central part of the deformed sample and prepared accordingly to the procedure described in section 2.3. It was found that plastic deformation resulted in grain refinement and the increase of dislocation density up to 2×10^{14} m^{-2}, i.e. yielding to nearly two orders of magnitude higher compared to the reference recrystallized microstructure. The detailed TEM analysis is reported in [62].

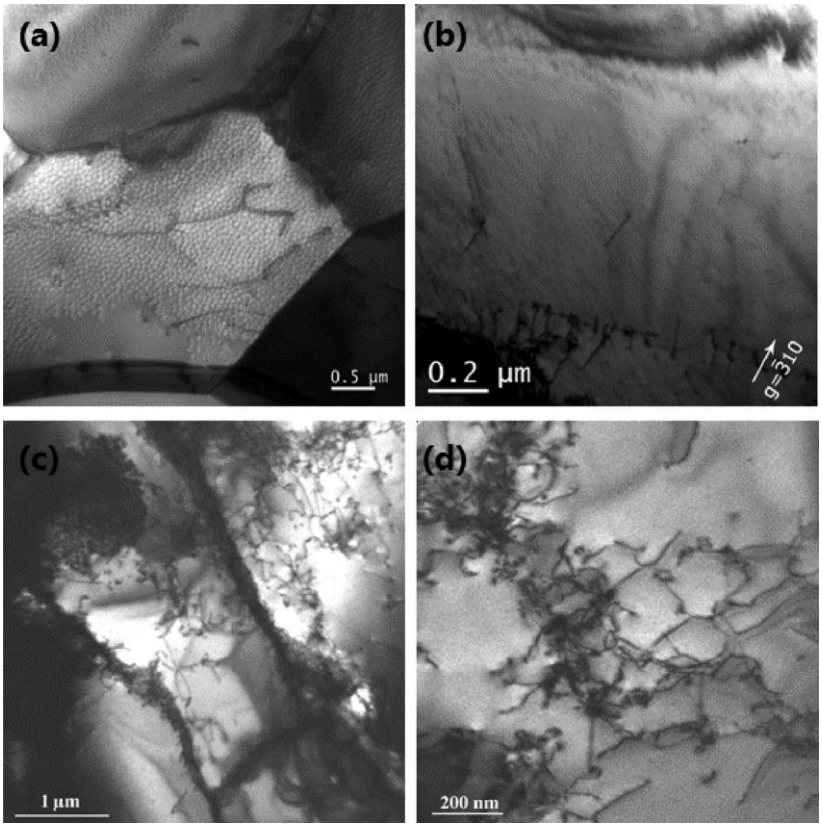

Figure 15 TEM images of (a,b) REF and (c,d) PD samples in the non-exposed condition. The images are taken to demonstrate the sub-grain structure (a,c) and appearance of dislocation lines inside the grains (b,d)

3.2 Influence of microstructure on gas retention (TDS)

3.2.1 Impact of plastic deformation and exposure fluence on D retention and surface microstructure, studied at baseline exposure temperature (470 K)

Three pairs of reference recrystallized and plastically deformed DF tungsten samples were exposed to the fluences of F=8×10^{24}, 5×10^{25} and 3.5×10^{26} D/m^2 to reveal the effect of microstructure and exposure fluence on the hydrogen isotope retention at the fixed exposure temperature. The fluences mentioned correspond to the exposure time of 10, 70 and 490 s. The other

exposure conditions are: temperature 473±10 K, ion energy 50 eV, and the maximum particle flux in the center of the samples (0.8-1.0)×10^{24} D/m^2/s.

A linear superposition of several Gaussian functions was used to fit each of the raw TDS curves. As an example, Figure 16 shows the TDS spectra of the reference sample exposed to fluence of 5×10^{25} D/m^2 and its decomposition to three peaks (henceforth referred to as P_1, P_2 and P_3). According to the previous studies [48, 63], peak P_1 can be attributed to the detrapping of deuterium from dislocations. P_2 is linked to the detrapping of vacancies and small vacancy clusters. Peak P_3 is attributed to D release from large pores. As will be shown later, the appearance of this peak is correlated with the emerging of the surface blisters (will be discussed in a section 0). These pores grow by loop punching or displacement of the whole sub-grain (which creates a sort of flake-like defect) as a result of the coalescence of several bubbles underneath a sub-grain surface [64].

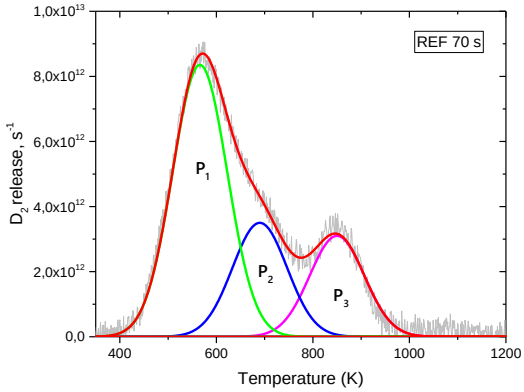

Figure 16 Experimental TDS spectra of deuterium release from reference recrystallized (REF) W sample exposed to fluence of F=5×10^{25} D/m^2 (corresponding to 70 s of exposure time)

The assignment of three peaks proposed above is in good agreements with the data for low energy D ion plasma exposure described in [63]. It was also concluded in [63], on the basis of TDS measurements and computational modelling, that the three major deuterium release stages are attributed to the detrapping from dislocations, vacancies and chemisorption on internal surface of pores. In addition, the second peak P_2 can be assigned to the detrapping from vacancies or to the detrapping of deuterium in a molecular form.

Figure 17 shows the simplified schematic representation of the energy landscape of an interstitial hydrogen atom migrating through the solid lattice of

tungsten. Here ΔE_D is the energy barrier which needs to be surpassed by H atom in order to migrate from one equilibrium site (i.e. interstitial position) to another. In the presence of a trap (a vacancy or dislocation line, etc.), H atom would be bound to the trap and will reduce its potential energy by the value ΔE_{Trap}. Hence, ΔE_{Trap}, is the energy barrier which H needs to surpass to escape from the trap and continue its migration in the lattice.

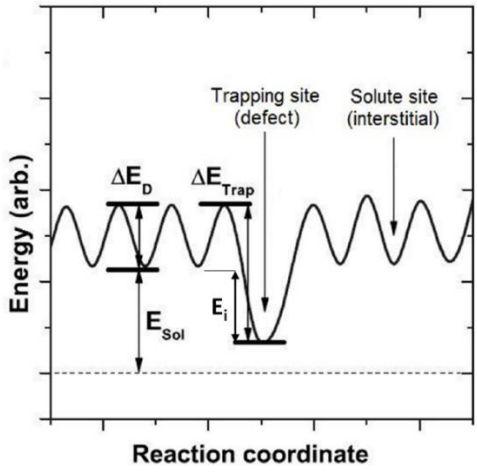

Figure 17 Schematic sketch of the hydrogen energy landscape within the solid [65]

Given the schematics shown in Figure 17, it is evident that E_{Trap} can be decomposed into two parts: E_m - bulk migration energy (equal to 0.39 eV as reported in the *ab initio* study [66] for H) and E_i - the interaction energy between H atom and the defect considered. A simple way to correlate the position of the desorption peak with the activation energy has been proposed in [67] following the analysis based on *Ab initio* calculation. The activation energy was calculated integrating the following equation [67]:

$$\frac{dC(t)}{dt} = -C(t) \cdot \upsilon \cdot exp\left(-\frac{-E_{Trap}}{k_B \cdot T}\right) \quad (8)$$

where $C(t)$ – H concentration stored at traps, k_B – Boltzmann constant, υ – Debye frequency (typical lattice vibration frequency equal to 10^{13} s^{-1} was used), T – temperature over which equation (8) should be integrated. The data obtained is presented on Figure 18. Note that the integration over time and temperature is equivalent, because temperature raises linearly in time. Integration of the temperature is therefore more useful to obtain directly relationship between the specific activation energy and temperature corresponding to the peak release.

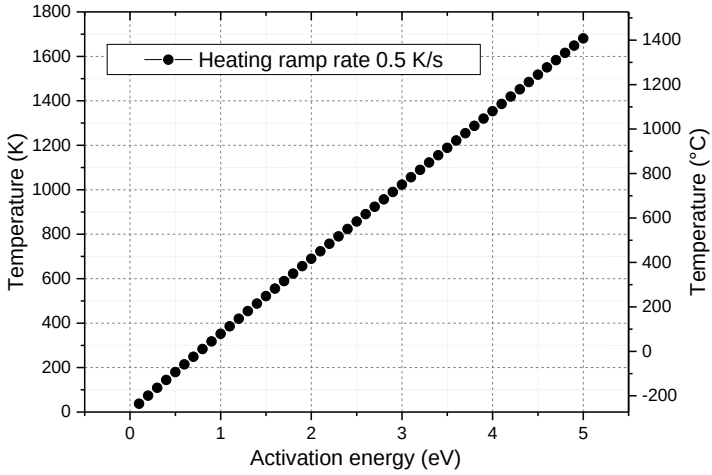

Figure 18 Correlation between peak temperatures and the activation energies for H obtained using equation (8)

By confronting the temperatures, corresponding to the peaks identified in Figure 16, on Figure 18, the activation energies of the peaks were found to be 1.6-1.7 eV for P_1, 1.9-2.0 eV for P_2 and 2.4-2.5 eV for peak P_3. By subtracting the value of the migration energy, one finds that the interaction energy corresponding to those traps to be 1.2, 1.6 and 2.1 eV. These energies are somewhat higher than the *ab initio* values reported for the H-dislocation, H-vacancy and chemisorption energy (0.45-0.9 eV [48, 68], 1.24±0.5 eV [32, 36, 69] and 2.0 eV [32]). However, the applied approach is oversimplified because it describes simultaneous release of H from traps without accounting for the diffusion to the surface and re-trapping. The latter processes lead to the delay in the release of H, hence the activation energy obtained using equation (8) is the upper bounds. A better estimation of the activation energy would require TMAP (Tritium Migration Analysis Program) modelling [70], which however needs a spatial distribution of D. While, the integral spatial distribution of D could be obtained using NRA analysis (some examples are provided further), the assignment of D concentration in specific type of traps remains ambiguous.

While the existence of P_1 and P_3 can be explained by the presence of dislocations and eventual formation of pores under high flux exposure, the peak related to the presence of vacancies or small vacancy clusters should be clarified. Indeed, prior the exposure the samples were annealed, so that the defects originated from the EDM cutting must have been removed. The annealing of the material was at a temperature of 1273 K, well above the temperature

corresponding to the migration energy of vacancy (about 600 K which according to Figure 18 corresponds to 1.78 eV reported in [71]). After cutting the samples, the surface was carefully treated to remove the roughness induced by the electric discharge machine, hence we do not expect the presence of vacancies in our materials before the exposure. Yet, the position of P_2 points to the activation stage with the trapping energy similar to the one calculated for the vacancy. Its possible origin will be discussed a later, after the results for different exposure fluences are presented.

Figure 19 presents TDS results for reference and plastically deformed samples exposed to fluence of F=8×10^{24}, 5×10^{25}, and 3.5×10^{26} D/m^2 obtained one week after the exposure. It can be seen from the graphs that the absolute positions of the peaks slightly depend on exposure conditions and are located in the following approximate ranges: P_1=550-650 K, P_2=700-800 K and P_3=850-1000 K.

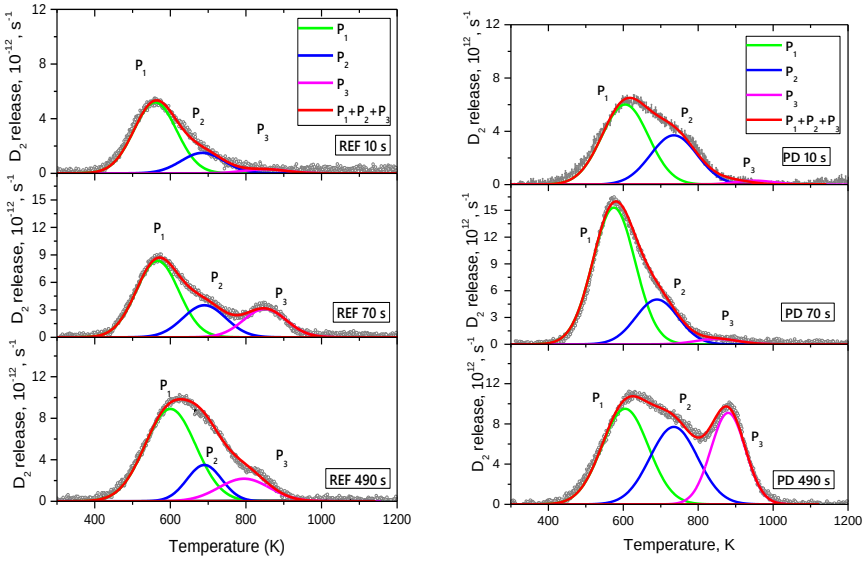

Figure 19 Experimental TDS spectra of deuterium release from reference recrystallized (REF) and plastically deformed (PD) polycrystalline DF W samples exposed to fluence of F=8×10^{24}, 5×10^{25}, and 3.5×10^{26} D/m^2, which correspond to 10, 70 and 490 s of exposure time, respectively, at a flux of (0.8-1.0)×10^{24} D/m^2/s

According to Figure 19, vacancy-like traps are present in both reference recrystallized and plastically deformed sets of samples. It is important to note,

that the equilibrium vacancy concentration at temperatures below 1000 K is extremely low and cannot explain the amount of stored D, as has been analyzed and discussed in [48]. Therefore, we attribute the peak P_2 to the storage of D in small clusters located on dislocation lines which assist the nucleation of plasma induced defects (vacancy-jogs). Hence presence of P_2 and its intensity is linked to the capacity of dislocation lines to act as traps. The increase of dislocation density in the sub-surface region after high flux plasma exposures is attributed to the thermal stresses and subsequent plastic deformation [72].

The mechanism of hydrogen isotopes trapping mediated by dislocations is proposed to be the following: The result of the condensation of migrating D atoms on dislocation lines is the formation of D_N clusters, attached to dislocations, as DFT calculations suggest the presence of the attractive interaction not only for an isolated D but for small clusters as well [48]. Further extension of a D_N cluster along the dislocation line will result in the cluster size growth and its immobilization at the dislocation line. The growth of a stable and immobilized D_N cluster should eventually result in the punch of the tungsten atom and creation of vacancy-D_N complex which will further growth by absorption of D atoms coming from bulk and those which migrate along the dislocation lines.

Dedicated computational assessment [73] was performed to analyze possible mechanisms of nucleation of thermally stable D-vacancy clusters on dislocation lines. The critical conditions for the nucleation of D-vacancy clusters were analyzed and current exposure conditions were found to satisfy the nucleation criterion [73].

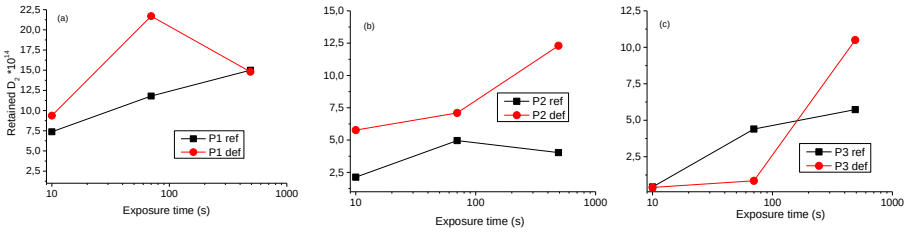

Figure 20 Integrals of the three Gaussian functions ((a) P_1, (b) P_2, and (c) P_3) constituting the TDS spectra measured in the reference recrystallized (REF) and plastically deformed (PD) samples as a function of the exposure time

As it can be seen on Figure 20, defects created by the plastic deformation cause the increase of the contribution of P_1 and P_2 to the total retention. This observation supports the hypothesis that these release stages are determined by the dislocation-type microstructure, as these are the primary defects generated

by the plastic deformation. At the same time, peak P_3 is totally suppressed up to exposure time 70 s for the plastically deformed sample, and only up to 10 s for the reference recrystallized one. Keeping in mind that the release at P_3 is associated with the presence of bubbles/pores, we can conclude that the plastically-induced dislocation network somehow delays the transformation of D-vacancy-like clusters into bubbles and/or suppresses the bubble growth rate.

The data shown on Figure 21 compares the total retention in the reference recrystallized and plastically deformed samples. According to the data presented, the retention in both types of samples is not yet saturated even after exposure during 490 s. At the same time, the application of plastic deformation increases the total D retention by about 50%, which is observed for each investigated exposure fluence.

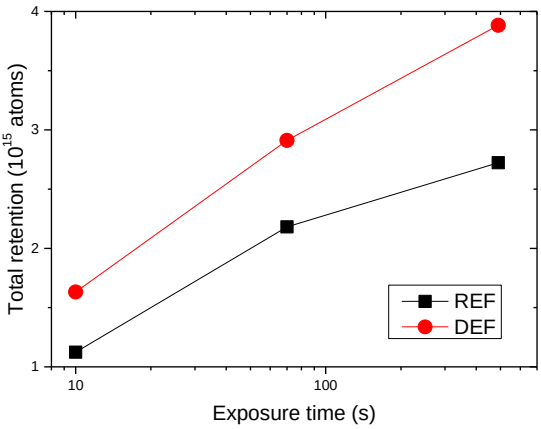

Figure 21 Total deuterium retention in reference recrystallized and plastically deformed samples

3.2.2 Impact of plastic deformation and exposure temperature on D retention, studied at fixed fluence (10^{26} D/m^2)

The impact of plastic deformation and exposure temperature on D retention was studied after a set of dedicated plasma exposures. The average particle flux across the sample was (0.9-2.8)×10^{24} D/m^2/s, fluence F=10^{26} D/m^2, exposure temperatures 460, 600, 820 and 1000 K.

Following the previous analysis, where it was discussed that P_1, P_2 and P_3 can be attributed to the detrapping from dislocations, vacancies/D clusters and voids, the TDS data was deconvoluted into three Gaussian peaks. The data for

reference recrystallized samples is presented on Figure 22, and for plastically deformed – on Figure 23.

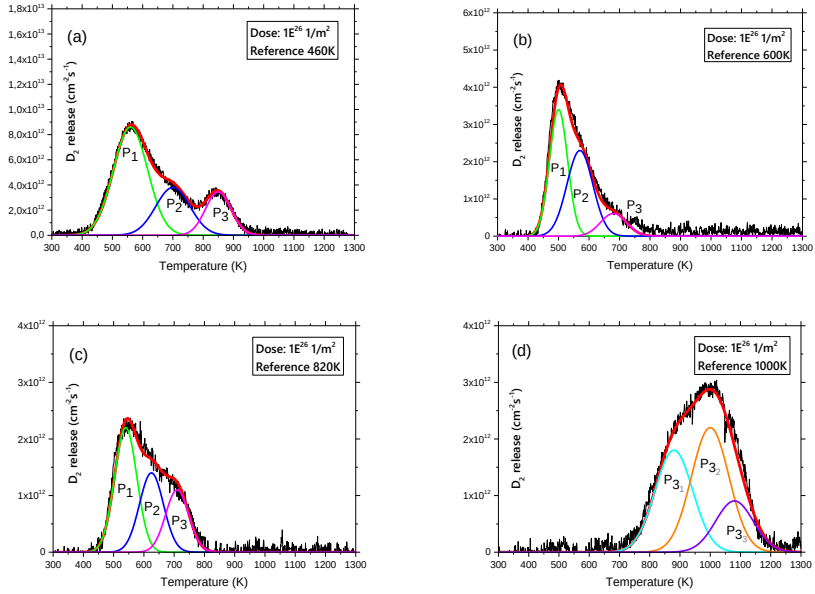

Figure 22 Deconvoluted TDS spectra of the reference samples exposed at (a) 460 K, (b) 600 K, (c) 820 K and (d) 1000 K. The black curve corresponds to the experimental data, the red curve is the superposition of the Gaussian functions. The latter are shown by green, blue and magenta, attributed to release stage P_1, P_2 and P_3 respectively

As it can be seen from Figure 22 and Figure 23 that exposures at low temperatures result in the appearance of three release peaks located around 450-550 K, 600-700 K and 700-800 K. After the exposure at 1000 K, no peaks below 700-800 K were observed, the major release occurs in the range of 700-1200 K, and it is therefore attributed to the detrapping of D from pores. The positions of the peaks slightly move from one exposure to another, but no clear trend can be observed.

The broadening, shift towards high temperature and increase in P_3 intensity, responsible for the detrapping from pores, after exposure at 1000 K indicate deep diffusion and storage of D in large bubbles. Note that a single Gaussian function is not enough to describe the experimentally measured desorption at 1000 K and, therefore, we divide P_3 into three sub-peaks. The appearance of the extra sub-stages, visible on Figure 22 (d) and Figure 23 (d), could be explained by the presence of a bi-modal size distribution of bubbles (will be discussed in a Section 0), which results in the delayed release from larger

bubbles. *Ab initio* and molecular dynamics simulations [73] demonstrated the tendency of H to occupy off-centered positions in a vacancy, due to its weak attraction to tungsten atoms [36, 74]. This indicates that H atoms, when filling a void, will first occupy the positions on the inner surface and then fill the center. As it will be discussed below, the increase of the bubble/pore size will lead to the delay in the maximum release temperature in the TDS spectrum. Detailed theoretical argumentation and estimation of the shift of the release peak is provided in [73], here we refer to the brief details.

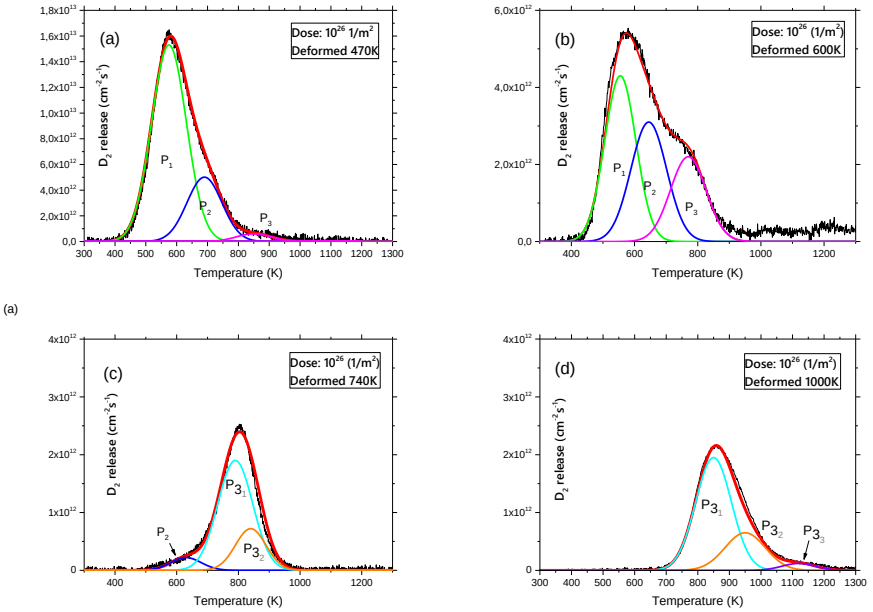

Figure 23 Deconvoluted TDS spectra of the plastically deformed samples exposed at (a) 470 K, (b) 600 K, (c) 740 K and (d) 1000 K

The increase of exposure temperature facilitates D diffusion. Detrapping from dislocations at higher temperatures results in the nucleation of bubbles mainly at strong traps such as grain boundary triple junctions and other bulk imperfections with a considerable open volume. Therefore, the bubble density reduces with raising the exposure temperature. As the bubble density reduces the rate of growth increases (because the lower number of bubbles share the same upcoming flux) and therefore the resulting mean size increases [73].Taking into account a significant difference in the bubble size (e.g. 10 vs. 100 nm), quantitative estimations based on atomic scale modeling [73] suggest the release peak can be shifted in a range of 100 K. This observation is in line with the spacing of P_{3_1} and P_{3_2} observed in our work. The presence of the bubbles was

indeed revealed in our samples after the plasma exposure by TEM [59], but a systematic analysis was not done. The TEM investigation including scanning of different depth regions would require enormous amount of work and was out of scope of the present PhD project.

Given that the relatively large bubbles (range of 10-100 nm) were indeed observed by TEM, three sub-peaks observed after the highest temperature exposures, could be attributed to the release from families of pores with different sizes. The reason for the occurrence of multi-modal size distribution of pores can be related to the gradients of temperature from the exposed surface to the cooled base. Such that the high temperature region (closer to the surface) exhibits smaller density of large pores, whereas a colder region has smaller pores (resulting from the growth of the vacancy-D clusters).

During the exposure, all penetrated D atoms can be sub-divided into those which are already stored in traps and those which remain as interstitials and diffuse in the lattice. As it was described in section 2.4, a very fast cooling process (2-3 s) can influence the mechanism of (de)trapping of atoms, since this time is not enough for all interstitial D atoms to reach the surface and escape from the material. As a result, a fraction of diffusing interstitials is getting to be trapped by available microstructure (e.g. dislocations) in the quickly cooling material. Naturally, those traps were not active during the exposure. As a result, the TDS shows the release of D at temperature below the surface temperature during the exposure, which manifest the release of D trapped during the above discussed cooling phase. This effect is clearly seen on Figure 22 and Figure 23 for plasma exposures performed above 600 K, when the release starts at the temperatures below exposure ones. Moreover, D diffusion from the bulk towards the surface will be accompanied by the frequent re-trapping events at microstructural defects already emptied from D. This is another reason for the occurrence of the delay in the release (and hence shift of the release peak) in the case of the high temperature exposure.

Figure 24 presents the D releasing stages, defined as an integral under the Gaussian function attributed to a certain stage and expressed as % of the total retention. A number of general trends can be identified:

- The intensity of P_1 becomes negligible at 1000 K. Consequently, the mechanism of detrapping from dislocations is no longer effective at exposure temperature above 820 K. Since grain boundaries are stronger traps than dislocations (0.45-0.9 eV [48, 68] and 2.0 eV [32] respectively), the fraction of D trapped by grain boundaries increases with the temperature. The diffusion towards bulk in this case is probably controlled by trapping at and diffusion along grain boundaries.

- The intensities of P_2 and P_1 show similar trend. With respect that the P_2 release stage is attributed to the detrapping from vacancy-jog clusters, it is natural to expect that the deactivation of dislocation trapping above 800 K will also eliminate the formation of dislocation-attached defects.

- P_3 intensity increases with exposure temperature and reaches 100% after the highest temperature exposure. Nanometric bubbles and larger cavities, correlated with this peak, contribute to the formation of sub-surface blisters (See section 0) and to the delayed release from the bulk material due to the presence of re-trapping processes.

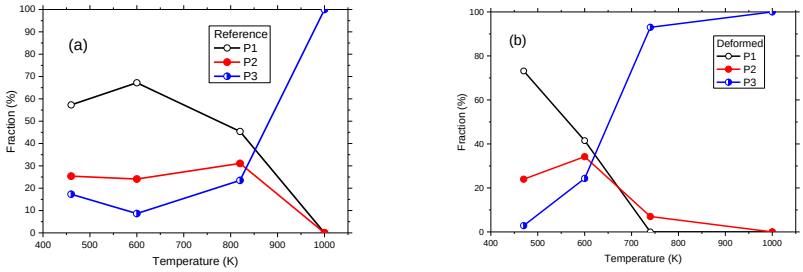

Figure 24 Fraction of D integrated over the Gaussian functions assigned to the release at stages P_1, P_2 and P_3 in (a) reference and (b) plastically deformed samples

As fractional contribution of the first peak prevails at low temperatures and then disappears with the increase of the exposure temperature, we can assume that this feature characterizes the change in the major trapping and diffusion mechanisms. This change happens in the temperature range of 600-820 K and depends on the dislocation density.

Figure 25 shows the data for the total retention of our experiments compared with data from high-flux and medium-flux exposures reported in literature. The results obtained within this study are in reasonable agreement up to 600 K with the data reported in other works involving medium flux (10^{22} $D/m^2/s$) and the same fluence as in the present case. Retention after higher temperature medium flux plasma exposures decreases significantly (by at least one order of magnitude), while in our study the saturation is recorded. Other studies after high flux exposures [75, 76] reported the similar trend for the saturation of total retention at 600-1000 K, despite the fact that polycrystalline tungsten used had different origin and purity (99.95% in [75], 99.94% in [76] and 99.97% here). Hence, the difference in the total retention measured in the

exposures above 600 K after medium and high plasma flux can be attributed to the effect of flux rather than impurities or possible microstructural differences.

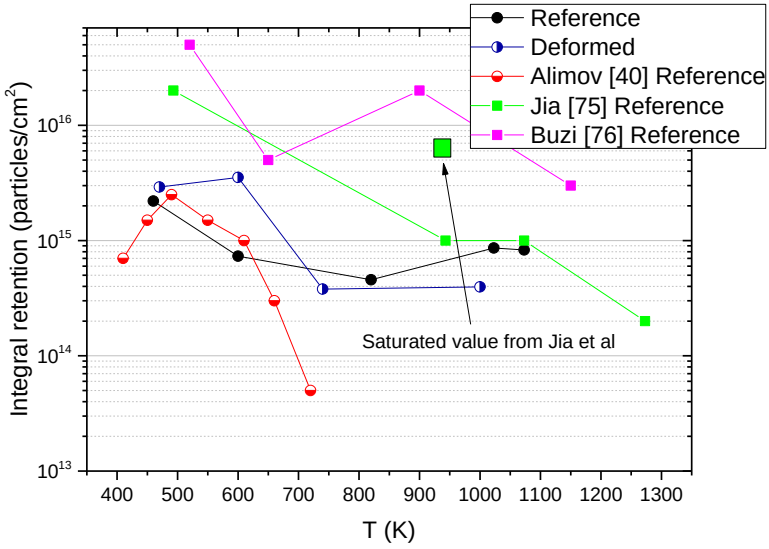

Figure 25 Total retention measured in this work as compared with the data reported in literature [75, 76], obtained in similar exposure conditions and comparable W grades (except from the work of Alimov et al. [40], where a lower flux was applied). The data point labeled as "Saturated value from Jia et al." corresponds to the retention measured at the fluence of 5×10^{26} D/m^2, at which the saturation of the retention has been identified to take place

The difference with the results obtained in [75] and [76] can be related to the difference in beam profile, sample thickness, etc. The specimens used in [75] were discs with diameter of Ø30 mm, in [76] – Ø14 mm disks, in the current study we used square tungsten samples with the dimensions 10×10×1 mm. Correspondingly, the exposure surface was larger in those works as compared with our samples. In addition, different sample geometry could result in different temperature distribution across the sample depth and therefore could also impact the total amount of D trapped.

3.2.3 Impact of plastic deformation and plasma composition, studied at baseline exposure conditions (T=470 K, fluence 5×10^{26}- 1×10^{27} D/m^2)

The retention of deuterium and helium in tungsten after high flux pure He, pure D and mixed beam plasma exposures is presented in this sub-section. Two pairs of samples (reference recrystallized and plastically deformed) were used to reveal the impact of material microstructure on the trapping and release of He and D.

The parameters of pure He and D exposures at the linear plasma generator Pilot-PSI are demonstrated in Table 2. Special care was taken to perform all exposures as close as possible to 470 K temperature to remain consistent with the previous studies [48, 77, 78]. As it was described earlier in section 2.4, Pilot-PSI is a unique machine in term of providing an ultra-high flux, but the precise control of surface temperature is a difficult task. Many parameters can influence the temperature of the sample, and plasma conditions is one of them. That is why, the surface temperature in the case of He exposures was slightly different from that of D exposers. However, the difference of 10 K should not impact the conclusions.

Table 2 Summary of the parameters of pure He and pure D exposures.

Microstructure (REF/PD)	Gas (He/D)	Flux (ions/m^2/s)	Fluence (ions/m^2)	Time (s)	Temperature (K)
REF	D	1.0×10^{24}	4.9×10^{26}	490	470
PD	D	1.0×10^{24}	4.9×10^{26}	490	470
REF	He	2.1×10^{24}	6.3×10^{26}	300	480
PD	He	2.1×10^{24}	6.0×10^{26}	300	480

The TDS spectra for the reference recrystallized and plastically deformed samples are shown on Figure 26. It can be clearly seen that plastic deformation enhances integral retention in case of pure D exposure, while in the case of pure He exposure the effect is opposite.

Plastic deformation does not influence the deuterium release up to about 600 K. The release from voids is well known to occur in the temperature range of 800-1000 K [79], thus the clearly pronounced peak around 900 K in case of plastically deformed material most likely corresponds to the D desorption from voids. The high temperature peak in case of reference recrystallized material is

also present, but it is much less pronounced under the current exposure conditions.

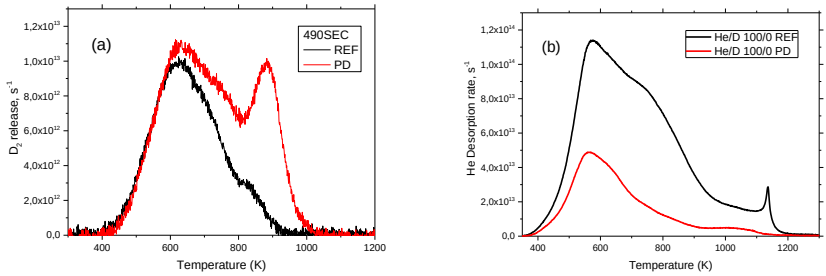

Figure 26 Comparison of TDS spectra after pure D (a) and pure He (b) exposure of both reference recrystallized and plastically-deformed samples

In case of pure He exposure, the reduction of He retention observed over the whole TDS temperature range. Plastic deformation seems to have no influence on the position of the release peaks. Thus, the following conclusion can be made: the origin of crystallographic defects which trap He atoms is the same for reference recrystallized and plastically deformed material. The dislocation network induced by the plastic deformation, clearly does not change the mechanism of trapping but somehow affects its intensity. This can be explained by either the nucleation or growth rate of He bubbles which are affected by a high density of dislocations. Assuming the dislocations can act as channels for fast diffusion of He in and outside the material, the nucleation of He clusters in subsurface area would indeed be suppressed.

The TDS spectra and the Gaussian fits for all four samples are given on Figure 27. Each symmetric Gaussian fit reasonably reproduces the TDS spectrum, except for a sharp and narrow peak around 1150 K for the reference recrystallized He exposed sample. Similar spikes were also noticed in the previous study [46] for pure recrystallized tungsten, however, their origin was not discussed. It can be assumed that such a sharp release is induced by the direct migration of He bubbles (due to the diffusion of He and W atoms on the internal surface of a bubble), which in turn leads to an abrupt increase of the release rate, contrary to the more gradual atomic evaporation (atom by atom) of He from He bubbles.

In case of pure D exposure, the release peaks are located around 600 K, 690-730 K and 840-880 K, meanwhile in the case of pure He exposure – around 570 K, 750 K and 1020 K (which, according to Figure 18, corresponds to 1.6, 2.2 and 3.1 eV). He-dislocation, He-vacancy and chemisorption energies obtained by *Ab*

initio calculations are equal to 1.32 eV, 4.55 eV [67] and 4.7-5.0 eV [80, 81]. The release stages are quite close to the results reported previously studying He release after plasma exposure at 1300 K [46]. The difference is seen for the low temperature release stage, which is found to be around 330–350 K [46]. This distinction might be caused by the difference in the exposure temperatures, which resulted in the formation of fuzz in the case described in [46], and not observed in our study. The positions of the high temperature peaks, described in [45, 46] and situated in the range of 800-1200 K, broadly agree with the ones observed in the present work.

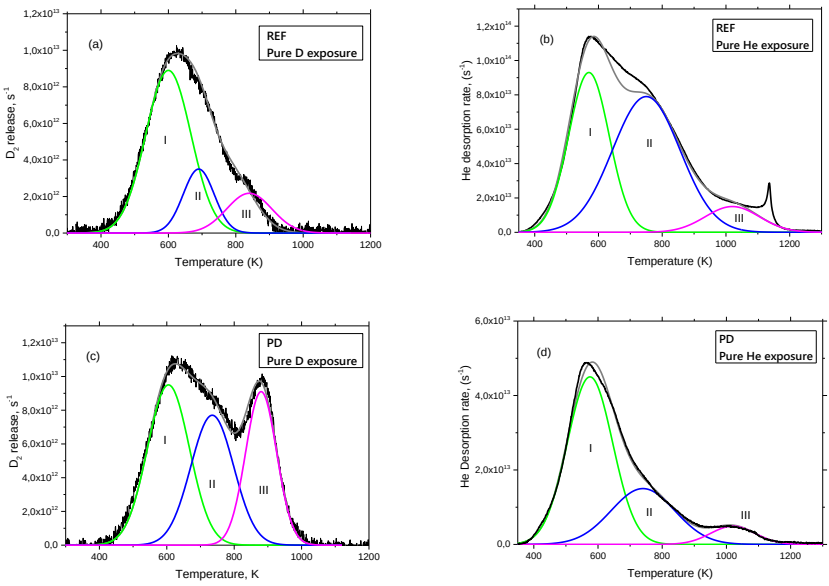

Figure 27 Decomposition of TDS spectra on the sub-stages. (a,c) D-exposed samples, (b,d) He-exposed samples

It has to be mentioned, that the release of D is completed within about 1000 K, which is in line with many previous studies done after pure D exposure (see e.g. [51, 82]). While the release of He could be uncompleted due to the technical limitations of the maximum temperature of TDS setup (1300 K). In earlier works involving He plasma exposures, He release was observed above 1300 K (see e.g. [83]). Thus the final conclusions can be only done after performing TDS up to 2000 K.

The total retention in the two pairs of samples is compared on Figure 28. It is clearly seen that plastic deformation suppresses He retention by a factor of

three. Assuming that He release is not yet finished, a fraction of He is very likely still retained in the material.

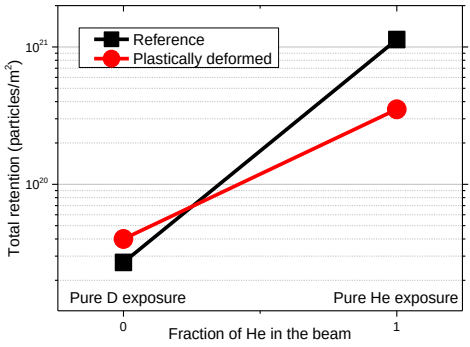

Figure 28 Comparison of the release of D_2 and He calculated on the basis TDS

The parameters of mixed beam plasma exposures are summarized in Table 3. He-to-D gas ratio was varied as 0/100, 40/60, 60/40, 80/20, 100/0 to investigate the impact of gas composition on He and D trapping. The first set of experiments were performed using high resolution TDS, which is sensitive enough to discrete He and D_2 masses, and included tungsten samples in reference recrystallized condition. During the second set of experiments reference recrystallized and plastically deformed samples were investigated using regular TDS. All results presented below, which were obtained by regular QMS, report D_2 release rate.

Figure 29 demonstrates the TDS spectra for He and D release after pure He, pure D and mixed beam exposures measured by high resolution TDS.

Figure 29 (a) presents the desorption rate of He. It can be seen that He release starts earlier in the case of mixed plasma (60% and 80% He in gas), in comparison to pure He exposure. This could be attributed to the formation of mixed He-D clusters, where the binding of He is lower as compared to pure He clusters. As demonstrated in [84], a single interstitial hydrogen is attracted to He-vacancy (or just substitutional He atom) with the energy of about 1 eV, which then decreases for a larger number of He atoms, allowing to accommodate up to 12 hydrogen atoms near a single substitutional He. The complete matrix of He_NH_M-vacancy cluster is computationally assessed in [69], it was demonstrated that the binding energy for He in the cluster $N + M \leq 6$ steadily decreases (by about 0.1- 0.2 eV) with the increase of the number of H atoms in the cluster. With that, it was shown that removing a He atom from a mixed He_xH_yV cluster requires always more energy (between 2 and 3 eV more) than removing an H atom from

a cluster of identical size. Thus, it can be concluded that an alternative interpretation of the observed results is possible. For example, it could be related to a diffusion mechanism attributed to the dislocation network or He depth distribution.

Table 3 Summary of exposure conditions. First experimental run: high resolution TDS (HR TDS), reference recrystallized (REF) samples; second experimental run: low resolution TDS (TDS), reference recrystallized (REF) and plastically deformed (PD) samples.

Set	Material (REF/PD)	He fraction in gas (ion%)	Flux (ions/m^2/s)	Fluence (ions/m^2)	Time (sec)	Temp. (K)
#1 HR TDS	REF	40	1.8×10^{24}	8.9×10^{26}	500	560
	REF	60	2.6×10^{24}	1.2×10^{27}	500	560
	REF	80	2.6×10^{24}	1.3×10^{27}	500	530
#2 TDS	REF	40	2.0×10^{24}	5.8×10^{26}	300	500
	REF	60	1.8×10^{24}	5.2×10^{26}	300	480
	REF	80	2.1×10^{24}	6.4×10^{26}	300	460
	REF	100	2.1×10^{24}	6.4×10^{26}	300	480
	PD	40	2.0×10^{24}	5.9×10^{26}	300	515
	PD	60	1.7×10^{24}	4.9×10^{26}	300	500
	PD	80	2.1×10^{24}	6.2×10^{26}	300	475
	PD	100	2.0×10^{24}	5.7×10^{26}	300	480

The main He release stage in case of mixed beam exposures is situated around 550 K, and its intensity increases with the fraction of He in the beam. The second He release stage is around 800 K, it is much less evident after mixed beam exposure compared to pure He. It is also important to mention that reaching the highest technically achievable temperature of 1300 K, He release is still not completed, as follows from Figure 29 (a).

Desorption rate of D is presented on Figure 29 (b), where two release stages (around 500 K and 800 K) can be distinguished. In case of pure D exposures, they are attributed to the detrapping from dislocations and small D-vacancy clusters [85]. Addition of at least 60% of He in the mixed plasma beam results in significant increase of stored D. This is obviously the influence of He, which enlarges the formation of defects that release D upon annealing up to 1000 K. For all He-to-D ratios, D release is completed at around 1000 K. We suggest that the

fact, that D retention is higher after pure D exposure compared to 40% He/60% D, can be explained by the difference in total D fluence achieved by the samples.

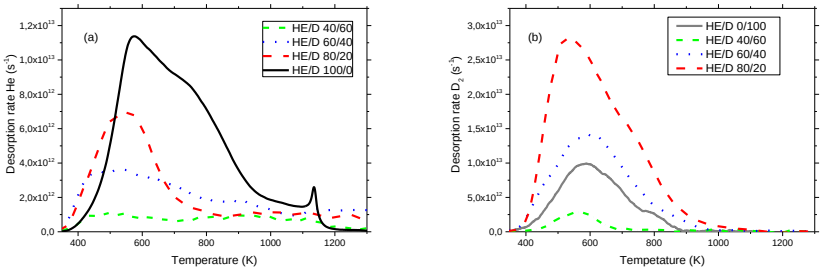

Figure 29 Release of (a) He and (b) D_2 from the reference samples exposed to the mixed plasma beam. The results for mixed beam were measured by high resolution QMS

The desorption rates of He and D (measured by high resolution TDS simultaneously) for each case of mixed beam exposure shown on Figure 30 allow one to compare the dynamics of He and D release.

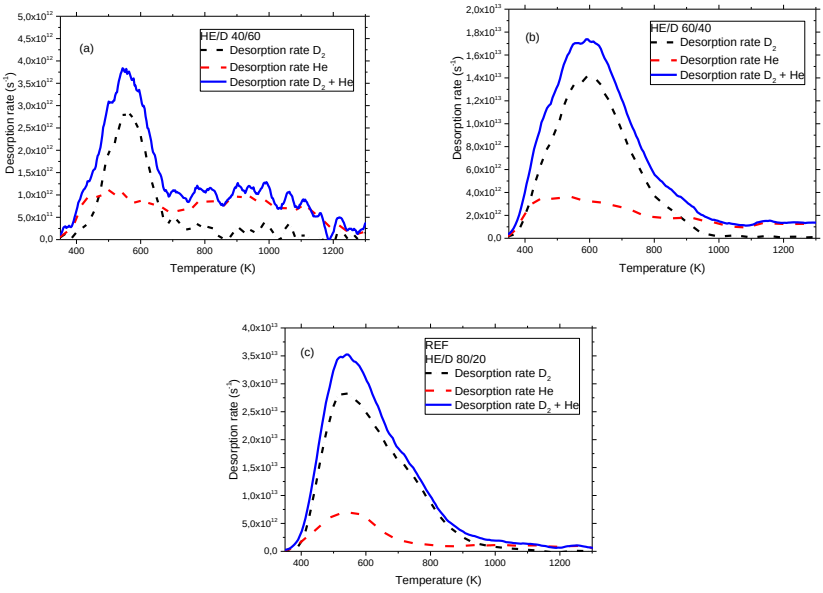

Figure 30 Comparison of the release of He and D_2 measured by the high resolution QMS from the reference samples exposed to the mixed plasma beam with He fraction in gas of 40% (a), 60% (b) and 80% (c)

The results of 40% He/60% D exposure are shown on Figure 30 (a). He release starts around 350 K, while the onset of the release of D is only around 400 K. This lag can be attributed to the lower migration energy of He as compared to atomic hydrogen (i.e. 0.06 eV vs. 0.25-0.4 eV [86, 87]), so that when the vacancy-like defects are filled with several He/D atoms, the first detrapping events are defined by the difference in the migration energy. The interaction of hydrogen with dislocations, according to the available computational data (e.g. [48]), can be different, e.g. hydrogen can diffuse along the dislocation core lines while being trapped at them. Here trapping means affinity of H to dislocation core, however affinity to the core does not prevent the migration along the core. Hence, the presence of the dislocation network caused by applying plastic deformation may indeed impact the depth distribution.

Apparently, the equilibrium of He-D clusters changes with the increase of He fraction in the plasma beam, and the release of D and He starts at the same temperature in case of other He-to-D ratios (Figure 30 (b) and Figure 30 (c)). To clarify this assumption further exposures involving a lower He-to-D ratio should be performed.

It is clearly seen for each case of the beam composition from Figure 30 that D release is generally completed within 1000 K and every time there is a cross-over point between D and He release. This cross-over point moves towards a higher temperature with the increase of the fraction of He in the beam, and reaches 1000 K in the case of 80% He/20% D. This implies that the higher He-to-D ratio, the stronger D trapping.

Another important observation is the increase of the D low temperature (500-600 K) peak contribution with the increase of He fraction in the plasma beam.

Lower intensity of the release rate in case of He-to-D ratio of 40/60 compared to other fractions can be explained by shorter time between plasma exposure and TDS measurement. The 40% He and 60% D sample was measured the same day as the exposure was performed, meanwhile, due to the busy schedule, the two others were only measured 11 days after.

Figure 31 presents the aggregated He+D_2 release measured by regular QMS (calibrated for D_2) for the mixed beam exposures with He fraction in gas of 40% (a), 60% (b) and 80% (c). Since the masses of He and D_2 cannot be distinguished by regular QMS, the data presented is the sum He+D_2. Each graph compares reference recrystallized and plastically deformed samples exposed at similar conditions.

According to the results presented, plastic deformation leads to the suppression of He+D uptake in each case of mixed beam exposures, whereas the

impact of deformation after the pure D exposure is the opposite. The major release peak, located around 500 K, does not shift in reference and plastically deformed samples irrespective of the He-to-D ratio.

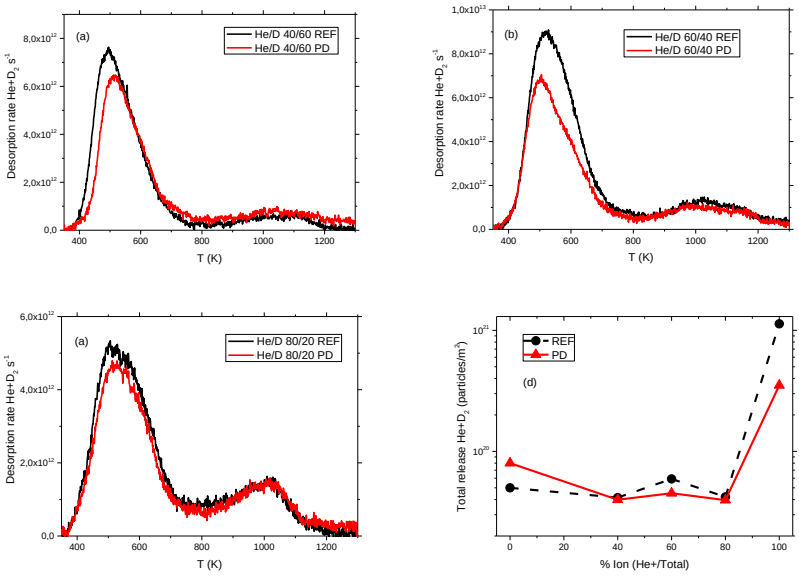

Figure 31 Comparison of the He+D_2 release measured by the regular QMS (low resolution TDS) from the samples exposed to the mixed plasma beam with He fraction in gas of 40% (a), 60% (b) and 80% (c). (d) The total release He+D_2 (i.e. integrals of the functions presented in fig. (a), (b), (c)) measured in reference and plastically deformed samples

Figure 32 summarizes the total release of He and D_2 measured by the high resolution QMS in reference samples. The impact of the He seeding is much more pronounced as compared to the above discussed effect of the plastic deformation. In case of pure He and D exposures, taking into account the comparable total fluences of ions (i.e. sum of D and He), the release changes by one order of magnitude going from about 10^{20} D/m^2 up to 10^{21} He/m^2. In the case of mixed plasmas, He seeding results the enhancement of D trapping (as measured by the D release), despite the lower fraction of D in the beam. Thus, He practically controls D trapping under selected plasma exposure conditions. This suggests that the binding of D with self-trapped He clusters and formation of He-D-vacancy clusters by punching self-interstitials in tungsten bulk is the major mechanism of D trapping (see review [41]).

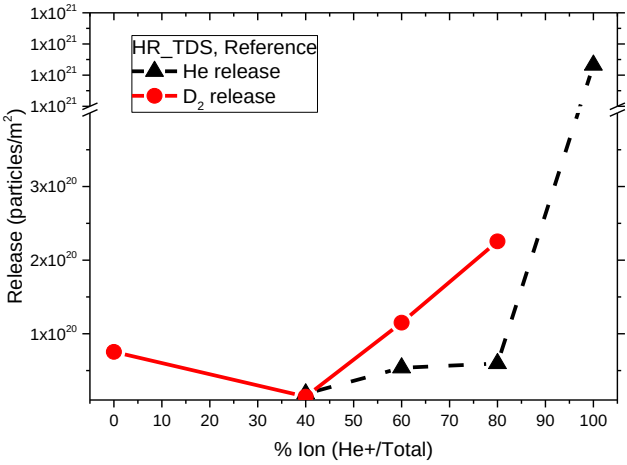

Figure 32 Comparison of the separate release of D_2 and He measured by the regular QMS from reference samples exposed to the mixed plasma beam with He fraction in gas of 40%, 60% and 80%

3.3 Complementary experiments – SEM, NI, NRA, TEM

This section presents the data obtained using complementary techniques, such as SEM, NI, NRA and TEM, to support the results and discussion in the section 3.1. Due to the tight schedule of the cycle "Plasma exposure - TDS" (to have the same time in between for all samples), the study with the complementary experimental techniques was not systematic. Also, during the PhD thesis, the Pilot-PSI device has been transferred from Nieuwegein to Eindhoven, which created a significant time gap for the access to the high flux plasma facility. The NRA and nanoindentation were applied later on some samples which were re-exposed to achieve as close as possible conditions to those presented in section 3.2. Because of this complications, this section contains a set of demonstration measurements rather than a systematic set of results.

3.3.1. Modification of surface hardness revealed by nanoindentation

In this section we demonstrate the results of nanoindentation of tungsten before and after plasma exposure. The usage of nanoindentation to characterize the plasma damage is applied here to validate the applicability of this techniques to sense any changes in the micro-mechanical properties of materials. At the moment when this work has started (in 2014), we could not find results of nanoindentation applied to characterize the hardness of (high flux) plasma exposed tungsten.

3.3.1.1 Modification of surface hardness induced by D plasma

The outer surface of tungsten, used as plasma-facing material, will experience cyclic heat loads, which can result in the nucleation of cracks and their propagation towards the bulk [88]. If penetrated plasma particles form nanocavities (likely hydrogen bubbles) [48], an increase of hardening of the material can be expected, which will occur due to constraining the dislocation-mediated plasticity. In this way, the release of thermo-mechanical stresses will be limited. If mechanical failure occurs, which is unacceptable for the proper functioning of armor material, a risk of plasma contamination and extra heat propagation will take place. Therefore, the understanding of the evolution of the sub-surface hardness after the plasma exposure is important.

It is known from the previous studies (e.g. [89, 90]), that hydrogen isotopes during high flux plasma exposure penetrate to the depth of about 5-10 μm only, thus the major amount of gas retained is stored within the first grain (or grains, if the material has fine grain structure). Conventional mechanical tests, such as Vickers hardness punch test or uniaxial tensile test, are not applicable to probe the surface hardness within such a shallow depth as 10 μm. The solution of this problem can be nanoindentation, which has a resolution of tens of nanometers, and therefore is a unique tool to understand the evolution of the sub-surface hardness.

There are three important quantities measured by nanoindentation: load P, displacement h and elastic unloading stiffness $S=\mathrm{d}P/\mathrm{d}h$ [56]. The accuracy of these data measurement defines the accuracy of hardness H and modulus E_{eff} [56].

The hardness can be estimated from:

$$H = \frac{P_{max}}{A}, \tag{9}$$

where P_{max} is the maximum load on samples and $A=F(h_c)$ is the contact area under load as a function of indenter geometry [56].

Estimation of the elastic modulus can be found from the relationship to contact area and unloading stiffness [56]:

$$S = \beta \frac{2}{\sqrt{\pi}} E_{eff} \sqrt{A}, \tag{10}$$

where β is a correction factor and E_{eff} is the effective elastic modulus defined as:

$$\frac{1}{E_{eff}} = \frac{1-\upsilon^2}{E} + \frac{1-\upsilon_{ind}^2}{E_{ind}} \tag{11}$$

E_{eff} takes into consideration the fact that the elastic displacement occurs in both the sample (with Young's modulus E and Poisson's ratio υ) and the indenter (with elastic constants E_{ind} and υ_{ind}).

On Figure 33 one can see the schematic representation of the process of nanoindentation for different microstructural state of tungsten material. The blue region underneath the indenter tip represents plastically affected volume which is known to be a factor of 5 to 10 of the indentation depth [91]. The response of the material is determined by the emission of geometrically necessary dislocations (GNDs) and their interaction with the original microstructure of the material. Depending on the depth of the penetration, the rate of GNDs emission changes (decreases with increasing the depths). Figure 33 (a) shows ideal crystal material without any natural defects such as dislocations or grain boundaries; Figure 33 (b) – recrystallized tungsten with large grains and therefore low grain boundary density; Figure 33 (c) – DF recrystallized tungsten with the presence of dislocations which remain because of the original mechanical deformation applied before the heat treatment; Figure 33 (d) - DF recrystallized tungsten after plasma exposure, where the dislocation density is reduced with the distance from the surface (this aspect of the microstructure will be discussed further in section 0 presenting TEM results). Figure 33 (e) and (f) represent the microstructure of IG tungsten before (high grain boundary density and low dislocation density) and after (high grain boundary density and high dislocation density) plastic deformation respectively.

For the ideal crystal, which does not have any statistically stored dislocations (SSDs), the response of the material (e.g. resulting hardness) is controlled only by the injection of GNDs by the indenter. As more crystallographic defects (SSDs) are present in the material, more pile-ups will be created by GNDs when reaching SSDs (here, SSD is a generic term applied to both bulk dislocations and dislocation walls forming grain boundaries).

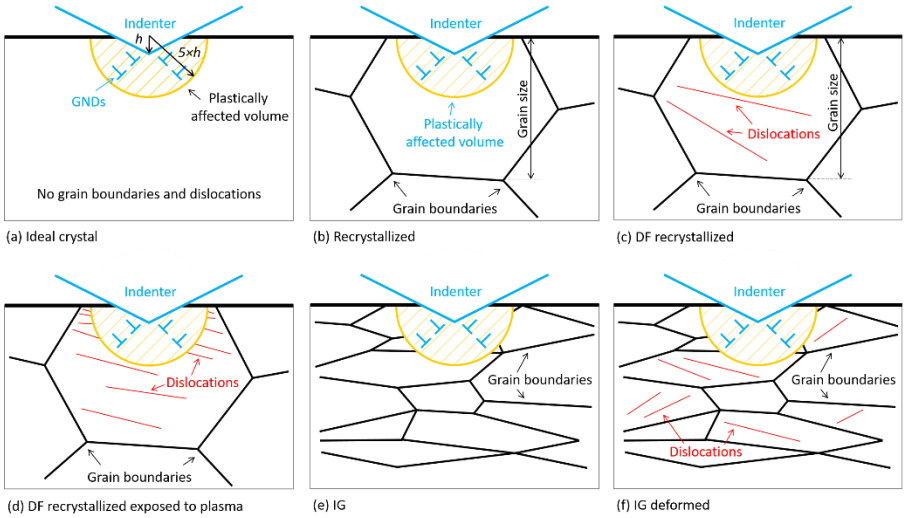

Figure 33 Schematic representation of nanoindentation for: (a) Single crystal, (b) recrystallized W without dislocations, (c) DF recrystallized W with dislocations, (d) DF recrystallized W exposed to plasma, (e) IG W with small grain size, (f) deformed IG W with small grain size and dislocations

The roughening of the surface amplified by the plasma exposure is unavoidable. Due to the imperfections of the contact surface, the absolute value of the Young's modulus E and the hardness H measured by nanoindentation contains intrinsic uncertainty [92-94]. As described in [94] and [95], the ratio of the hardness-to-reduced modulus, H/E_r^2, being independent on the contact area, can be used to avoid the uncertainties related to the surface roughness which interfere the accurate estimation of the actual contact area. In addition, H/E_r^2 value at a certain depth (being not more than 0.4-0.5 μm for reference recrystallized material), characterizes the resistance of material to the injection of GNDs and their further propagation into bulk. Schematic representation of H/E_r^2 as a function of indentation depth is shown on Figure 34, where region 1 corresponds to the shallow region of the measurement controlled by GNDs emission solely, region 3 corresponds to the case when the penetration is controlled by the interaction of GNDs with SSDs and therefore can be used to describe the microstructure and mechanical properties of bulk material; region 2 is the transition between the two above described. Typically, the region is located at the penetration depth of 100-500 nm, depending on the characteristic size of crystal defects (i.e. the spacing of bulk dislocations or the diameter of grain or sub-grain). The peculiarity of the plasma exposed material is that plasma exposure induces non-monotonic (with respect to the depth) deformation expressed in the strong increase of the dislocation density in the sub-surface region and its reduction to the nominal value at a depth of 10-15 μm. The

decrease of the dislocation density is nearly exponential with the penetration depth. Thereby, the characterization of the plasma impact requires testing material in region 1 and 2.

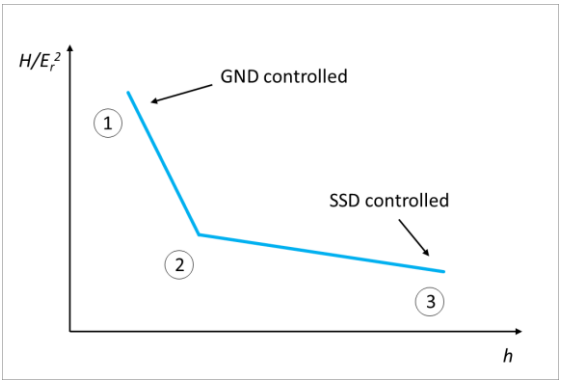

Figure 34 Schematic representation of H/E_r^2 (h) representation of results

Thus, a comparison of H/E_r^2 value in the reference and plasma exposed material can help to understand whether plasma defects indeed offer extra resistance to the plastic flow under the tip of indenter. The nanoindentation data obtained within this study will be presented in two ways: hardness H as function of penetration depth h and hardness-to-reduced modulus H/E_r^2 as function of h. The value of H_0, the hardness at the depth of 1500 nm (the maximum measured depth), will be given for each measurement.

Three samples (reference recrystallized and exposed to plasma at 460 K and 820 K up to fluence of 5×10^{25} D/m^2) were tested using nanoindentation. The data presented on Figure 35 (a) does not give a clear trend of hardness modification with exposure temperature. Therefore another method was used to clarify the impact of plasma exposure. It is clear from Figure 35 (b) that the effect of plasma induced damage is very pronounced within the first 100 nm, where the break on x-axis is applied to show the difference between the samples at the low-depths region and the results in depth). Deeper, all curves converge to the same value over the entire indentation depth. The size and density difference of plasma induced defects caused by exposure can be the reason for the deviation of the curves obtained after the exposure at 460 K and 820 K.

GNDs, interacting with SSDs, dislocation loops and cavities (the microstructural analysis will be presented in section 0), lead to the hardening of the material, which can be seen on Figure 35 (b) as an increase of H/E_r^2. However, the extension of this effect in depth is rather narrow.

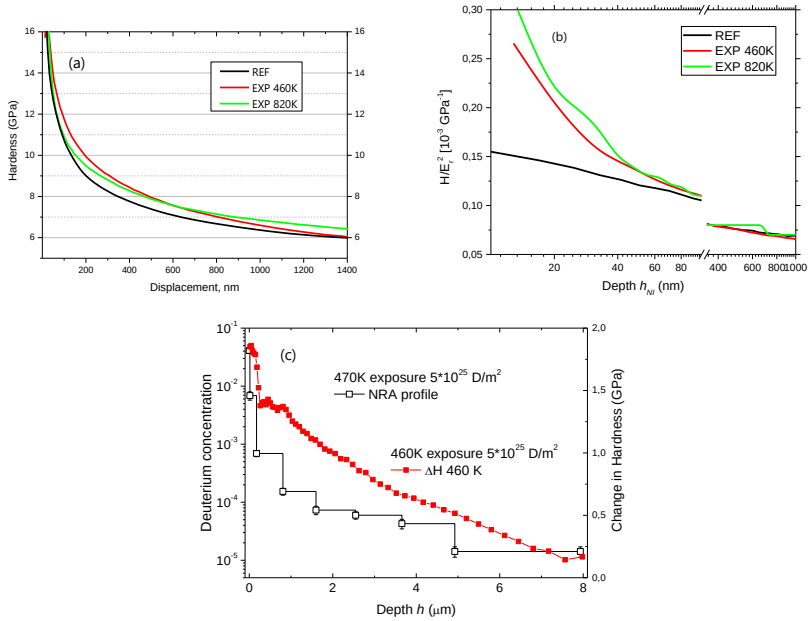

Figure 35 (a) H and (b) H/E_r^2 as functions of the indenter penetration depth, h. (c) NRA profile of D in W exposed at 470 K [96], compared to the change of hardness as a function of probed depth. h for NI measurements is scaled as h×5 to reflect the real volume probed by the penetrating indenter

NRA analysis is a conventional way to measure the sub-surface deposition of D. The results of NRA applied to the sample exposed under equivalent high flux plasma conditions are demonstrated on Figure 35 (c). The relative change in the hardness ΔH is also added in the figure, plotted versus the indentation depth. As it was mentioned before, plastically affected volume is about 5 times larger than the indenter penetration depth [91]. Thereby, h is multiplied by 5 in this representation. Clearly, the deuterium deposition, measured by NRA, is in good correlation with the plasma induced hardness increase. And since these two value are shown on difference scales, it can be concluded that surface hardness is proportional to the logarithm of deuterium concentration. Therefore, the increase of hardness can be attributed to the presence of plasma induced defects, which provide extra resistance to penetration of GNDs. The relative change in hardness ΔH is in good correlation with the data reported in [97] for the similar exposure conditions (450 K and 5×10^{25} ions/m^2).

As will be shown later in section 0, the TEM analysis of the exposed surface and sub-surface region reveals that in the current plasma exposure conditions, the main microstructural defects were dislocation networks and cavities/bubbles (with rather low density under pure D exposure). Hence, these

defects are apparently responsible for the modification of the sub-surface mechanical properties.

Figure 36 (a) and (b) compare the change of hardness and H/E_r^2 with the dislocation density measured by TEM as a function of penetration depth (see section 0). ΔH is seen to correlate well with the trend of the reduction of the dislocation density as the indentation depth is increased. One can see that $\Delta H/E_r^2$ is non-negligible only within the first 0.5 μm from the surface, which corresponds to the dislocation density of about 3×10^{13} m^{-2}. As soon as the dislocation density drops below $\sim2\times10^{13}$ m^{-2}, the two materials demonstrate equivalent response even at rather shallow depth, when the indentation corresponds to region 2 (see Figure 34). Based on this results, we conclude that the strong increase of the dislocation density in the surface and sub-surface region can be detected by nanoindentation. However, it is difficult to ascribe specific mechanical properties (hardness or modulus) to it because the impact of the plasma exposure occurs only at a very shallow depth where the response is primary driven by the emission of GNDs.

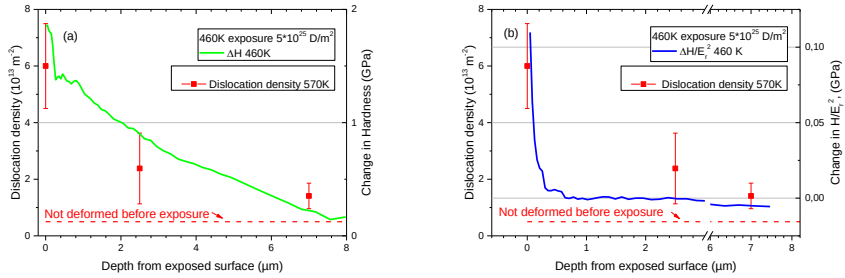

Figure 36 The change of (a) hardness and (b) H/E_r^2 as a function of probed depth compared to the dislocation density h for NI measurements is scaled as h×5 to reflect the real volume probed by the penetrating indenter

3.3.1.2 Modification of surface hardness induced by plastic deformation and annealing

To confirm that the increase of hardness after plasma exposure is indeed due to the increased dislocation density, a number of experiments was performed on the samples, annealed and pre-deformed to 4% and 9%. The purpose of those nanoindentation tests was to understand how the response of the material depends on the dislocation density. It is important to mention that no more reference recrystallized DF material was left at that moment, and another ITER-specification tungsten was used (IG). This material has the same

purity, was produced also by Plansee AG but was hammered on both sides. Thus, in as-produced state it had elongated "carrot-like" grains.

Figure 37 demonstrates microstructural change of as-received IG tungsten after annealing at 1300°C, 1500°C and 1800°C during one hour in vacuum. As was revealed by TEM [59], such annealing leads to the decrease of the dislocation density from 4.5×10^{12} m^{-2} to 6×10^{11} m^{-2} after annealing at 1300°C, 3×10^{9} m^{-2} at 1500°C and 1×10^{8} m^{-2} at 1800°C. The latter value is the limit of the TEM resolution. The change in grain morphology was studied by EBSD. As it can be seen, it is expressed in the rounding of grains and enlargement of their size, which happened between 1300°C and 1500°C. Almost no difference is revealed between the material annealed at 1500°C and 1800°C, which means that the temperature of 1500°C is high enough to induce recrystallization of the initial microstructure on a time scale of an hour.

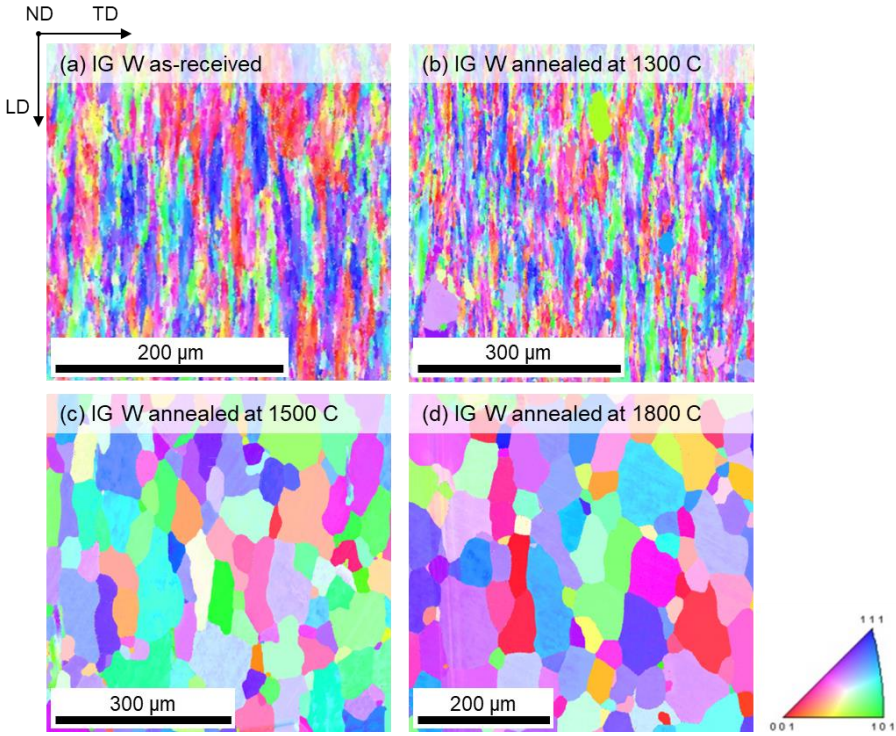

Figure 37 EBSD of (a) as-received IG tungsten and annealed at (b)1300°C, (c) 1500°C and (d) 1800°C

Figure 38 presents nanoindentation measurements of IG tungsten in as-received and annealed states. As one can see from Figure 38 (a), material softening with the increase of annealing temperature is evident. Samples

annealed at two higher temperatures (having the same grain size and assuming that all dislocations were annealed) demonstrate very similar result, which confirms the assumption, that all grains are already recrystallized after thermal treatment at 1500°C.

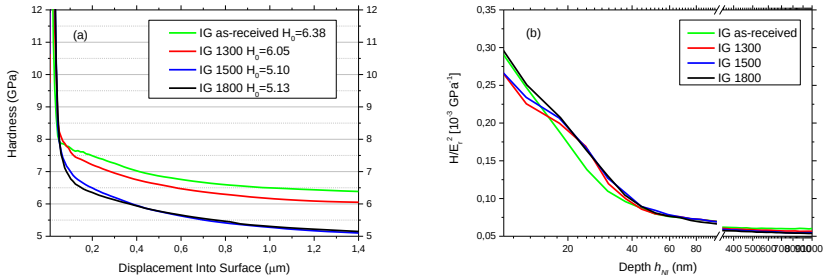

Figure 38 (a) H and (b) H/E_r^2 as functions of the indenter penetration depth, h, for IG W after annealing at 1300°C, 1500°C and 1800°C

Figure 38 (b) demonstrates that annealing practically did not change the H/E_r^2 function. This means that the resistance of the material to the penetration of GNDs was similar for all probed microstructures. The reason why the saturated hardness (i.e. hardness at large indentation depth) is quite sensitive to the annealing is probably because it is governed by the response of statistically stored dislocations and grain boundaries. Whereas H/E_r^2 value is governed by the dissolution of GNDs under the indenter tip and therefore the highest sensitivity occurs at shallow depths (where the contribution from GNDs is prevailing). Apparently, the dissolution of GNDs at the shallow penetration depths is not strongly modified by the reduction of the dislocation density from 4.5×10^{12} m^{-2} to 1×10^{8} m^{-2} and the increase of grain size.

The results of hardness as a function of probed depth are presented on Figure 39 (a) for the reference and plastically-deformed material. As was studied in [59] the applied plastic deformation led to the following change in the microstructure. A significant accumulation of dislocations and formation of dislocation pile-ups were observed after the deformation to 4%. The dislocation density increased to about 3×10^{13} m^{-2}. The investigation of microstructure and dislocation density of the 9% deformed sample did not reveal the difference with 4% deformed material. The effect of the plastic deformation is well pronounced on whole penetration depth, and it increases with the increase of the deformation strain (i.e. with the dislocation density). H/E_r^2 as a function of the indenter penetration depth is shown on Figure 39 (b). 4% and 9% deformed samples show similar results, while for the as-received material the curve becomes lower as the indentation depths is beyond 60 nm. This feature has a

good correlation with the increase of dislocation density and the refinement of sub-grains after plastic deformation as revealed by TEM. Thus, the representation of the results as H/E_r^2 *(h)* is sensitive to the grain refinement and the increase of dislocation density above 3×10^{13} m^{-2}, but not to the grain size increase.

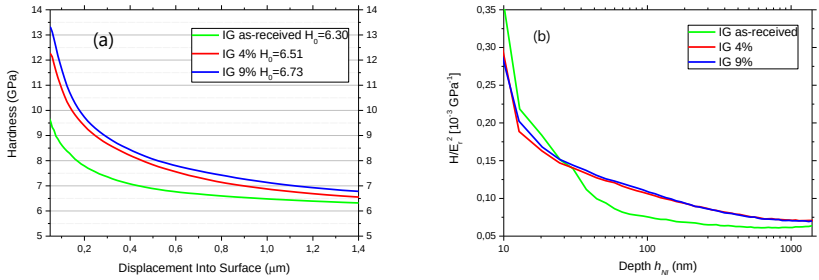

Figure 39 (a) H and (b) H/E_r^2 as functions of the indenter penetration depth, h, for IG W after deformation up to 4% and 9%

The data of H_0 is compared to the experimentally measured dislocation density on Figure 40. The figure also contains the curve obtained with the model proposed by Mecking and Kocks in [98]:

$$\dot{\rho}(\varepsilon) = \dot{\varepsilon}\left(k_1\sqrt{\rho} - k_2(\dot{\varepsilon},T)\rho(T)\right) \tag{12}$$

This model describes the evolution of the dislocation density ρ defined by the strain rate ε and the balance of dislocation multiplication and recovery/storage upon plastic deformation. These two opposite processes are effectively parameterized by introducing coefficients k_1 and k_2 which depend on temperature and strain rate:

$$\frac{k_2(\dot{\varepsilon},T)}{k_1} = \frac{\chi\cdot b}{g}\left(1 - \frac{k_B\cdot T}{D\cdot b^3}\cdot ln\left(\frac{\dot{\varepsilon}}{\dot{\varepsilon}_0}\right)\right) \tag{13}$$

Where χ is the interaction parameter, g – normalized activation energy, D – the constant of proportionality, $\dot{\varepsilon}_0$ and $\dot{\varepsilon}$ –reference and experimentally applied strain rate.

The model of Mecking and Kocks implies that the increase of the flow stress with progressive deformation applied to the material is driven by the multiplication of dislocations (so-called forest hardening). Subsequently, by doing nanoindentation on the plastically deformed materials we demonstrated that there is a correlation between the nanohardness and the dislocation density.

The multiplication of dislocations in bulk polycrystalline tungsten occurs as a result of self-pinning of dislocations and the formation of junction segments. Additionally, the formation of dislocation pile-ups and tangles near the microstructural defects which suppress dislocation propagation (e.g. grain boundary) is another reason for the multiplication of dislocations.

The removal of dislocations is attributed either to self-annihilation with dislocations of opposite signs, or to the absorption of dislocations by grain boundary interfaces. The latter represents a mechanism where the dislocation pile-ups formed in a front of a grain boundary results in either transmission of the piled dislocations into a neighboring grain, or in conversion of the bulk dislocations into grain boundary dislocations (i.e. absorption of dislocations). indeed, the saturated hardness at the depth of 1500 nm shows similar trend as dislocation density (see Figure 40). This was expected because the dislocation density is directly related to the increase of the flow stress, as was noted above.

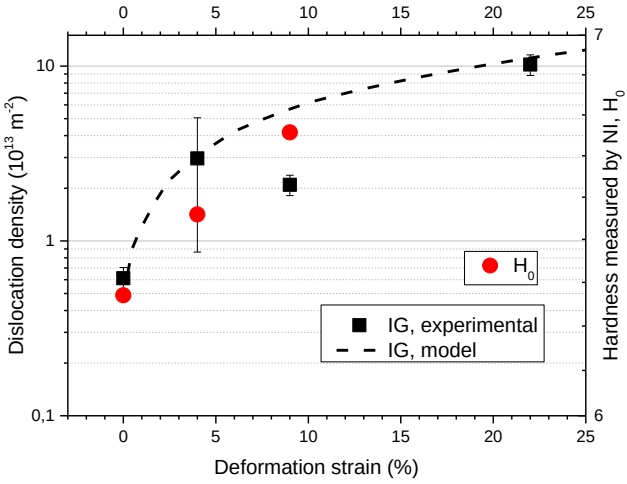

Figure 40 Dislocation density, comparison of the experimental measurements and model of Mecking and Kocks [98]

As a summary of this section, the following statements can be made. The value of H/E_r^2 *(h)* is not sensitive to the grain size increase (thus does not capture the process of recrystallization of tungsten), but is sensitive to the increase of the dislocation density. Accounting for the results obtained for the plasma-exposed samples, one can observe that H/E_r^2 resolve the presence of dislocations only if its absolute value exceeds a certain limit. Thus, this limit also depends on the absolute value of the indentation depth. This threshold can be understood from the fact that the material response is provided within a plastically affected zone,

which naturally increases as the indentation depths increases. The hardness is sensitive to the both decrease of the grain size (i.e. thermal annealing) and to the increase of the dislocation density (i.e. plastic deformation), however, the reliable measurements can only be obtained at significant penetration depth (i.e. region 2 and 3 on Figure 34).

3.3.1.3 Modification of surface hardness induced by mixed beam and He plasma

After the exposure to the mixed beam and pure He plasma, the samples were also tested by means of nanoindentation. The results of the measurements are presented on Figure 41 for the reference material. The results of the indentation of the exposed samples show very similar trend of hardness and H/E_r^2, while the material exposed to pure He plasma shows significant difference. In particular, in the shallow depth region there is a statistically significant reduction of the hardness, while H/E_r^2 strongly increases in the same indentation region.

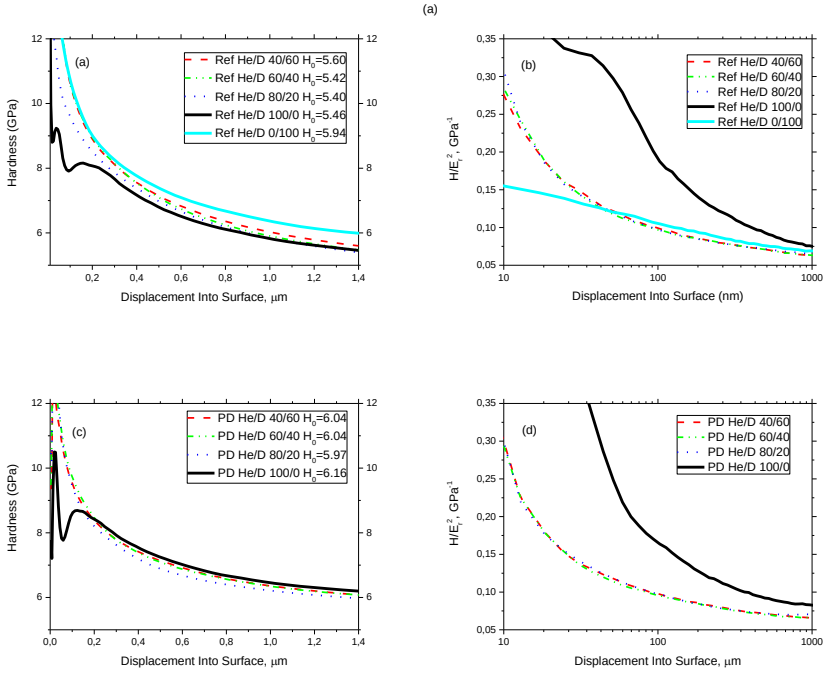

Figure 41 (a) H and (b) H/E_r^2 as functions of the indenter penetration depth, h, for DF reference W exposed to plasma of different composition. (c) H and (d) H/E_r^2 as functions of the indenter penetration depth, h, for DF plastically deformed W exposed to plasma of different composition

The fact that pure He exposure resulted in a reduced hardness within the first 0.2-0.3 μm can be explained by the formation of rough surface (precursor of fuzz) and a high density of bubbles observed by TEM (as will be reported in section 0). On the other hand, the increase of H/E_r^2 implying harder penetration of GNDs in the material could be explained by the presence of high dislocation density in the sub-surface region, which is also confirmed by TEM measurements. It can be seen that pre-applied plastic deformation does not change the conclusion on the impact of the mixed plasma exposure i.e. the significant difference is observed only in the case of pure He exposure. The results of the mixed beam exposures are very similar to those obtained after pure D exposure.

3.3.2 Surface blistering induced by plasma exposure

Blistering on the surface of tungsten after plasma exposure has been already studied in many works, e.g. [99-101]. In this section the main observations regarding blistering at relevant exposure conditions obtained in other works will be followed by the brief description of our observations.

Two types of blisters were revealed in the recrystallized tungsten after exposure to pure D plasma with flux of 10^{22} D/m^{-2}/s, fluence of 10^{26} D/m^{-2} and temperature T=480-520 K as reported in [99]: small ones (less than few microns in diameter) and large ones (greater than a few microns). Some of the large blisters reached the size of 20 μm and showed a multi-layered (stair-step) structure [99]. Most of them appeared near the grain boundaries.

Similar observations were reported in [100] for temperatures between 460 K and 515 K and fluence of 10^{27} D/m^{-2}. While lower temperature (320-370 K) exposures resulted in the formation of smaller blisters (reaching up to 10 μm in diameter), and no blisters were observed after exposures above 700 K, apparently due to the efficient diffusion towards the bulk.

Experiments reported in [101] revealed, that after exposure at 600-850 K, blisters even reached the size up to 100 μm, while lower temperature exposures caused the formation of only small blisters, comparable in size with other observations [99, 100].

It was also shown in works [99-101] that blister formation at the temperatures above 700-800 K was suppressed and blister size strongly depends on the exposure temperature. It is natural to assume that blister size and appearance should depend not only on the exposure temperature but also on the flux (with all other exposure parameters kept constant).

Our study was performed on the samples exposed to the fluences of F=8×10^{24}, 5×10^{25} and 3.5×10^{26} D/m^2 (which correspond to the exposure time of 10, 70 and 490 s) and at the temperature 473±10 K. Hydrogen retention in these specimens is described in the section 3.2. The surfaces of exposed samples are shown on Figure 42.

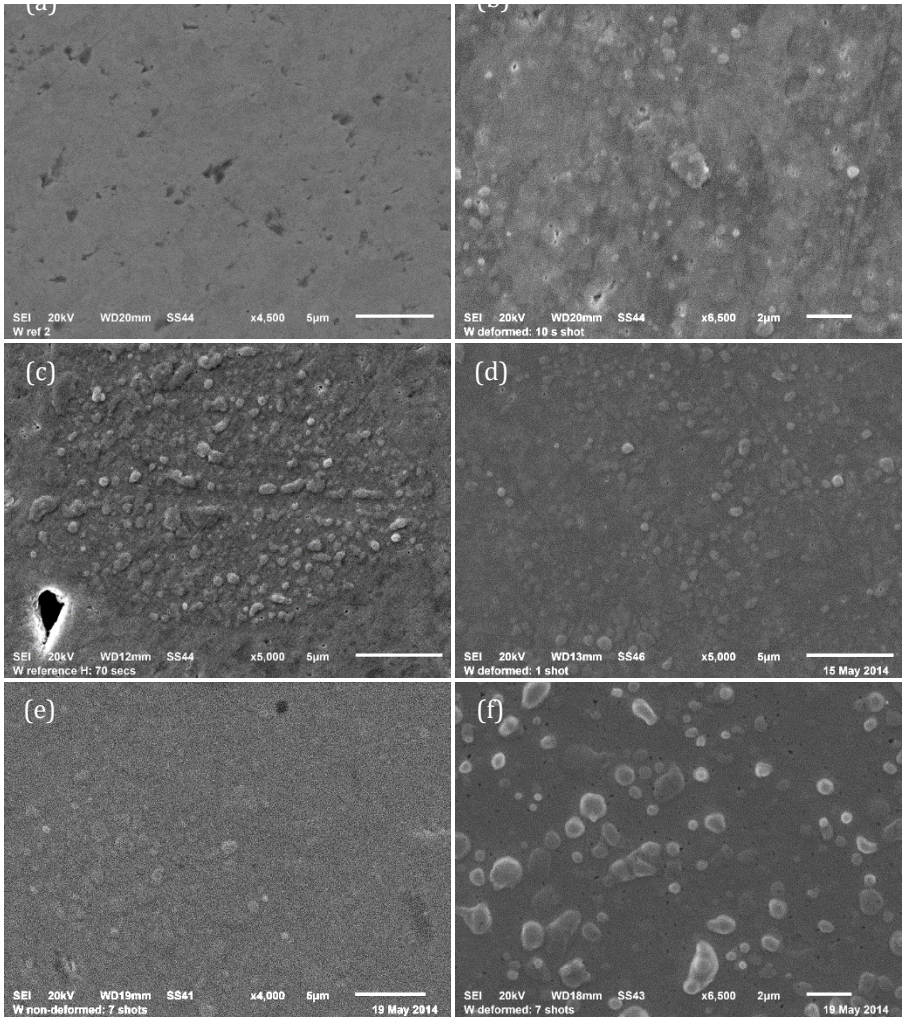

Figure 42 SEM images of W surface exposed to pure D plasma: (a) reference sample, fluence F=8×10^{24} D/m^2, (b) plastically deformed, fluence F=8×10^{24} D/m^2, (c) reference sample, fluence F=5×10^{25} D/m^2, (d) plastically deformed, fluence F=5×10^{25} D/m^2, (e) reference sample, fluence F=3.5×10^{26} D/m^2, (f) plastically deformed, fluence F=3.5×10^{26} D/m^2

Blisters were observed on the surfaces of all samples, except of the reference sample exposed to the lowest fluence (plasma discharge of 10 s). Blister size distribution was calculated in blister-rich zones and is summarized on Figure 43. The observations are in line with the previous study reported in [102].

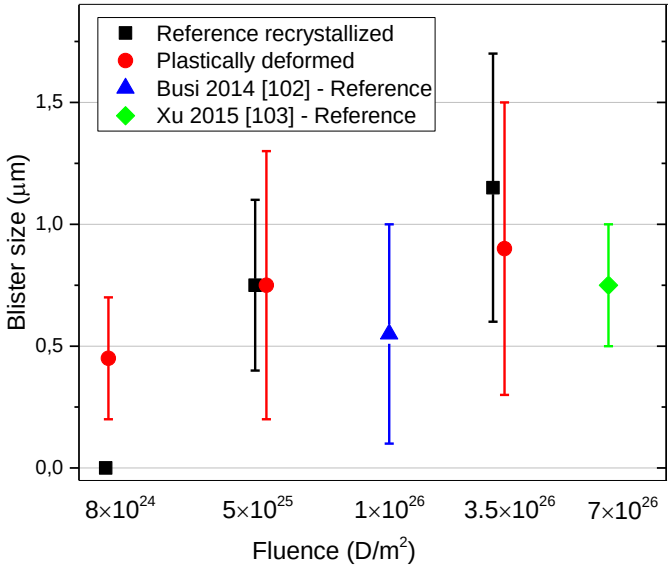

Figure 43 Blister size distribution compared to the data reported in [102] and [103]

Two types of regions were observed in reference material: blister-depleted and blister-rich (Figure 44 (a)). Blisters sometimes reached the size up to 2 μm and are spaced by about 0.5-3.0 μm. This heterogeneous blister distribution is in agreement with other studies of recrystallized tungsten (e.g. [96]).

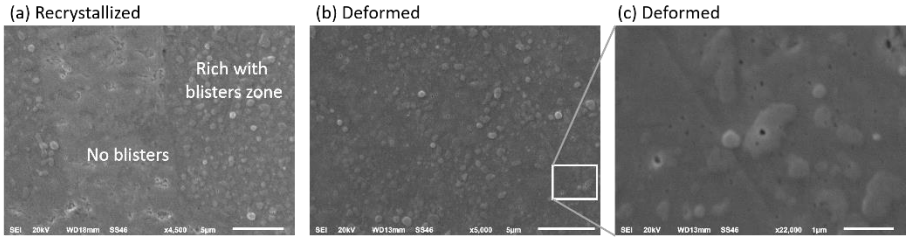

Figure 44 SEM images of plasma-exposed W samples: (a) Reference; (b) Deformed; (c) zoomed area showing ruptured blisters. The image is taken after TDS is done

Figure 44 (b) and (c) demonstrates the SEM images of the plastically deformed tungsten specimens after 70 s exposure. Significantly more uniform blister distribution was found in the plastically deformed sample, as well as the absence of blister-free zones. The size of blisters in plastically deformed material is smaller (up to 1 μm) compared to the reference sample and they are more numerous (spaced by 0.3-0.5 μm) i.e. their surface density is higher. Many of the blisters on the surface of the deformed sample were found to have small holes, an example of such feature is shown on Figure 44. SEM images were taken using a secondary electron detector, so these features can easily be identified as holes based on the pronounced contrast between the edge of the hole and the hole itself. Thus, the following conclusion can be made: most of blisters are open during plasma exposure probably due to the gas pressure exceeding the strength of the blister cap.

The presence of different blister density zones in the reference sample is attributed to the lattice orientation of the grains, (111)-oriented grains are assumed to be the most susceptible to blistering following the previous studies [104]. The blisters induced by high flux plasma are so called “high dome” blisters, which form by plastic deformation (hydrogen flakes, which are growing underneath the upper grains, push them upwards) and slip induced by gas pressure in the flake located underneath the blister [105]. Intensive blistering on (111)-oriented grains can be explained by preferential slip of the dislocations (with Burgers vector being $a_0/2<111>$). Nanoindentation measurements combined with EBSD analysis have been applied to the reference recrystallized material to verify that grain orientation indeed influences surface mechanical properties, which then could be linked to the different accumulation of plasma damage in grains with different orientations.

The reference sample was first scanned with EBSD and then, the area of interest was indented. The indenter marks are evident on Figure 45 (a), and the results of nanoindentation are grouped depending on grain orientation (6-8 indents per orientation) and shown on Figure 45 (b). The saturated hardness at a depth of 1.5 μm reaches 6±0.1 GPa, which is in good agreement with the values 6.0 GPa and 5.6 GPa reported in [106] and [107] for recrystallized polycrystalline tungsten respectively. This confirms that plasma induced damage does not spread deeper than 1.5-2.0 μm.

At the depth below 400-500 nm, the hardness measured in the (111) grain is clearly lower than in the two others. This effect could be related to the variation in the storage of plasma damage, as also expressed by heterogeneous distribution of blisters, see examples on Figure 45 (c) and (d).

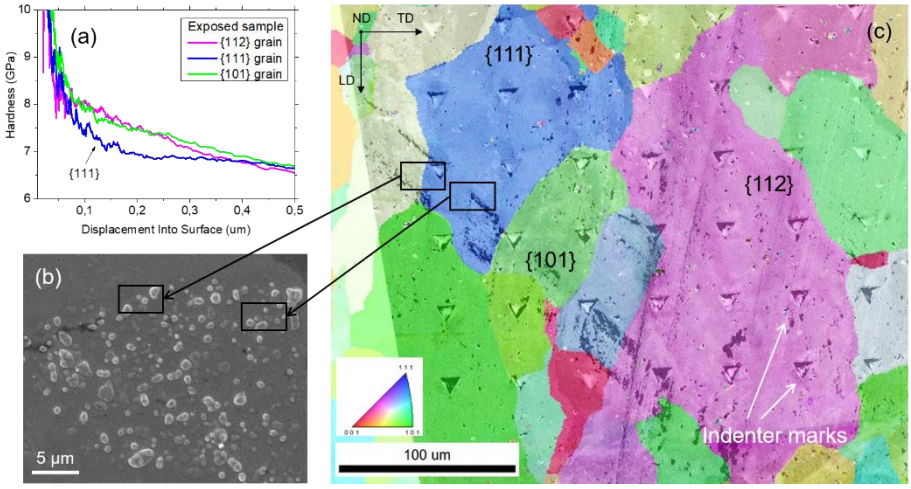

Figure 45 (a) Hardness depth profile measured by nanoindentation in the exposed reference sample; (b) SEM micrograph showing the blister-rich and blister-free zones in reference sample; (c) Electron backscatter diffraction inverse pole figure map of reference sample exposed to plasma combined with the map of indents. Exposure fluence – 5×10^{25} m^{-2}

Thus, it can be concluded that the pre-deformed material exhibits much more uniform pattern of blisters, whereas the reference material reveals strong dependence on the grain orientation, at least in the case of the probed plasma exposure conditions. Nano-indentation applied to the reference sample confirmed systematic difference in the hardness of <111>-oriented grains compared to others.

3.3.3 TEM investigation of the effect of plasma exposure on microstructure

The results of TEM investigation are presented in this subsection. TEM was used to study the impact of plasma exposure on the reference and plastically deformed samples which were irradiated in similar conditions (i.e. equivalent plasma flux, fluence and similar temperature). To understand better the impact on the microstructure, the study was performed at different depths. The samples exposed to pure He and mixed He-D plasmas were also investigated to reveal whether addition of He leads to the variation of the microstructural evolution as compared to pure D or pure He exposure. It turned out that TEM sample for the top surface investigation could not be prepared due to the high porosity and roughness. The slice of the material extracted by FIB was studied in SEM to demonstrate the extension of the plasma impact on the grain morphology.

3.3.3.1 Microstructure before exposures

TEM was applied to investigate the effect of plasma exposure on microstructure and microstructural modification depending on the depth from the exposed surface. The study was performed on the top surface of the material and in the bulk, where plasma induced modification was not expected. The TEM samples were prepared in accordance with the procedure described in section 2.3.

Figure 46 demonstrates the composite image of reference recrystallized tungsten. The presence of sub-grains with a mean size of 2.5-5.0 μm and mainly connected by low-angle grain boundary interfaces was observed. The average dislocation density was estimated to be around 2.8×10^{12} m^{-2} [59].

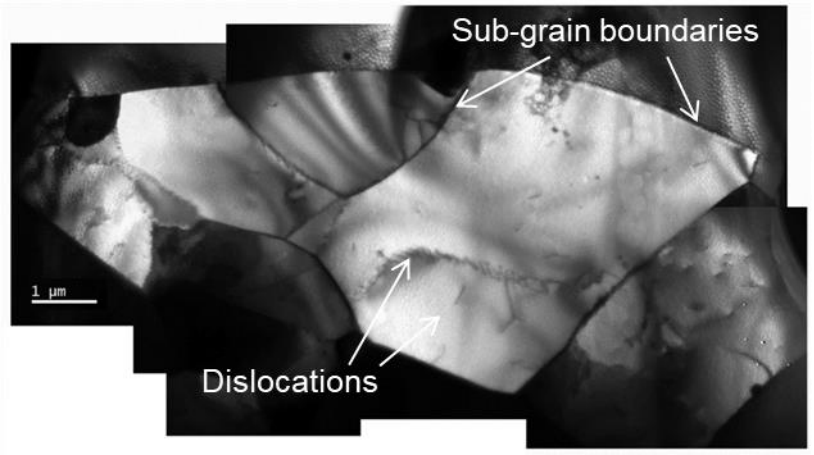

Figure 46 Composite TEM image of DF grade

Modification of microstructure with an increase of deformation level is shown on Figure 47. In 5% deformed samples, similar to the reference recrystallized material, only screw dislocation segments with Burgers vector $a_0/2<111>$ were observed. With the increase of deformation level up to 20% and 28%, a densely tangled dislocation network with a significant presence of edge component was revealed. Moreover, after 28% deformation a process of grain refinement had started.

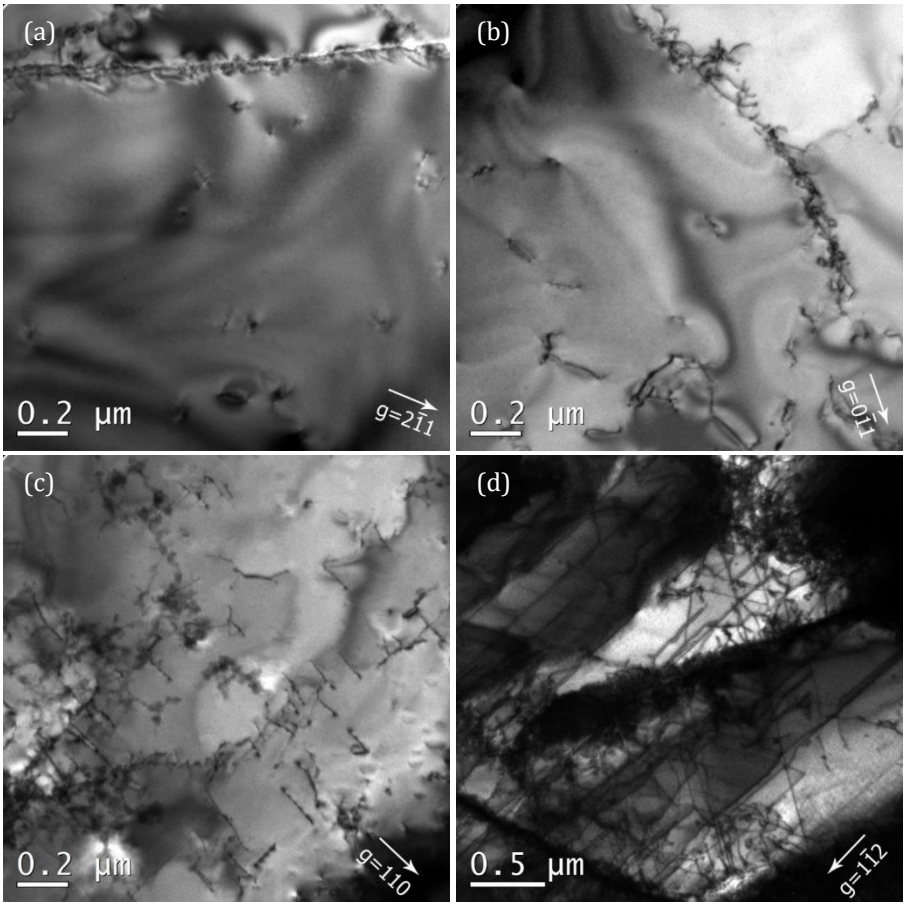

Figure 47 TEM micrographs showing a typical dislocation pattern in tungsten corresponding to (a) as-annealed condition, g=(2$\bar{1}$1) (211)and close to a [113] zone axis; (b) 5% deformed, g=(0$\bar{1}$1) and close to a [011] zone axis; (c) 20% deformed, g=(110) and close to a [001] zone axis; (d) 28% deformed, g=(1$\bar{1}$2) and close to a [111] zone axis

The comparison of measured dislocation density with the model of Mecking and Kocks [98] is presented on Figure 48. The experimental TEM results were demonstrated to be in good agreement with the theoretical data [59].

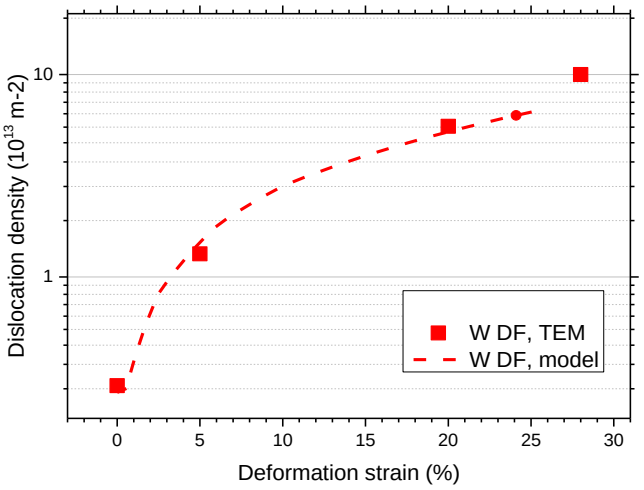

Figure 48 Dislocation density, comparison of the experimental measurements and model of Mecking and Kocks [98]

3.3.3.2 Microstructure after exposure to D plasma

TEM study after D plasma exposure (F=5×10^{25} D/m^2, T=570 K) revealed the following: significant increase of dislocation density and presence of dense dislocation networks in the surface layer (Figure 49 (a) and (b)). Dislocation density was found to be more than a factor of two higher in comparison with the value in the bulk and not uniform in different sub-grains. An example of the two neighboring sub-grains is demonstrated on Figure 49 (c) and (d).

Exposures of plastically deformed material (F=5×10^{25} D/m^2, T=620 K, 20% deformation) also resulted in significant increase of dislocation density in the sub-surface region (Figure 50) as well as presence of dislocation networks.

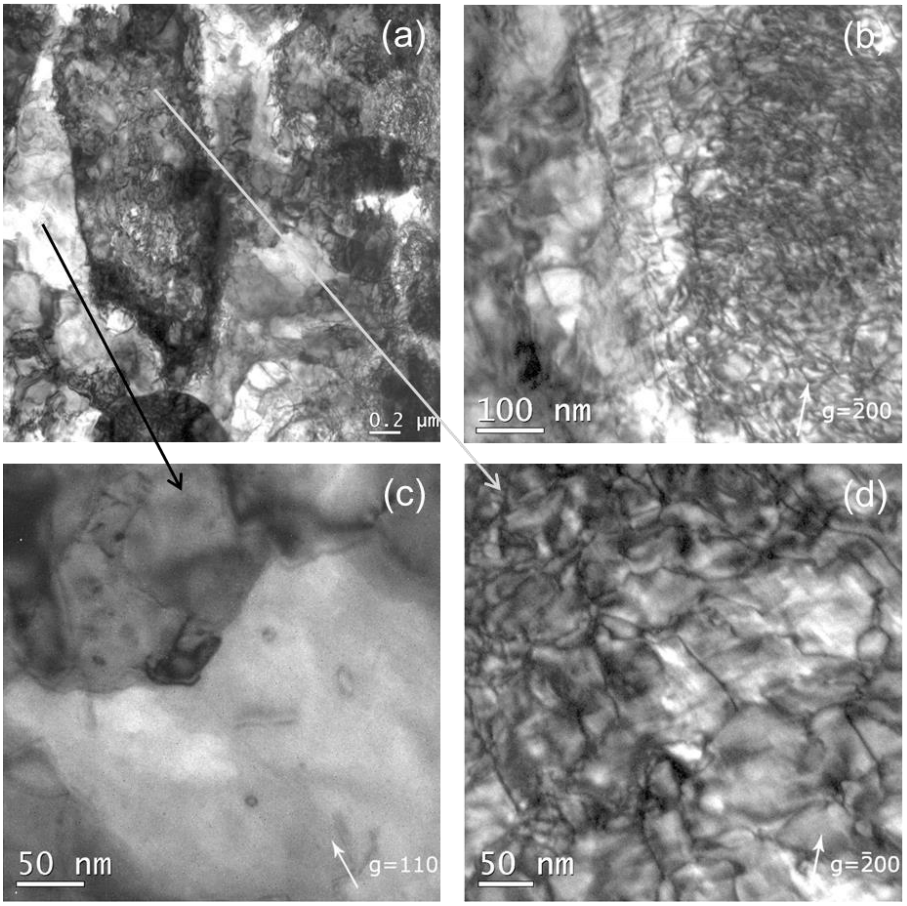

Figure 49 TEM micrographs of reference recrystallized tungsten after plasma exposure: (a) top surface; (b) higher magnification of the top surface to demonstrate the presence of dislocation tangles; (c) and (d) higher magnification of two neighboring sub-grains with a strong difference in dislocation density, namely (c) 4×10^{13} m^{-2} and (d) 1.5×10^{14} m^{-2}

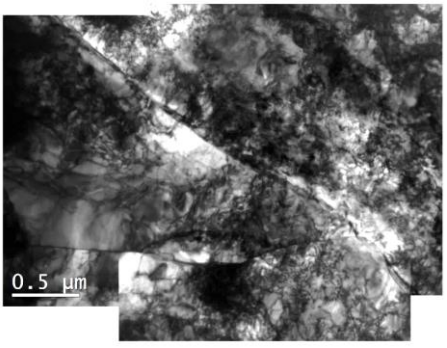

Figure 50 Composite TEM image of the surface microstructure of the plasma exposed DF 20% deformed sample

The dislocation density for both exposed samples was also calculated at different depths and the results are presented on Figure 51. It can be seen that the dislocation density of not deformed material recovers to the value measured before exposure at a depth of 10-12 μm. The measurements done in deformed sample show that dislocation density decreases linearly with depth, reaching the reference value at a depth of about 12-13 μm.

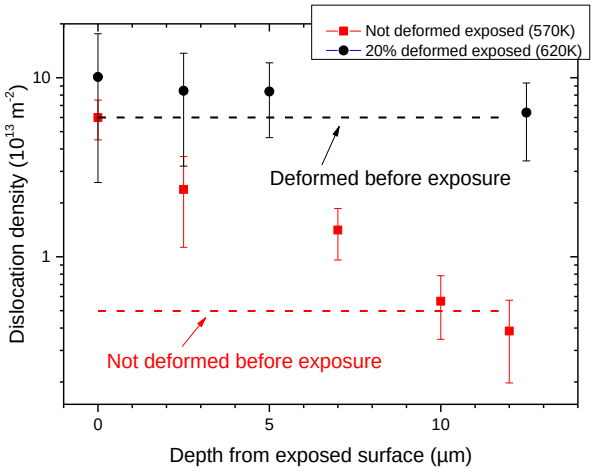

Figure 51 Average dislocation density measured in reference recrystallized tungsten after plasma exposure at 570 K as a function of the distance from the exposed surface

Thereby, the main impact of D plasma exposure on the microstructure is the strong increase of the dislocation density (by about one order of magnitude) on the surface, moderate increase within 1-5 μm range and recovery of the initial microstructure beyond 10 μm.

3.3.3.3 Microstructure after mixed beam and pure He plasma exposure

Tungsten samples exposed to a mixed He-D plasma varying He-to-D ratio from 40% He and 60% D to 80% He and 20% D were studied by TEM to reveal the effect of mixed plasma beam on the microstructure. The microstructure of the exposed samples was studied at the top surface (first 100 nm from the surface) and in a sub-surface region located at a depth of 1-5 μm.

The defect structure of the exposed area of reference samples exposed to the three different plasmas is shown on Figure 52. The inspection of the top surface layer revealed the presence of cavities of circular shape and the strong

increase of dislocation density in all inspected specimens. In some regions it exceeded 10^{15} m^{-2}. Nevertheless, no regular observation of the dislocation loops (expected due to the loop-punch mechanism [108]) was registered, as it was reported in [109] and [110]. This can be attributed to the energy of the He ions (50 eV) which is too low to produce displacement damage leading to the formation of loops, and to low dislocation density which can screen the escape of the loops to the surface [72, 111]. Hence, the lack of the observation of loops could be due to the dynamic recovery of the loops (escape to the top surface) during the exposure.

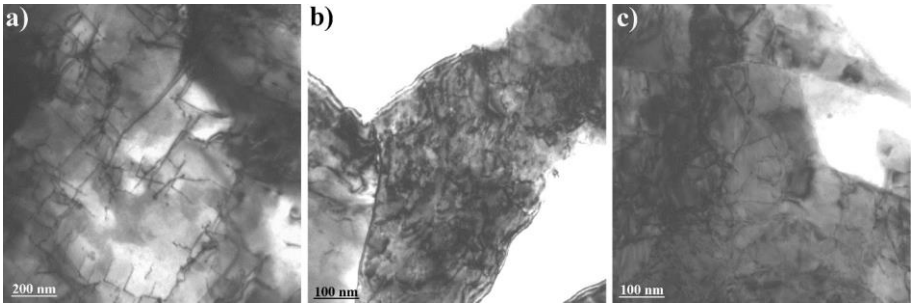

Figure 52 TEM images of the dislocation patterns at the exposed surface of the non-deformed samples exposed to a) the He/D = 80/20 plasma, b) the He/D = 60/40 plasma and c) the He/D = 40/60 plasma

Figure 53 shows typical TEM images of the top surface region. Strong reduction of dislocation density in the sub-surface region (first 5 μm from the exposed surface) was revealed in both reference and the plastically deformed samples, which nearly recovers to the microstructure before exposures. At this depth, the cavities, resolved by TEM, were no longer observed. Hence, if the cavities or He-D clusters actually present in the material their size should not exceed one nanometer (being the resolution limit of applied TEM).

Different He-to-D ratio during plasma exposures did not result in a detectable difference in the defect structure at the exposed surface. This conclusion is in line with TDS measurements reported in section 0, demonstrating that the release peak responsible for detrapping from dislocations has the main contribution to the trapping of plasma particles.

Due to the strong roughness of plasma subjected surface in case of pure He plasma exposure, it was found that single-side polishing does not provide the acceptable quality to perform TEM analysis, and only the sub-surface region (1-5 μm) could be studied.

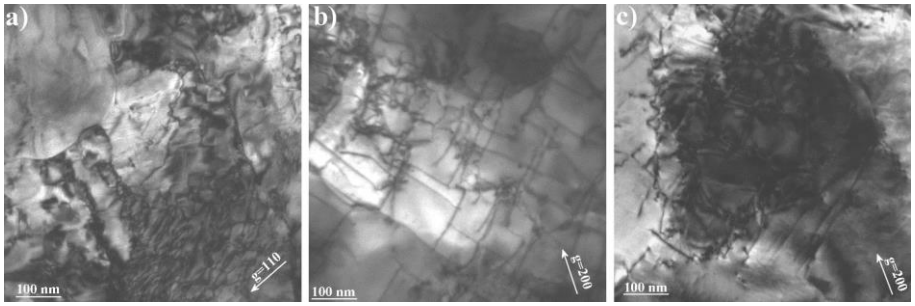

Figure 53 TEM images of the dislocation structure near the exposed surface of the plastically deformed tungsten samples exposed to a) the He/D = 80/20 plasma, b) the He/D = 60/40 plasma and c) the He/D = 40/60 plasma

Increase of dislocation density after D plasma exposure was found to be about one order of magnitude compared to not-exposed sample. In the He-exposed sample, the increase of the dislocation density was much higher, and in the shown region on Figure 54 it reached a value of (1-2)×10^{15} m^{-2}.

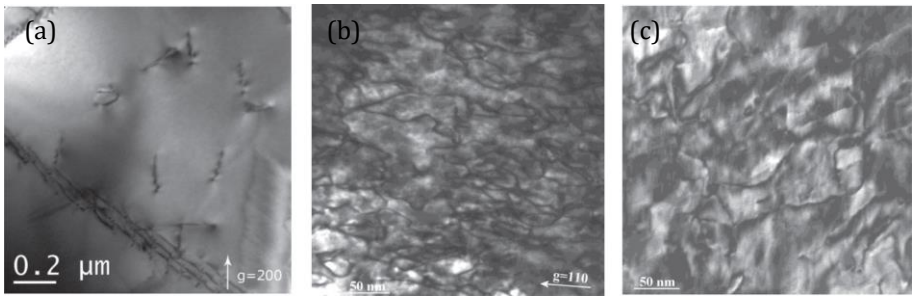

Figure 54 TEM images of not deformed samples exposed to (a) D and (b) He, and (c) plastically deformed sample exposed to pure He plasma. The dislocation density at a depth of 3-5 μm below the plasma exposed surface is measured to be about (2-4)×10^{13} m^{-2} in D-exposed sample, and (1-2))×10^{15} m^{-2} in the He-exposed sample (for both reference recrystallized and plastically deformed samples)

Since TEM investigation of the top surface area is impossible due to the surface roughness, the investigation of He plasma induced damage was performed using FIB. The SEM image of the lamella cut with FIB is shown on Figure 55. Although the surface quality still requires improvement, grain refinement in the sub-surface region at the depth of 1 μm or even less is evident. This confirms that the top surface region is heavily deformed (pattern of small sub-grains) while the region within next 10 μm is nearly free of the grain refinement. So, He exposure affects material microstructure more strongly than D exposure, at least within the range of 5 μm from the surface. Clearly, a much

more careful investigation is needed to understand the nanometer level microstructure in the surface and subsurface region after pure He exposures.

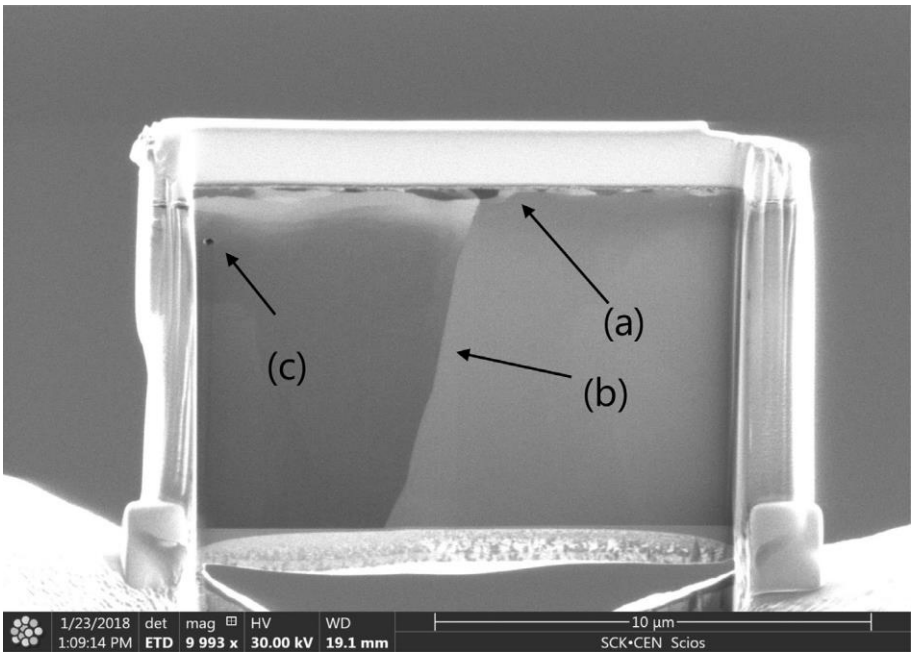

Figure 55 FIB-cut TEM lamella extracted from the He-exposed REF sample, the image is recorded using the ion beam and it shows (a) plasma-exposed top surface where the grain refinement occurred; (b) grain boundary interface which goes along the whole sample; (c) cavity induced by the plasma exposure

A comparison of dislocation density measured by TEM at different depth from beneath the exposed surface for He, D and mixed beam plasma exposures is shown on Figure 56. It is evident from the Figure 56 that the microstructure of material after mixed beam exposures recovers to the initial one much faster than after pure D plasma exposure (5 µm vs. 10-12 µm). The fact that the value of dislocation density after pure He is much higher than the ones after mixed beam, is in good agreement with the observed difference of the material resistance to the penetration of GNDs (H/E_r^2) shown on Figure 41. Further detailed TEM analysis is needed to reveal the trend of dislocation density after pure He exposures.

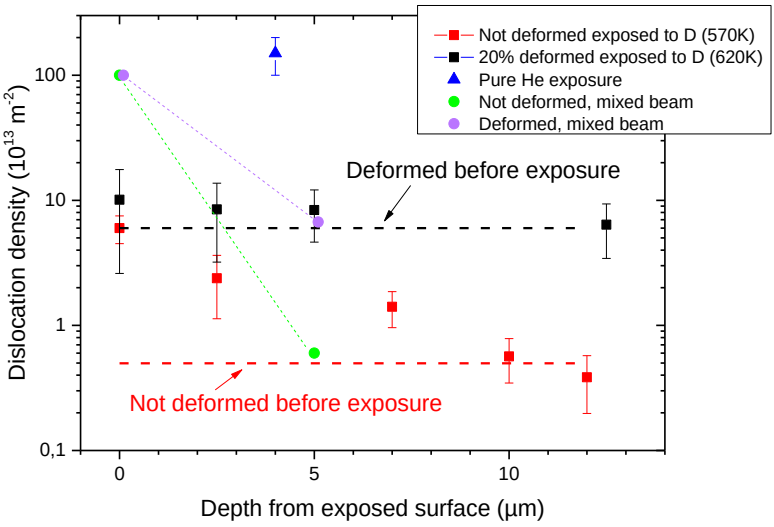

Figure 56 Average dislocation density measured after pure D and mixed beam plasma exposures as a function of the distance from the exposed surface

4

Conclusions and outlook

4.1. Summary and conclusions

Experimental work was performed to assess the interaction of high flux plasma with tungsten in different microstructural state using a number of techniques such as uniaxial tensile loading, TDS, NRA, as well as microstructural analysis tools – SEM, TEM, EBSD and FIB. The main experimental findings of the presented thesis and conclusions can be summarized in the same structure as the Thesis Tasks were formulated:

1. *Impact of plastic deformation and exposure fluence on D retention and surface microstructure, studied at baseline exposure temperature (470 K)*

    - Plastic deformation led to the complex interplay in the intensity of three main deuterium release peaks. Namely plastic deformation resulted in the enlargement of contribution of the release stages responsible for detrapping from dislocations and vacancies. At the same time the contribution of pores was totally restrained up to an exposure fluence of 5×10^{25} D/m^2; hence the dislocation network suppressed the bubble growth rate. Beyond the certain dose, the peak responsible for the detrapping from pores increased substantially exceeding the value in the reference material.

    - The total deuterium retention (progressively increasing with the fluence) increased by about 50% after plastic deformation in comparison with reference recrystallized samples (in the range of studied fluences of 8×10^{24}, 5×10^{25} and 3.5×10^{26} D/m^2).

- Dedicated deuterium plasma exposures of plastically deformed tungsten samples resulted in the rupture of almost all visible blisters on the surface of deformed samples, unlike the surface of recrystallized tungsten. In the deformed samples, the gas release spectrum did not have a stage which corresponds to the release from the bubbles, while this stage was present in the reference recrystallized material.

- Nanoindentation performed on the recrystallized sample revealed different hardness between the (111)-oriented and other high-index oriented grains. This observation is consistent with the heterogeneous distribution of blisters, which mostly are present on the (111) oriented grains, as identified by SEM. Hence, it was concluded that nanoindentation technique is sensitive enough to resolve changes in the hardness of very thin region affected by the plasma exposure. Such methodology might have a potential for non-destructive analysis of PFC.

- Nanoindentation results demonstrated that plasma exposure increased significantly the resistance to plastic penetration of the indenter in the sub-surface region affected by the exposure. The increase is concluded to be from the presence of nanometric cavities, which act as obstacles to the movement of GNDs propagating away from the indenter tip.

2. *Impact of plastic deformation and exposure temperature on D retention, studied at fixed fluence (10^{26} D/m^2)*

    - Plastic deformation affected both the total deuterium retention and its distribution in different types of traps. It was expressed in higher dislocation density in plastically deformed samples (2×10^{14} m^{-2}) compared to reference recrystallized material (4×10^{12} m^{-2}). During the exposures at low temperatures (460 and 600 K) plastic deformation enhanced the total retention but suppressed the growth of cavities; meanwhile at high temperatures (820 and 1000 K) it reduced the total retention. The explanation for this observation can be the following: the retention at low temperatures is mainly driven by trapping and nucleation of bubbles at bulk dislocations and dislocation junctions, whereas at high temperatures it is mainly facilitated by the long-range diffusion into the bulk.

    - The transition between these two regimes occurred in the range of 600-700 K. It can be suggested, assuming that deuterium trapping and nucleation of plasma induced defects are driven by the

dislocation networks, that the temperature of 600-700 K is the upper limit for the dislocation-dominating trapping in the ITER-relevant high flux regime. This temperature threshold provides an estimate for the operation temperature where the deep diffusion towards PFC can still be suppressed thanks to the natural microstructure of ITER-specification tungsten grades.

3. *Impact of plastic deformation and plasma composition, studied at baseline exposure conditions (T=470 K, fluence 5×10^{26} - 1×10^{27} D/m^2)*

- Three major release stages were observed in both reference recrystallized and plastically deformed samples after pure He plasma exposure. The peaks positions are the same for both types of samples, but their amplitudes differ and depend on the dislocation density of the material. Hence, within the studied exposure conditions, plastic deformation does not change the fundamental mechanisms by which He trapping, diffusion and release occur.

- Plastic deformation suppressed the total He retention by a factor of three, taking into account that TDS measurement was performed up to 1300 K, i.e. certain amount of He may remain in the samples. Definite conclusions requires high temperature TDS measurements.

- Pure He plasma exposure induced much stronger increase of dislocation density in the sub-surface region of reference recrystallized samples as compared to pure D exposure. However, the depth where the microstructure recovers to the original bulk pattern was about 15-20 μm and is similar for both pure He and pure D exposed samples.

- The integral retention of He faintly depends on the He-to-D ratio, but it increased significantly as the fraction of He raises from 80% to 100%. It can be concluded that the presence of even 20% of D in the beam substantially suppresses He trapping.

- He seeding into the plasma enhanced the integral retention of D in both reference recrystallized and plastically deformed samples. Thus, D retention in the mixed beam is primary defined by amount of He. Apparently, He atoms promote nucleation of stable nanobubbles, which accommodate both He and D atoms under high flux exposure.

- Since D trapping increased with the reduction of D seeding into the plasma (and coincident growth of He seeding), not dislocation-

induced microstructure, but the He seeding played the major role in the D trapping under mixed beam exposure.

- In the TDS cycle after mixed beam exposures, He release started earlier than the release of D. This can be explained by the presence of mixed He-D nanoclusters, in which the (de)trapping energy of He to the cluster is lower compared to the trapping energy of D. The difference in the detrapping energy can be attributed to the difference in the migration energy of He and hydrogen in tungsten bulk, which according to the *ab initio* data [36, 112], amounts to 0.2 eV.

4.2. Outlook

As an outlook for further study and to confirm some of the preliminary conclusions drawn from this work, one should clarify several points which might have further consequences with respect to the subject studied here, namely:

- To perform high temperature (at least up to 2000 K) TDS measurements to confirm the conclusions regarding the outgassing of He. Earlier studies [113, 114] demonstrate that He release may last up to 1600-1800 K, meanwhile the TDS setup used in this work can only ensure heating up to 1300 K

- To perform local measurements of thermal conductivity of the pure D and D-He exposed samples to clarify whether pre-applied plastic deformation has an impact on the thermal conductivity of 10-50 μm layer of the plasma exposed samples

- To perform follow-up plasma discharge exposures (using D and D-He exposed samples) to simulate transients. The currently obtained samples perfectly fit quasi steady-state plasma accelerator (QSPA) Kh-50 available for EU Fusion consortium. This will allow to understand the impact of pre-existing D and D-He exposure on the crack formation boundary.

References

1. M. Kikuchi, K. Lackner, M. Q. Tran, *The case for fusion*, in *Fusion physics*. 2012, International Atomic Energy Agency: Vienna. p. 1-58.
2. Ongena, J. and Y. Ogawa, *Nuclear fusion: Status report and future prospects.* Energy Policy, 2016. **96**: p. 770-778.
3. Kikuchi, M., *Hydrogen Fusion: Light Nuclei and Theory of Fusion Reactions* in *Frontiers in Fusion Research* 2011. p. 15-32.
4. Viswanathan, B., *Nuclear Fusion*, in *Energy Sources* 2017. p. 127-137.
5. Xu, Y., *A general comparison between tokamak and stellarator plasmas.* Matter and Radiation at Extremes, 2016. **1**: p. 192-200.
6. K.J. Dietz, D. Bartlett, G. Baumel, et al, *Start up and initial operation of JET.* Journal of Nuclear Materials 1984. **128 & 129**: p. 10-18.
7. Callis, R., *Start-Up performance of the DIII- D tokamak.* Fusion technology, 1986. **1**: p. 347-352.
8. B. Lipschultz, J. Goetz, B. LaBombard, G. McCracken, J. Terry, D. Jablonski, C. Kurz, A. Niemczewski, J. Snipes, *Plasma-surface interactions in the Alcator C-Mod tokamak.* Journal of Nuclear Materials, 1995. **220-222**: p. 967-970.
9. W. Tenten, U. Dohms, L. Fuss, H. Huppertz, J. Lerch, K.D. Miiller, P. Reinhart, F. Rongen, *How to upgrade a control system for a tokamak.* Nuclear Instruments and Methods in Physics Research, 1994. **A352**: p. 137-140.
10. C.-P. Käsemann, E. Grois, F. Stobbe, M. Rott, and K. Klaster, *Pulsed Power Supply System of the ASDEX Upgrade Tokamak Research Facility.* 15th International Conference on Environment and Electrical Engineering (EEEIC), 2015 p. 237-242.
11. Bucalossi, J., *Tore Supra—WEST*, in *Magnetic Fusion Energy* 2016. p. 261-293.
12. V.K. Gusev, T.A. Burtseva, A.V. Dech, G.A. Gavrilov, V.E. Golant, S.V. Krikunov, R.G. Levin, V.B. Minaev, A.B. Mineev, O.A. Minyaev, *Plasma Formation and First OH Experiments in the Globus-M Tokamak.* Nuclear Fusion, 2001. **41**: p. 919.
13. X. Gao, the EAST team, *Diagnostics for first plasma study on EAST tokamak.* Physics Letters A, 2008. **372** p. 2286–2290.
14. V.P. Muratov, G.L. Saksagansky, O.G. Filatov, *ITER – International Thermonuclear Experimental Reactor*, in *Fundamentals of Magnetic Thermonuclear Reactor Design* 2018. p. 39-67.
15. Y. Wu, S. Sahin, *Fusion Energy Production*, in *Comprehensive Energy Systems* 2018. p. 538-589.
16. Romanelli, F., *EFDA - Fusion Electricity. A roadmap to the realisation of fusion energy*. 2012. p. 1-75.
17. *ITER (International Thermonuclear Experimental Reactor)*. Available from: https://www.iter.org/.
18. T. Hirai, S. Panayotis, V. Barabash, C. Amzallag, F. Escourbiac, A. Durocher, M. Merola, J. Linke, Th. Loewenhoff, G. Pintsuk, M. Wirtz, I.

Uytdenhouwen, *Use of tungsten material for the ITER divertor.* Nuclear Materials and Energy, 2016. **9**: p. 616-622.

19. R. Parker, G. Janeschitz, H.D. Pacher, D. Post, S. Chiocchio, G. Federici, P. Ladd, ITER Joint Central Team, Home Teams, *Plasma-wall interactions in ITER.* Journal of Nuclear Materials, 1997. **241-243**: p. 1-26.
20. M. Merola, F. Escourbiac, A. R. Raffray, P. Chappuis, T. Hirai, S. Gicquel, *Engineering challenges and development of the ITER Blanket Systemand Divertor.* Fusion Engineering and Design, 2015. **96-97**: p. 34-41.
21. S. Carpentier-Chouchana, T. Hirai, F. Escourbiac, a. Durocher, a. Fedosov, L. Ferrand, M. Firdaouss, M. Kocan, a. S. Kukushkin, T. Jokinen, V. Komarov, M. Lehnen, M. Merola, R. Mitteau, R. A. Pitts, P. C. Stangeby, M. Sugihara, *Status of the ITER full-tungsten divertor shaping and heat load distribution analysis.* Physica Scripta, 2014. **T159**: p. 014002.
22. R. A. Pitts, S. Carpentier, F. Escourbiac, T. Hirai, V. Komarov, S. Lisgo, A. S. Kukushkin, A. Loarte, M. Merola, A. Sashala Naik, R. Mitteau, M. Sugihara, B. Bazylev, P. C. Stangeby, *A full tungsten divertor for ITER: Physics issues and design status.* Journal of Nuclear Materials, 2013. **438(SUPPL)**: p. S48–S56.
23. T. Hirai, F. Escourbiac, S. Carpentier-Chouchana, A. Fedosov, L. Ferrand, T. Jokinen, V. Komarov, A. Kukushkin, M. Merola, R. Mitteau, R.A. Pitts, W. Shu, M. Sugihara ,B. Riccardi, S. Suzuki, R. Villari, *ITER tungsten divertor design development and qualification program.* Fusion Engineering and Design, 2013. **88**: p. 1798-1801.
24. Gustafson, P., *Evaluation of the Thermodynamic Properties of Tungsten.* International Journal of Thermophysics, 1985. **6**(4): p. 395-409.
25. Pintsuk, G., *Tungsten as plasma facing material.* Comprehensive Nuclear Materials, 2012. **4**: p. 551-581.
26. I. V. Mazul, G. L. Saksagansky, *First Wall Components*, in *Fundamentals of Magnetic Thermonuclear Reactor Design* 2018. p. 211-246.
27. Sikka, V.K. and J. Moteff, *Superlattice of voids in neutron-irradiated tungsten* Journal of Applied Physics 1972. **43**(12): p. 4942–4944.
28. I. V. Gorynin, V .A. Ignatov, V. V. Rybin, et al., *Effects of neutron irradiation on properties of refractory metals.* Journal of Nuclear Materials 1992. **191–194**: p. 421–425.
29. L.K. Keys, J. Moteff, *Neutron irradiation and defect recovery of tungsten.* Journal of Nuclear Materials, 1970. **34**(3): p. 260-280.
30. D. Stork, P. Agostini, J-L. Boutard, D. Buckthorpe, E. Diegele, S. L. Dudarev, C. English, G. Federici, M. R. Gilbert, S. Gonzalez, A. Ibarra, Ch. Linsmeier, A. Li Puma, G. Marbach, P. F. Morris, L. W. Packer, B. Raj, M. Rieth, M. Q. Tran, D. J. Ward, S. J. Zinkle, *Developing Structural, High-heat flux and Plasma Facing Materials for a near-term DEMO Fusion Power Plant: the EU Assessment.* Journal of Nuclear Materials, 2014. **455**(1-3): p. 277-291.
31. Roth, J., et al., *Tritium inventory in ITER plasma-facing materials and tritium removal procedures.* Plasma Physics and Controlled Fusion, 2008. **50**: p. 103001.

32. D.F. Johnson, E.A. Carter, *Hydrogen in tungsten: Absorption, diffusion, vacancy trapping, and decohesion.* Journal of Materials Research, 2010. **25**(2): p. 315-327.
33. Tanabe, T., *Review of hydrogen retention in tungsten.* Physica Scripta, 2014. **T159** p. 014044.
34. Tanabe, T., *Review of hydrogen retention in tungsten.* Physica Scripta, 2014. **T159**.
35. Dubinko, V., et al., *Dislocation mechanism of deuterium retention in tungsten under plasma implantation.* Journal of Physics: Condensed Matter, 2014. **26**: p. 395001.
36. Heinola, K., et al., *Hydrogen interaction with point defects in tungsten.* Physical Review B, 2010. **82**(9): p. 094102.
37. Terentyev, D., et al., *Dislocations mediate hydrogen retention in tungsten.* Nuclear Fusion, 2014. **54**: p. 042004.
38. Sand, A.E., K. Nordlund, and S.L. Dudarev, *Radiation damage production in massive cascades initiated by fusion neutrons in tungsten.* Journal of Nuclear Materials, 2014. **455**(1-3): p. 207-211.
39. Van Renterghem, W., et al., *TEM analysis of recrystallized double forged tungsten after exposure in JUDITH 1 and JUDITH 2.* Nuclear Materials and Energy, 2016. **9**: p. 484-489.
40. Alimov, V.K. and J. Roth, *Hydrogen isotope retention in plasma-facing materials: review of recent experimental results.* Physica Scripta, 2007. **T128**: p. 6-13.
41. Henriksson, K.O.E., et al., *The depth of hydrogen and hellium bubbles in tungsten: a compasiron.* Fusion Science and Technology, 2006. **50**: p. 43-57.
42. Alimov, V.K., et al., *The effect of displacement damage on deuterium retention in ITER-grade tungsten exposed to low-energy, high-flux pure and helium-seeded deuterium plasmas.* Journal of Nuclear Materials, 2012. **420**(1-3): p. 370-373.
43. Ogorodnikova, O.V., et al., *Deuterium retention in tungsten exposed to low-energy pure and helium-seeded deuterium plasmas.* Journal of Applied Physics, 2011. **109**(1): p. 013309.
44. Alimov, V.K., et al., *Surface morphology and deuterium retention in tungsten exposed to low-energy, high flux pure and helium-seeded deuterium plasmas.* Physica Scripta, 2009. **T138**.
45. Finlay, T.J., et al., *Effects of D and He implantation depth on D retention in tungsten under simultaneous D-He ion irradiation.* Physica Scripta, 2016. **T167**: p. 014042.
46. Yajima, M., et al., *In situ observation of structural change of nanostructured tungsten during annealing.* Journal of Nuclear Materials, 2014. **449**(1-3): p. 9-14.
47. S.M. Myers et al., *Hydrogen interactions with defects in crystalline solids.* Reviews of Modern Physics, 1992. **64** p. 559.
48. Terentyev, D., et al., *Dislocations mediate hydrogen retention in tungsten.* Nuclear Fusion, 2014. **54**: p. 042004.

49. M. Wirtz, G. Cempura, J. Linke, G. Pintsuk, I. Uytdenhouwen, *Thermal shock response of deformed and recrystallised tungsten.* Fusion Engineering and Design, 2013. **88**(9-10): p. 1768-1772.
50. *The Plansee Group*. Available from: https://www.plansee.com/en/index.html.
51. Zayachuk, Y., et al., *Deuterium retention in tungsten and tungsten–tantalum alloys exposed to high-flux deuterium plasmas.* Nuclear Fusion, 2012. **53**: p. 103021.
52. Sheng, H., et al., *High temperature strain hardening behavior in double forged and potassium doped tungsten.* Journal of Nuclear Materials, 2014. **444**(1): p. 214-219.
53. Sheng, H., et al., *Mechanical properties and microstructural characterizations of potassium doped tungsten.* Nuclear Engineering and Design, 2012. **246**: p. 198– 202.
54. Ješko, K., et al., *Plasma pressure and particle loss studies in the Pilot-PSI high flux linear plasma generator.* Nuclear Materials and Energy, 2017. **12**: p. 1088–1093.
55. Redhead, P.A., *Thermal desorption of gases.* Vacuum,, 1962,. **12**(4): p. 203-211.
56. Oliver, W.C. and G.M. Pharr, *Measurement of hardness and elastic modulus by instrumented indentation: Advances in understanding and refinements to methodology.* Journal of Materials Research, 2004. **19**(1): p. 3-20
57. Zhou, W., et al., *Fundamentals of Scanning Electron Microscopy (SEM)*, in *Scanning Microscopy for Nanotechnology. Techniques and Applications* 2007. p. 1-40.
58. Adams, B.L., S.R. Kalidindi, and D.T. Fullwood, *Electron Backscatter Diffraction Microscopy and Basic Stereology*, in *Microstructure Sensitive Design for Performance Optimization* 2013. p. 341-371.
59. Dubinko, A., *Plastic Deformation of Tungsten under Fusion-Plasma Exposure Conditions*. 2018, UGent.
60. Butler, T.W., *Report E-69-1 on the determination of dislocation densities*. 1969, United States Naval Academy Engineering Department: Annapolis, Maryland.
61. Schmid, K. and U.v. Toussaint, *Statistically sound evaluation of trace element depth profiles by ion beam analysis.* Nuclear Instruments and Methods in Physics Research Section B 2012. **281**: p. 64–71.
62. Dubinko, A., et al., *Evolution of plastic deformation in heavily deformed and recrystallized tungsten of ITER specification studied by TEM.* International Journal of Refractory Metals and Hard Materials, 2017. **66**: p. 105–115.
63. O. V. Ogorodnikova, J. Roth, M. Mayer, *Ion-driven deuterium retention in tungsten* Journal of Applied Physics 2008. **103**: p. 034902.
64. Alimov, V.K., et al., *Temperature dependence of surface morphology and deuterium retention in polycrystalline ITER-grade tungsten exposed to low-energy, high-flux D plasma.* Journal of Nuclear Materials, 2012. **420**(1-3): p. 519-524.

65. Roth, J. and K. Schmid, *Hydrogen in tungsten as plasma-facing material.* Physica Scripta, 2011. **T145**: p. 014031.
66. Frauenfelder, R., *Solution and Diffusion of Hydrogen in Tungsten.* Journal of Vacuum Science and Technology 1969. **6**: p. 388.
67. Bakaev, A., et al., *Trapping of hydrogen and helium at dislocations in tungsten: an ab initio study.* Nuclear Fusion, 2017. **57**: p. 126040.
68. Grigorev, P.Y., et al., *Interaction of hydrogen with dislocations and grain boundaries in Tungsten.* Journal of Surface Investigation, 2015. **9**(6): p. 1287–1292.
69. Becquart, C.S. and C. Domain, *A density functional theory assessment of the clustering behaviour of He and H in tungsten.* Journal of Nuclear Materials, 2009. **386–388**: p. 109-111.
70. Zayachuk, Y., *Deuterium Retention in Tungsten and Tungsten-Tantalum Alloys under High Flux Plasma Exposure*. 2013, UGent.
71. Rasch, K.D., R.W. Siegel, and H. Schultz, *Quenching and recovery investigations of vacancies in tungsten.* Philosophical Magazine A, 1980. **41**(1): p. 91-117.
72. Dubinko, A., et al., *Effect of high flux plasma exposure on the micro-structural and -mechanical properties of ITER specification tungsten.* Nuclear Instruments and Methods in Physics Research Section B: Beam Interactions with Materials and Atoms, 2017. **393**: p. 155-159.
73. Grigorev, P., et al., *Numerical analysis of TDS spectra under high and low flux plasma exposure conditions.* Physica Scripta, 2016. **T167**: p. 014039.
74. Sun, L., et al., *Hydrogen behaviors in molybdenum and tungsten and a generic vacancy trapping mechanism for H bubble formation.* Journal of Nuclear Materials, 2013. **434**(1): p. 395-401.
75. Jia, Y.Z., et al., *Surface morphology and deuterium retention in tungsten exposed to high flux D plasma at high temperatures.* Journal of Nuclear Materials, 2015. **457**: p. 213-219.
76. Buzi, L., et al., *Influence of tungsten microstructure and ion flux on deuterium plasma-induced surface modifications and deuterium retention.* Journal of Nuclear Materials, 2015. **463**: p. 320-324.
77. Terentyev, D., et al., *Synergy of plastic deformation and gas retention in tungsten.* Nuclear Fusion, 2015. **55**(1): p. 013007.
78. Terentyev, D., et al., *Effect of plastic deformation on deuterium retention and release in tungsten.* Journal of Applied Physics, 2015. **117**(8): p. 083302.
79. H. Eleveld, A. van Veen, *Void growth and thermal desorption of deuterium from voids in tungsten.* Journal of Nuclear Materials, 1994. **212-215**: p. 1421-1425.
80. Lee, S.-C., J.-H. Choi, and J.G. Lee, *Energetics of He and H atoms with vacancies in tungsten: First-principles approach.* Journal of Nuclear Materials, 2008. **383**: p. 244–246.
81. Becquart, C.S. and C. Domain, *Ab initio calculations about intrinsic point defects and He in W.* Nuclear Instruments and Methods in Physics Research B, 2007. **255**: p. 23–26.

82. Lee, H.T., et al., *Hydrogen and helium trapping in tungsten under single and sequential irradiations.* Journal of Nuclear Materials, 2007. **360**(2): p. 196-207.
83. Baldwin, M.J., et al., *Effect of He on D retention in W exposed to low-energy, high-fluence (D, He, Ar) mixture plasmas.* Nuclear Fusion, 2001. **51**: p. 103021.
84. Jiang, B., F.R. Wan, and W.T. Geng, *Strong hydrogen trapping at helium in tungsten: Density functional theory calculations.* Physical Review B, 2010. **81**: p. 134112.
85. Ogorodnikova, O.V., J. Roth, and M. Mayer, *Pre-implantation and pre-annealing effects on deuterium retention in tungsten.* Journal of Nuclear Materials, 2008. **373**: p. 254-258.
86. Heinola, K. and T. Ahlgren, *Diffusion of hydrogen in bcc tungsten studied with first principle calculations.* Journal of Applied Physics, 2010. **107**(11): p. 113531.
87. Becquart, C.S. and C. Domain, *Migration energy of He in W revisited by ab initio calculations.* Physical Review Letters, 2006. **97**(19): p. 196402.
88. Loarte, A., et al., *ELM energy and particle losses and their extrapolation to burning plasma experiments.* Journal of Nuclear Materials, 2003. **313–316**: p. 962-966.
89. M.H.J. 't Hoen, et al., *Saturation of deuterium retention in self-damaged tungsten exposed to high-flux plasmas.* Nuclear Fusion, 2012. **52**: p. 023008.
90. Alimov, V.K., J. Roth, and M. Mayer, *Depth distribution of deuterium in single- and polycrystalline tungsten up to depths of several micrometers.* Journal of Nuclear Materials, 2005. **337–339**: p. 619-623.
91. Delincé, M., P.J. Jacques, and T. Pardoen, *Separation of size-dependent strengthening contributions in fine-grained Dual Phase steels by nanoindentation.* Acta Materialia, 2006. **54**(12): p. 3395-3404.
92. Oliver, W. and G. Pharr, Journal of Materials Research, 2004. **19**: p. 3-20.
93. Fischer-Cripps, A.C., *Nanoindetation, Mechanical Engineering Series*. 2002, Berlin: Springer.
94. Joslin, D.L. and W.C. Oliver, *A New Method for Analyzing Data from Continuous Depth-Sensing Microindentation Tests.* Journal of Materials Research, 1990. **5**(1): p. 123-126.
95. Vlassak, J.J. and W.D. Nix, *Measuring the Elastic Properties of Anisotropic Materials by Means of Indentation Experiments.* Journal of the Mechanics and Physics of Solids, 1994. **42**(8): p. 1223-1245.
96. Zayachuk, Y., et al., *Surface modification of tungsten and tungsten–tantalum alloys exposed to high-flux deuterium plasma and its impact on deuterium retention.* Nuclear Fusion, 2013. **53**: p. 013013.
97. Zayachuk, Y., et al., *Nanoindentation study of the combined effects of crystallography, heat treatment and exposure to high-flux deuterium plasma in tungsten.* Journal of Nuclear Materials, 2017. **486**: p. 183-190.
98. Mecking, H. and U.F. Kocks, *Kinetics of Flow and Strain-Hardening.* Acta Metallurgica, 1981. **29**(11): p. 1865-1875.

99. Shu, W.M., A. Kawasuso, and T. Yamanishi, *Recent findings on blistering and deuterium retention in tungsten exposed to high-fluence deuterium plasma.* Journal of Nuclear Materials, 2009. **386–388**: p. 356–359.
100. Alimov, V.K., et al., *Surface morphology and deuterium retention in tungsten exposed to low-energy, high flux pure and helium-seeded deuterium plasmas.* Physica Scripta, 2009. **T138**: p. 014048.
101. Sharpe, J.P., et al., *Retention behavior in tungsten and molybdenum exposed to high fluences of deuterium ions in TPE.* Journal of Nuclear Materials, 2009. **390391**: p. 709712.
102. Buzi, L., *Influence of the Particle Flux on Surface Modifications of Tungsten*. 2014, UGent.
103. Xu, H.Y., et al., *Deuterium-induced nanostructure formation on tungsten exposed to high-flux plasma.* Journal of Nuclear Materials, 2015. **463**: p. 308–311.
104. Shu, W.M., E. Wakai, and T. Yamanishi, *Blister bursting and deuterium bursting release from tungsten exposed to high fluences of high flux and low energy deuterium plasma.* Nuclear Fusion, 2007. **47**(3): p. 201.
105. Skinner, C.H., et al., *Recent Advances on Hydrogen Retention in ITER's Plasma-Facing Materials: Beryllium, Carbon, and Tungsten.* Fusion Science and Technology, 2008. **54**(4): p. 891-945.
106. Armstrong, D.E.J., P.D. Edmondson, and S.G. Roberts, *Effects of sequential tungsten and helium ion implantation on nano-indentation hardness of tungsten* Applied Physics Letters, 2013. **102**: p. 251901.
107. Zhang, Z.X., et al., *Irradiation hardening in pure tungsten before and after recrystallization.* Fusion Engineering and Design, 2015. **98-99**: p. 2103-2107.
108. Grigorev, P., *Assessment of Retention of Plasma Components in Tungsten under High Flux Plasma Exposure: Multi-Scale Modelling Approach*. 2016, UGent.
109. Bernard, E., et al., *Temperature impact on the micro structure of tungsten exposed to He irradiation in LHD.* Journal of Nuclear Materials, 2017. **484**: p. 24-29.
110. Iwakiri, H., et al., *Microstructure evolution in tungsten during low-energy helium ion irradiation.* Journal of Nuclear Materials, 2000. **283-287**: p. 1134-1138.
111. Dubinko, A., et al., *Sub-surface microstructure of single and polycrystalline tungsten after high flux plasma exposure studied by TEM.* Applied Surface Science, 2017. **393**: p. 330-339.
112. Becquart, C.S. and C. Domain, *An object Kinetic Monte Carlo Simulation of the dynamics of helium and point defects in tungsten.* Journal of Nuclear Materials, 2009. **385**: p. 223-227.
113. Qilai Zhou, K.A., Akihiro Togari, Miyuki Yajima, Masayuki Tokitani, Suguru Masuzaki, Naoaki Yoshida, Masanori Hara, Yuji Hatano, Yasuhisa Oya, *Helium retention behavior in simultaneously He+-H2+ irradiated tungsten.* Journal of Nuclear Materials, 2018. **502**: p. 289-294.
114. Baldwin, M.J., et al., *Effect of He on D retention in W exposed to low-energy, high-fluence (D, He, Ar) mixture plasmas.* Nuclear Fusion, 2011. **51**(12

Paper 1

Dislocation-mediated trapping of deuterium in tungsten under high-flux high-temperature exposures

A. Bakaeva, D. Terentyev, G. De Temmerman, K. Lambrinou, T.W. Morgan, A. Dubinko, P. Grigorev, K. Verbeken, J.M. Noterdaeme

Journal of Nuclear Materials

Volume 479 (2016) Pages 307-315

Journal of Nuclear Materials 479 (2016) 307–315

Contents lists available at ScienceDirect

Journal of Nuclear Materials

journal homepage: www.elsevier.com/locate/jnucmat

Dislocation-mediated trapping of deuterium in tungsten under high-flux high-temperature exposures

A. Bakaeva [a, e], D. Terentyev [a, *], G. De Temmerman [b], K. Lambrinou [a], T.W. Morgan [c], A. Dubinko [a, e], P. Grigorev [a, e], K. Verbeken [d], J.M. Noterdaeme [e]

[a] SCK•CEN, Nuclear Materials Science Institute, Boeretang 200, 2400, Mol, Belgium
[b] ITER Organization, Route de Vinon-sur-Verdon, CS 90 046, 13067, St Paul Lez Durance Cedex, France
[c] FOM Institute DIFFER, De Zaale 20, 5612 AJ, Eindhoven, The Netherlands
[d] Department of Materials Science and Engineerin, Ghent University, St. Pietersnieuwstraat 41, 9000, Ghent, Belgium
[e] Department of Applied Physics, Ghent University, St. Pietersnieuwstraat 41, 9000, Ghent, Belgium

ARTICLE INFO

Article history:
Received 23 March 2016
Received in revised form
5 July 2016
Accepted 6 July 2016
Available online 9 July 2016

Keywords:
Dislocations
Tungsten
Retention
Hydrogen

ABSTRACT

The effect of severe plastic deformation on the deuterium retention in tungsten exposed to high-flux low-energy plasma (flux ~10^{24} m^{-2} s^{-1}, energy ~50 eV and fluence up to 5 × 10^{25} D/m^2) was studied experimentally in a wide temperature range (460–1000 K) relevant for application in ITER. The desorption spectra in both reference and plastically-deformed samples were deconvoluted into three contributions associated with the detrapping from dislocations, deuterium-vacancy clusters and pores. As the exposure temperature increases, the positions of the release peaks in the plastically-deformed material remain in the same temperature range but the peak amplitudes are altered as compared to the reference material. The desorption peak attributed to the release from pores (i.e. cavities and bubbles) was suppressed in the plastically deformed samples for the low-temperature exposures, but became dominant for exposures above 700 K. The observed strong modulation of the deuterium storage in "shallow" and "deep" traps, as well as the reduction of the integral retention above 700 K, suggest that the dislocation network changes its role from "trapping sites" to "diffusion channels" above a certain temperature. The major experimental observations of the present work are in line with recent computational assessment based on atomistic and mean field theory calculations available in literature.

1. Introduction

Tungsten (W) is the main candidate plasma facing material (PFM) of a fusion reactor (see e.g. Refs. [1,2]). Although W clearly has a number of advantages, the retention and permeation of hydrogen isotopes (HI) remain a concern for both the efficient operation and safety of the reactor, given the extreme operation conditions that the PFM must sustain during service (e.g. see recent review by Tanabe [3]).

While at the low-temperature limit (450 K) the bulk permeation is suppressed and the formation of HI bubbles and cavities occurs mainly in the sub-surface region [3], at the high-temperature limit (1000 K and above), a significant contribution of the bulk retention at a depth of millimeter and beyond is to be accounted for. Another important point is that sub-surface trapping, expressed in the formation of bubbles and accompanied by plastic deformation and blistering, is a non-equilibrium process primarily defined by the combination of plasma flux, surface temperature (and its gradient towards the bulk) and material microstructure [3]. The latter truly plays a crucial role because it defines the density and strength of trapping sites inducing the formation of HI clusters that cannot nucleate otherwise in the perfect bulk, due to the absence of hydrogen self-trapping in bcc W [4,5]. Moreover, the initial microstructure of the PFC material will undergo constant modification due to the formation of plasma-induced defects (such as bubbles [6] and dislocation tangles [7]), neutron irradiation lattice defects (Frenkel pairs and their clusters [8]) and thermal fatigue-induced defects (dislocation pile-ups and slip bands [9]). That is why significant effort is currently devoted to understanding the role of the initial microstructure in the HI permeation, dynamic trapping and release.

* Corresponding author.
E-mail address: dterenty@sckcen.be (D. Terentyev).

http://dx.doi.org/10.1016/j.jnucmat.2016.07.018
0022-3115/

Among the naturally existing and radiation-induced defects, the following are of special relevance with respect to HI retention: vacancies (and small vacancy clusters), voids, grain boundaries and dislocations. Trapping at dissolved interstitial impurities (C, O) is also possible, but generally considered to be too weak to initiate nucleation of HI bubbles at temperatures above 450 K [3]. Focus is, therefore, put on studies allowing to reveal (and preferably understand) the role played by each type of the above mentioned defect microstructures.

Implantation with high-energy H ions is an efficient way to address trapping at point defects, as one can select the beam energy in the narrow range needed to create Frenkel pairs without producing collision cascades [10]. Investigation of ion pre-implanted samples is more complex, but allows one to probe samples that contain both dislocation loops and voids simultaneously [11]. Comparison of results obtained using single crystals and recrystallized polycrystalline grades allows to reveal the trapping efficiency of grain boundaries (GBs). Recently, a comparison of HI retention and microstructure after high-flux deuterium (D) plasma exposure was performed in recrystallized and heavily plastically deformed samples [12,13]. All microstructural features, except from the dislocation density (increased by two orders of magnitude), remain the same after plastic deformation. The exposures were performed at 450 K (low-temperature limit) in the dose range of 8×10^{24}–3×10^{26} D/m^2/s, using the high-flux linear plasma accelerator PILOT-PSI.

The obtained results have shown that heavy plastic deformation increases the total D retention by ~50%, as compared to the reference recrystallized sample. The contribution of D trapping by pores to the total retention is suppressed by plastic deformation up to a certain dose and increases beyond it. This has been explained by the dual role of the dislocation network: on one hand offering preferential nucleation sites, and on the other hand delaying the formation of HI bubbles to a higher dose as compared to the reference sample, due to the increased density of trapping sites. Hence, the plastically-induced dislocation network delays the formation of large HI bubbles, but such delaying capacity is limited.

To extend our understanding of the role played by plastic deformation in the HI diffusion, trapping and release processes, it is important to screen the effect of temperature and in particular to reveal whether the dislocation-enhanced retention also occurs above 800 K, where the retention in low-dislocation density grades (i.e. coarse-grained and recrystallized grades) strongly decreases [14]. In this work, we perform a series of high-flux exposures in the 470–1000 K range, using the same flux exposure parameters, detection/analysis techniques and material as in earlier studies [12,13].

2. Experimental details

The pristine material used in this study was a polycrystalline W of 99.99% purity, provided in a rod form by Plansee AG [15]. The main impurities, as reported by the manufacturer, are listed in Table 1. The removal of initial residual stresses was performed by a thermal treatment at 1273 K, followed by recrystallization at 1873 K for 1 h. Generally, the microstructure of the as-received material consisted of large random grains (separated by high-angle GBs) that contained subgrains (separated by low-angle GBs), while dislocations were present both inside the grains as well as at low-angle GBs. Upon thermal annealing (at 1873 K), microstructural recovery was expressed in a limited subgrain growth, removal of a significant amount of subgrains and reduction in the dislocation density. The grain size of the as-annealed material typically varied in the 50–150 μm range and the dislocation density was about 5×10^{12} m^{-2}.

The samples intended for tensile plastic deformation were cut from the as-annealed rods. To release the stress introduced by electric discharge machining (EDM), the tensile samples were re-annealed at 1273 K for 1 h in an argon (Ar) atmosphere. Several tensile tests were performed at 873 K in air at a deformation rate of 0.2 mm/min to reach 28% deformation. The latter approximately corresponds to the ultimate tensile strength of the studied W grade. Transmission electron microscopy (TEM) and electron backscatter diffraction (EBSD) samples were cut from the middle of the samples and re-annealed at 873 K for three hours prior to the examination to remove the EDM-induced defects without affecting the dislocation microstructure.

The microstructure of the annealed and plastically-deformed tungsten samples was studied. Scanning electron microscopy (SEM) analysis of the as-annealed samples revealed the growth of random grains up to 150 μm, and the strong reduction of the fraction of low-angle GBs down to about 20%. Examples of EBSD grain orientation maps are given in Fig. 1a and b for as-annealed and plastically-deformed samples, respectively. Three main crystallographic orientations of the W bcc lattice (i.e. ⟨111⟩, ⟨001⟩ and ⟨101⟩) can be identified on the EBSD maps. Fig. 1a and b shows that the large random grains are practically free of subgrains and that small grains (5–10 μm) are rarely observed.

In the case of the deformed material (Fig. 1b), the effect of tensile loading is obvious and one can see that the grains are elongated in accordance with the orientation of the sample with respect to the tensile loading direction. However, the applied deformation did not result in grain refinement that was clearly detectable by means of EBSD. To provide a deeper insight in the possible microstructural modifications induced by plastic deformation, a TEM investigation was performed.

TEM samples ($10 \times 3 \times 1.25$ mm^3) were extracted from the middle of both as-annealed and as-deformed specimens (plates with dimensions of $10 \times 10 \times 1.25$ mm^3) by EDM. These pieces were then mechanically polished from both sides using SiC paper (grits: 220, 500, 1200 and 4000) to achieve 70–100 μm thickness and further cut with a wire cutter into pieces to fit 3-mm diameter TEM grids. They were polished again from both sides with 4000 SiC paper to remove the remnants of glue, rinsed in acetone and ethanol and then glued on ∅ 3-mm copper grids with an aperture of 1 mm. Finally, the specimens were polished electrochemically with a solution of 1.5 wt% NaOH in water using an applied voltage of 15 V. The specimens were investigated by means of a JEOL 2010 TEM operating at 200 kV and a JEOL 3010 TEM operating at 300 kV. Examples of bright field TEM images of dislocations observed in as-received and plastically-deformed samples are presented in Fig. 1c and d. The presence and density of dislocations was inhomogeneous in the as-annealed sample, even within a single grain. After plastic deformation, dislocations became evident everywhere in the sample visible area, while the scatter in their spatial distribution was reduced.

The average dislocation density was measured based on the method described in Ref. [16]. Several calculations at different specimen areas were performed to get an average dislocation density. Each calculation requires a TEM micrograph, corresponding selected area diffraction (SAD) pattern and convergent beam electron diffraction (CBED) pattern. In the Digital Micrograph software, which is provided with the image sensor of the TEM, a circle is drawn randomly in an image and the number of its intersections with dislocation lines is counted. The dislocation density is then calculated as $\rho = 2N/Lt$, where N is the number of intersections of the circle with dislocation lines, L is the circle diameter, and t is the local thickness of the specimen in the area of the image. The length of the circle is automatically calculated by the Digital Micrograph software. The local thickness of the specimen is

Table 1
Impurity content of the W batch used in this study, as specified by the material supplier.

Impurity	Ag	Ba	C	Fe	Mn	Ni	Ti	Mo	Co	O	Si	Al	Ca	Cr	K
(μg/g)	10	5	10	30	5	5	5	100	30	20	20	15	5	20	10
Impurity	Na	Pb	Zn	H	Pb	As	Cd	Cu	Mg	Nb	Ta	Zr	N	S	
(μg/g)	10	5	5	5	20	5	5	10	5	10	20	5	5	5	

determined from the CBED and SAD patterns. The resulting dislocation density in the 28% deformed sample was found to be about 2×10^{14} m^{-2}, i.e. nearly two orders of magnitude higher than that in the as-annealed sample. Detailed information about mechanical properties and primary microstructure of the tungsten grade studied here can be found in Ref. [17].

The samples for the plasma exposure were of square shape with dimensions of 10 × 10 × 1 mm being mirror polished from the exposure side and flattened on the other side. Exposures to deuterium plasma were performed at the linear plasma generator PILOT-PSI [18,19], employing high-density plasma mimicking the 'sub-displacement threshold' plasma-wall interaction conditions expected in the ITER divertor. The energy of the deuterium ions was ~50 eV (controlled by negatively biasing the target), while energies in excess of 900 eV are required to initiate atomic displacement in W. Although the plasma beam is non-uniform, the size of the sample corresponded to the full width at half maximum, i.e. 10 mm, which ensured limited temperature and flux gradients across the surface during the exposure, as measured and confirmed in-situ by an infra-red camera (FLIR A645 sc) during the exposure. The average particle flux across the sample was in the $(0.9–2.8) \times 10^{24}$ D/m^2/s range, depending on the desired exposure temperature. The flux was calculated from the plasma electron density and electron temperature, as measured by Thomson scattering [20] at a distance of ~25 mm upstream from the plasma-facing surface. Special care was taken to perform all exposures at as identical conditions as was technically achievable. Four pairs of W samples (i.e. deformed and reference ones) were exposed to a fluence of $F = 10^{26}$ D/m^2 at 460, 600, 820 and 1000 K. The variation of the temperature across the sample surface typically does not exceed 10–20 K once the steady-state regime is reached.

The surface of the exposed samples was inspected by SEM both before and after thermal desorption spectroscopy (TDS) to check whether the pattern of blisters (if any) was modified during TDS measurements. SEM images for the samples exposed at 470K are presented in our earlier work [12,13]. Observation of fine features of microstructure were acquired using a secondary electron detector, so as to effectively reveal the small (1–2 μm) blisters on the surface of the W specimens. The employed SEM was a JEOL JSM-6610LV (JEOL, Tokyo, Japan) and the operating conditions were: 20 kV accelerating voltage and 12–20 mm working distance. SEM inspection was primary used to confirm the formation of blisters, while the in-depth investigation of surface and sub-surface microstructure will be reported in our upcoming work. Here, we make a focus on study of D release.

Retention measurements were performed by means of TDS. The maximum temperature was 1273 K, the heating/cooling rate was 0.5 K s^{-1} and the holding time at the maximum temperature was 5 min. The release flux of molecular HD and D_2 was measured by a quadrupole mass spectrometer. Quantification of the mass four

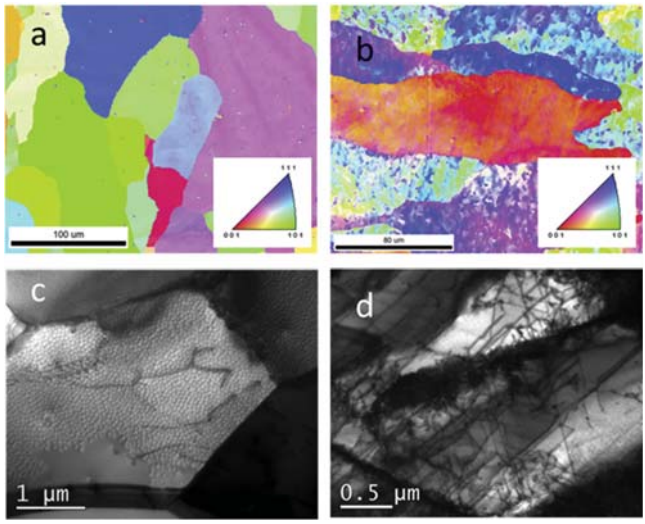

Fig. 1. Tungsten EBSD grain orientation maps in the (a) as-annealed and (b) as-deformed (28% strain) states. In Fig. 1b, the direction of applied tension is along the scale bar. TEM bright field images showing a typical dislocation pattern in tungsten corresponding to the (c) as-annealed state (g = (2$\bar{1}$ 1) and close to the [113] zone axis) and (d) 28% deformed state (g = (1$\bar{1}$ 2) and close to the [111] zone axis).

signal (corresponding to the release of D_2) was performed using a calibrated D_2 leak. Quantification of the mass three signal (corresponding to HD release) was performed using the averaged value of the signals of two calibrated leaks: H_2 and D_2. During the measurement, it has been observed that the signal of mass four (D_2), measured on all exposed samples, was orders of magnitude higher than the signals of mass 19 (HDO) and 20 (D_2O) that were at the level of the background noise. The signal of mass three (HD) was also considerably lower as compared to D_2, proving that prior exposure degassing was efficient to remove major fraction of hydrogen. The total deuterium retention was, therefore, measured by the release of D_2.

3. Results and discussion

3.1. SEM microstructure

In all samples, blisters were observed on the sample surface, with preferential blistering on {111}-oriented grains. The observation of blisters, even at temperatures as high as 1000 K, is in line with the results of recent works by Jia et al. [21] and Buzi et al. [22], where different W grades of commercial purity were exposed to a high-flux plasma at the same plasma generator and in similar conditions. The blister size distribution was clearly bi-modal: small blisters (0.2–0.6 μm) with high density and small size were dominant on the surface of samples exposed at 800 K and 1000 K, whereas large (1–3 μm) dome-shaped and less numerous blisters were observed on samples exposed at lower temperatures. At 800 K, the areal density of the small blisters was of the order of 10^{12} m^{-2} in the as-annealed samples and 5×10^{12} m^{-2} in the plastically deformed samples. In-depth characterization of the surface and sub-surface microstructure by SEM and TEM techniques is ongoing and will be reported elsewhere.

3.2. TDS measurements and interpretation of the release stages

Figs. 2 and 3 depict the TDS spectra measured on the reference and plastically-deformed samples. Following the previous analysis based on the results of the exposures at 460 K, we have deconvoluted the spectra into three major Gaussian peaks (henceforth referred to as P_1, P_2 and P_3), as shown in Fig. 2a. In our previous work, we have argued that each release stage corresponds to detrapping from a different type of defects, namely: P_1-dislocations, P_2-D clusters occupying jogs on dislocation lines, and P_3-pores (i.e. D bubbles and cavities, associated with the blister appearance).

As can be seen in Figs. 2 and 3, the appearance and amplitude of the three peaks depends on the exposure temperature and pre-deformation applied. Typically, the exposure in the 460–800 K temperature range leads to the positioning of the three peaks around 450–550 K, 600–700 K and 700–800 K for P_1, P_2 and P_3, respectively. After a high-temperature exposure (i.e. at 1000 K), the major release occurs in the 700–1200 K temperature range, and we, therefore, attribute the measured desorption to the detrapping from pores. It is to be noted that the exact position of the peaks slightly changes depending on the exposure temperature, but there is no clear trend to be deduced. For the cases when the shift occurs towards a higher temperature, such as the case of peak P3, we attribute this to the thermally-activated deeper diffusion of D in the bulk. Since the peaks are clearly distinguishable from each other and are confined in a limited temperature range, we consider the detrapping to occur via the three principal mechanisms discussed below.

The nature of the first peak (P_1) was analyzed in our previous work, where exposures at 470 K up to different fluences were studied. The occurrence of this peak strongly correlates with the dislocation density, and a rough estimation of the detrapping energy is about 0.8–1 eV. The value of this detrapping energy is in line with the available computational data for the binding of hydrogen to a screw dislocation - 0.6 eV (and unpublished data for the edge dislocation – 0.89 eV) [6] plus its migration energy (according to ab initio calculations 0.25–0.4 eV [23,24] and experimental results 0.4 eV [25]).

The rough estimation of the activation energy for the P_2 peak provides a value of 1.3–1.5 eV, which is conventionally attributed to the trapping at vacancies. In our previous work [13], we have pointed out that the formation of non-equilibrium D clusters on dislocations or at dislocation junctions may result in the punching of jogs. In this way, a cluster of interstitial D atoms would transform into an over-pressured nano-bubble capable to grow further by emitting dislocation jogs. In this case, the D trapping should be associated with the vacancy dislocation jog, which has nearly similar trapping energy profile as a single vacancy, as demonstrated by first principle calculations [26]. Hence, such a mechanism explains the presence of this release stage with features similar to the trapping at vacancies. Note that the equilibrium vacancy concentration at temperatures below 1000 K is extremely low and cannot explain the amount of stored D, as has been analyzed and discussed in Ref. [6]. Therefore, we shall attribute P_2 to the storage of D in small clusters formed on dislocation lines, and hence its intensity (and presence) is linked to the capacity of dislocation lines to act as traps assisting the nucleation of plasma-induced defects (vacancy-jogs).

Finally, the high-temperature peak (P_3) is conventionally attributed to the release from pores (i.e. voids and cavities with the activation energy of about 2 eV, see e.g. Ref. [3]) that can be delayed due to the long-range diffusion process and sub-surface retrapping originating from the presence of emptied but not yet recovered nano-voids. Separating the contributions of the bulk release from the sub-surface one is a complicated matter and lies outside the scope of the present work. We shall limit ourselves in stating that the increase in P_3 intensity, broadening and shift towards high temperatures indicate both deep diffusion and storage of D in large bubbles.

The justification for the formation of the other two sub-stages (i.e. $P3_1$ and $P3_2$, see Figs. 2d and 3d) could lie in the presence of a bi-modal size distribution of bubbles (as mentioned in the previous section), so that the release from larger bubbles is delayed. The theoretical argumentation and estimation of the shift in the high-temperature peak depending on the bubble size has been reported in Ref. [27].

The effect of the exposure temperature and the initial microstructure are of crucial importance, first because the increase in surface temperature promotes both the diffusion of D and the formation of larger bubbles. The growth of bubbles is promoted by the temperature increase because the trapping at dislocations is no longer effective to induce the intensive bubble nucleation. Consequently, the concentration of the bubbles decreases, but their size increases, respectively. Bubbles mainly nucleate at strong traps, such as grain boundary triple junctions and other bulk imperfections with a considerable open volume. Consequently, the density of stable bubbles is reduced and they may grow faster (larger income flux per bubble). Given a significant difference in the bubble size (e.g. 10 vs. 100 nm), quantitative estimations based on atomic-scale modeling suggest the shift of the release peak to be in the order of 100 K [27], which is in line with the spacing of $P3_1$ and $P3_2$. Given the above, when discussing the fractional D uptake per each type of the trap, we shall not consider separately the three sub-peaks observed in the highest temperature exposure and attribute them all to the release from pores.

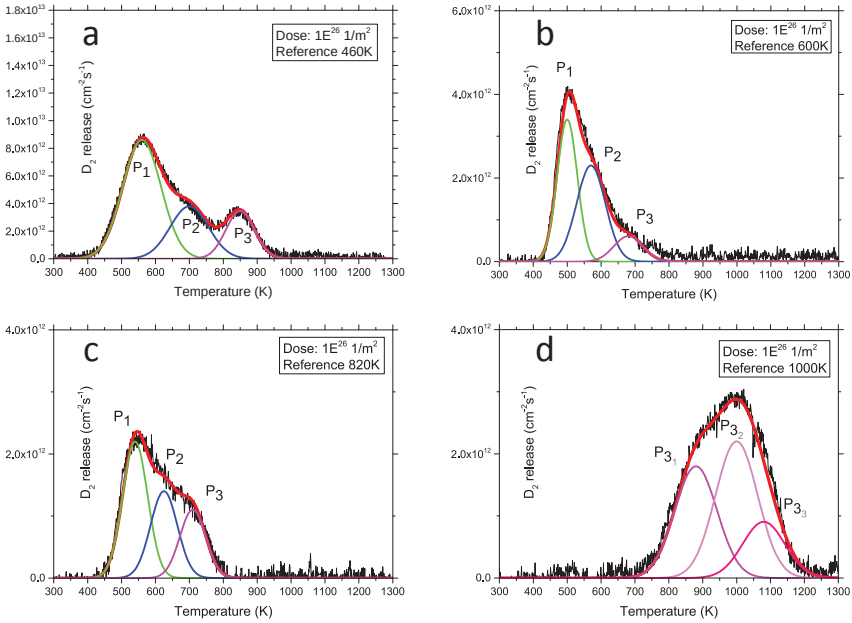

Fig. 2. Deconvoluted TDS spectra of the reference samples exposed at (a) 460 K, (b) 600 K, (c) 820 K and (d) 1000 K. The black curve corresponds to the experimental data, the red curve is the superposition of the three (in the general case) Gaussian functions. The latter are shown by green, blue and magenta, attributed to release stage I, II and III, respectively. (For interpretation of the references to colour in this figure legend, the reader is referred to the web version of this article.)

Finally, we would like to draw attention to the fact for the exposure at 600 K and above, the release of D has started below the exposure temperature. This is observed for both reference and deformed samples. We attribute this feature to the specificity of the exposure conditions (i.e. high flux resulting in a strong gradient of trapped D under surface) and cooling solution (i.e. rapid cooling to room temperature as soon as the exposure is stopped). A typical time for the cooling of the surface down to the room temperature is about 2–3 s, depending on the target exposure temperature. Consequently, not all D detrapped from weak traps (dislocations and vacancies) is fast enough to reach the surface and escape from the sample. In addition, the diffusion of D from bulk towards surface will be conducted by often re-trapping events at the defects already emptied from D. Such re-trapping process during the cooling stage may result in the formation of multiple vacancy-D_N clusters (up to 6 atoms can be bound to a single vacancy [5], and up to eight atoms to a superjog on the dislocation [6]), whose break-up is expected to occur in the temperature range 400–600 K. Quantitative estimations of the re-arrangement of D among different traps under the cooling stage requires further dedicated numerical simulations.

Note that the above provided discussion for the release peaks and their evolution as a function of exposure temperature is based on an oversimplified picture, assuming that the major part of D is stored within a thin region under surface (tens of μm or less). In the present work, we did not perform depth profile measurements, however, the available data from NRA [28] and SIMS [22] for the exposures done in polycrystalline W in similar conditions point to the fact that major fraction of D is indeed stored within a subsurface region of several μm. What cannot be easily extracted from NRA and SIMS is the structure and morphology of defects containing D atoms. Following the discussion in Ref. [4], the nucleation of vacancy-like traps on dislocation lines and their evolution is extremely sensitive to the local temperature, local flux and density of lattice defects (i.e. primarily dislocations). In turn, the occupation of different types of traps will have a strong influence on the peak shapes and positions. The temperature distribution across the sample depth was calculated by solving the heat equation at the steady state with the boundary conditions defined by the surface and back-side temperature. It was found that the reduction of temperature from the surface towards bulk remains within 10 K for the first 10 μm at the highest exposure temperature. The gradient is even smaller for the lower exposure temperatures. Understanding of the role played by initial microstructure and non-equilibrium trapping in the appearance of the TDS peaks requires further thorough modeling, which is out of scope of the present work.

3.3. Analysis of the TDS peak intensity

The fraction (expressed as % of the total retention) of the D released through stages I, II and III is shown in Fig. 4 for both types of samples. The fraction is defined as an integral under the Gaussian function attributed to a certain stage and normalized by the total D release. The following general trends can be clearly identified:

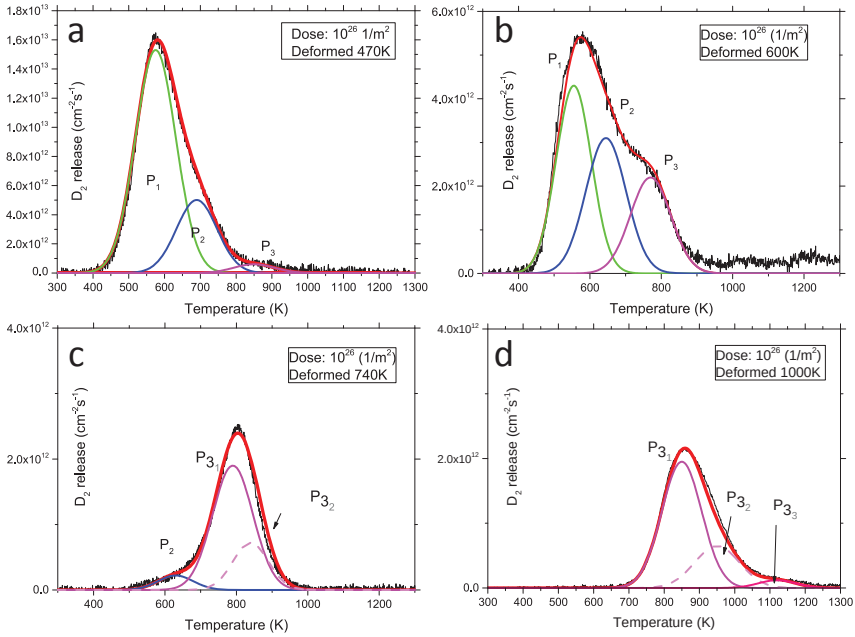

Fig. 3. Deconvoluted TDS spectra of the plastically deformed samples exposed at (a) 470 K, (b) 600 K, (c) 740 K and (d) 1000 K. Note that a single Gaussian function is not enough to describe the experimentally measured desorption at 1000 K and, therefore, we divide P_3 into three sub-peaks. Among these three sub-peaks, there is a high-temperature release stage ($P3_3$) around 1000–1200 K that is evident in both types of samples. We attribute this high-temperature peak to the slow diffusion of D from the bulk to the surface, which is conducted by continuous trapping-retrapping at the already emptied pores.

(i) The intensity of P_1 monotonically decreases with the exposure temperature, becoming negligible at 1000 K. Since this release has been attributed to the detrapping from bulk dislocations, one realizes that this mechanism is no longer effective when the exposure temperature exceeds 800 K. Apparently, the high surface temperature facilitates frequent detrapping from dislocations, so that the major fraction of D is distributed at grain boundaries (likely high-angle GBs with a higher binding energy and interface migration energy). The diffusion towards bulk in such a situation should be controlled by trapping at and diffusion along grain boundaries.

(ii) The intensities of P_2 and P_1 are strongly interrelated. Given that the P_2 release stage has been attributed to the detrapping from vacancy-jog clusters, it is natural to expect that the de-activation of dislocation trapping above 800 K will also eliminate the formation of dislocation-attached defects. The combined effect of temperature and flux on the nucleation of dislocation-mediated D clusters is also consistent with the computational assessment performed in Refs. [26,29]. In particular, it was demonstrated that above 800 K at a flux of 10^{24} D/m^2/s, the desorption rate exceeds the incoming rate, thus preventing the nucleation of stable D clusters by punching dislocation jogs.

(iii) The intensity of P_3 monotonically increases with the exposure temperature, reaching 100% at 1000 K. This peak has been attributed to the D release from nano-metric bubbles and larger cavities that contribute to blister formation in the sub-surface, as well as to the delayed release from the bulk due to the retrapping diffusion process.

Apart from the above general trends, several additional features can be distinguished. The fractional contribution of the release attributed to dislocations (P_1) prevails in both samples up to 600 K and then strongly decreases. However, it vanishes at 800 K in the deformed samples, while it remains present up to 800 K in the reference samples. This behavior can be attributed to the change of the major trapping and diffusion mechanisms that apparently occurs in the 600–800 K temperature range, depending on the dislocation density (and given the applied plasma flux in this study). Indeed, below 600 K, diffusion is mainly governed by the trapping of D at bulk dislocations, while migration occurs along dislocation lines and storage of D takes place in clusters formed at dislocations as well as GBs.

The binding of D to grain boundary interfaces is expected to be stronger as compared to its binding to dislocations, so the diffusion is essentially limited within the first layer of grains in low-temperature exposures. Above 600 K, D atoms quickly diffuse via dislocation lines to the GBs, migrate preferentially along the GB interfaces (while being bounded) and form clusters there. Hence, some fraction of the penetrated D is stored in sub-surface bubbles, while the remaining D diffuses deeper into the bulk. Apparently, a

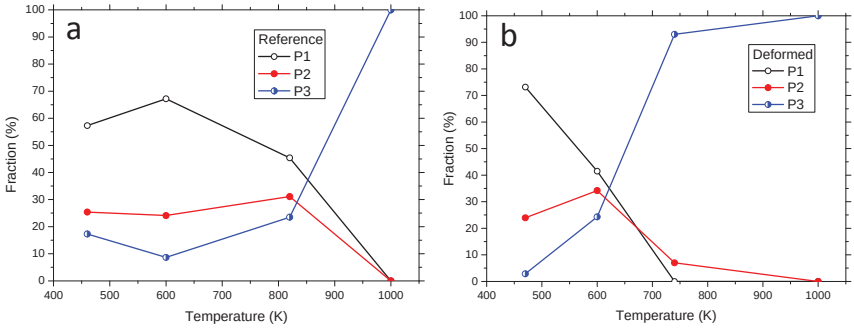

Fig. 4. Fraction of D integrated over the Gaussian functions assigned to the release at stages I, II and III in (a) reference and (b) plastically deformed samples.

high dislocation density reduces the effective diffusion coefficient (due to the trapping-retrapping process), which results in a different concentration profile of permeating D along the sample depth. Hence, for a given fluence, the concentration and diffusion depth of bulk-permeated D is higher in the reference material as compared to the plastically-deformed one. Note that there is a temperature gradient from the surface to the bulk, since the bottom part of the sample is under active cooling at ~300 K. Deep diffusion to the colder region may explain why the contribution from dislocation retrapping in the as-annealed sample lasts up to 800 K, while it is strongly reduced in the deformed material.

The sub-surface layer of the plastically deformed material, where the trapping on plasma-induced defects prevails, saturates faster with D as the temperature increases, a fact that can explain faster transformation of D clusters into nano-bubbles, seen as the P_3 release peak. Correspondingly, D is mainly stored in nano-bubbles already at 800 K in the deformed sample, while this fraction is only about 20% in the reference sample.

3.4. Integral retention

The data for the total (or integral) retention are summarized in Fig. 5. As was already shown in Refs. [13], plastic deformation affects both the shape of the TDS release spectra and the total retention over the entire temperature range studied so far. Below 600 K, the deformation enhances the integral retention, while above 600 K, it reduces the retention. This supports the argumentation of the modification of the mechanism controlling the D uptake from sub-surface trapping on plasma-induced defects (driven by dislocations) to deep diffusion. Plastic deformation suppresses the total retention above 600 K, which is another evidence of the efficient reduction of deep diffusion by the dislocation network in addition to the discussion in Section 3.3. However, one should take into account that at sufficiently high fluence, the saturation of the trap capacity must vanish the reduction of the deep diffusion. Hence, the observed effect of plastic deformation is only temperature- but also fluence-dependent feature.

The comparison of our results with data coming from high-flux and medium-flux exposures reported in literature is presented in Fig. 5. Our results are in reasonable agreement with the total retention reported in other works involving medium flux (10^{22} D/m^2/s, and the same fluence as in the present case) plasma exposures of polycrystalline W up to 600 K. Above that temperature, exposures at medium flux reported strong retention reduction by at least one order of magnitude, while saturation is observed in the present work. A similar trend for the saturation in the 600–1000 K temperature range was also reported in other studies that employed high-flux exposures [21,22]. Although three independent studies employed polycrystalline W grades of different origin and purity (99.95 in Refs. [21], 99.99% here and 99.94% in Ref. [22]), the trend of the saturation of the D retention up to 1000 K is evident. Hence, the deviation of the total retention in the exposures above 600 K in medium- and high-flux exposures must be attributed to the flux effect rather than to possible microstructural differences (grain size, dislocation density) or the impurity contents of the exposed W grades.

The data obtained by Jia et al. [21] and Buzi et al. [22] and, deviate from ours in the sense that a much higher retention was found at 490 K and essentially a lower retention was reported for the 900–1100 K temperature range. In both works, a technically pure polycrystalline W grade was used, with a similar grain size as the W grade studied here. The difference in the obtained results may originate from the size of samples used in the studies of Jia et al. and Buzi et al. While our samples were square plates of $10 \times 10 \times 1$ mm^3, Jia et al. used ∅ 30 mm disks and Buzi et al. used ∅ 14 mm disks, which must have resulted in different plasma current profile and temperature distribution across the exposed sample surface. That explains why the appearance of the exposed surfaces (i.e. blister size and density) observed within the area of the focused beam was generally the same, while the integral retention, especially at high temperatures, differed considerably. One also must note that the present results correspond to a fluence of 10^{26} m^{-2} and the retention is probably not yet saturated. According to Jia et al. the saturation fluence is 4×10^{26} m^{-2}, while the saturated retention is also added in Fig. 5.

4. Summary and conclusive remarks

The parametric study performed in this work on reference recrystallized and plastically-deformed W samples has shown that substantial plastic deformation affects both the total retention and distribution of D in different types of traps. The principal difference between two sets of samples exposed in the 460–1000 K temperature range was the dislocation density, ranging from 5×10^{12} in the reference samples to 2×10^{14} m^{-2} in the plastically-deformed samples. It was established that the effect originating from an increased dislocation density depends strongly on the exposure temperature. At low temperatures, plastic deformation suppresses

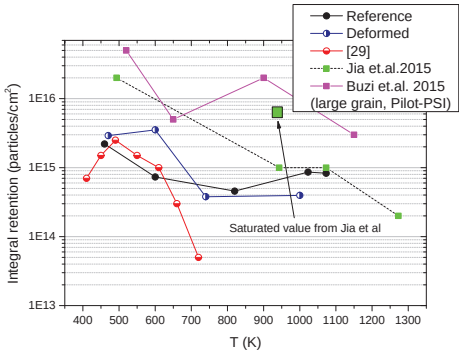

Fig. 5. Total retention measured in this work as compared with the data reported in literature [21,22], where the retention was measured in similar high-flux plasma exposures and comparable W grades (except from the work of Alimov et al. [14], where a lower flux was applied). The data point labeled as "Saturated value from Jia et al." corresponds to the retention measured at the fluence of 5×10^{26} D/m^2, at which the saturation of the retention has been identified to take place.

the growth of bubbles/cavities, but enhances the total retention. At high temperatures, plastic deformation actually reduces the total retention. The cross-over temperature between these two regimes is around 600–700 K.

Given the discussion provided in Section 3, we attribute the physical explanation of this transition to the existence of two processes that dominate at "high" and "low" temperature regimes and are interrelated with the dislocation density. In the low temperature regime, the retention is mainly assisted by trapping and nucleation of bubbles at bulk dislocations (and dislocation junctions). In the high temperature mode, the retention is mainly driven by the long-range diffusion in the bulk. Following the discussion provided in Section 3, a high dislocation density enhances the nucleation of plasma-induced defects in the low-temperature exposures, while hindering the long-range bulk diffusion in the high-temperature exposures.

On the basis of the evolution of TDS spectra versus exposure temperature, the transition between low- and high-temperature trapping processes occurs around 600–700 K. Under the assumption that the trapping of D and nucleation of plasma-induced defects is assisted by the dislocation networks, we suggest that 600–700 K is the upper limit for the dislocation-dominating trapping in the ITER-relevant high flux mode (i.e. as the case studied here). The threshold temperature is expected to decrease with the reduction of the plasma flux, as the dislocation-assisted trapping is a temperature- and flux-dependent process.

At this point, however, it is still too early to make a firm conclusion on the role played by temperature and dislocation density in the present rather complex experiment. Requirements for the high flux and high temperature plasma mimicking ITER conditions unfortunately impose certain limitations on the uniformity of the flux profile across the sample surface, backside cooling induces strong temperature gradient at the end of the exposure. In combination, it leads to the heterogeneous distribution of trapped D in both radial and normal-to-plasma beam directions. Without knowing the depth and surface profiles of the D retained in different parts of the sample and preferably also at a depth below typical resolution of NRA, one cannot make rigorous modeling to re-affirm the source of the release peaks and their evolution with the exposure temperature or initial microstructure. As of now, we expect that the after-exposure fast cooling explains the low temperature release stages, which occur at the temperature below the exposure temperature. Because of the fast cooling (several seconds to reach room temperature) only a part of D atoms reaches the sample surface and desorbs during the cooling. A certain amount is retained because of the slow diffusion hindered by the retrapping (trapping in sub-surface region on emptied traps). The heterogeneity of the flux profile is another technically unavoidable issue. Although the flux increases only by a factor of three from the edge to the center of the sample, one cannot rule out the modification of the trapping depth profile, which inherently affects the TDS spectrum. As a result, we measure the effective spectrum being a superposition of the spectra corresponding to different depth profiles in the center and at the edge of the sample. To clarify the above discussed issues, we plan to perform experiments using a combination of NRA and TDS techniques, and by selecting several areas of the target as well as applying flash electro-chemical polishing to remove sub-surface layer in controlled manner. Sub-sequent removal of the sub-surface layer and NRA measurements will enable us clarifying the impact of exposure temperature and initial microstructure on the bulk-retention.

Acknowledgements

This work has been carried out within the framework of the EUROfusion Consortium and has received funding from the Euratom research and training programme 2014–2018 under grant agreement No 633053. The views and opinions expressed herein do not necessarily reflect those of the European Commission. The authors thank referees for the in-depth discussion and contribution made upon the reviewing stage to improve this work.

References

[1] M. Rieth, D. Armstrong, B. Dafferner, S. Heger, A. Hoffmann, M.-D. Hofmann, U. Jäntsch, Adv. Sci. Technol. 73 (2010) 11–21.
[2] M. Rieth, S.L. Dudarev, S.M.G. de Vicente, J. Aktaa, et al., J. Nucl. Mater. 432 (2013) 482–500.
[3] T. Tanabe, Phys. Scr. T159 (2014).
[4] V. Dubinko, P. Grigorev, A. Bakaev, D. Terentyev, G. Van Oost, F. Gao, D. Van Neck, E.E. Zhurkin, J. Phys. Condens. Matter 26 (2014) 395001.
[5] K. Heinola, T. Ahlgren, K. Nordlund, J. Keinonen, Phys. Rev. B 82 (2010) 094102.
[6] D. Terentyev, V. Dubinko, A. Bakaev, Y. Zayachuk, W. Van Renterghem, P. Grigorev, Nucl. Fusion 54 (2014) 042004.
[7] A. Dubinko, A. Bakaeva, M. Hernandez-Mayoral, D. Terentyev, G. De Temmerman, J.M. Noterdaeme, Phys. Scr. T167 (2015) 014030.
[8] A.E. Sand, K. Nordlund, S.L. Dudarev, J. Nucl. Mater. 455 (2014) 207–211.
[9] W. Van Renterghem, I. Uytdenhouwen, T. Loewenhoff, M. Wirtz, Nucl. Mater. Energy Accept. Publ. (2016), http://dx.doi.org/10.1016/j.nme.2016.04.003.
[10] O.V. Ogorodnikova, J. Roth, M. Mayer, J. Appl. Phys. 103 (2008) 034902.
[11] O. Ogorodnikova, J. Roth, M. Mayer, J. Nucl. Mater. 373 (2008) 254–258.
[12] D. Terentyev, G. De Temmerman, B. Minov, Y. Zayachuk, K. Lambrinou, T.W. Morgan, A. Dubinko, K. Bystrov, G. Van Oost, Nucl. Fusion 55 (2015) 013007.
[13] D. Terentyev, G. De Temmerman, T.W. Morgan, Y. Zayachuk, K. Lambrinou, B. Minov, A. Dubinko, K. Bystrov, G. Van Oost, J. Appl. Phys. 117 (2015) 083302.
[14] V.K. Alimov, J. Roth, Phys. Scr. T128 (2007) 6–13.
[15] I. Uytdenhouwen, M. Decreton, T. Hirai, J. Linke, G. Pintsuk, G. Van Oost, J. Nucl. Mater. 363–365 (2007) 1099–1103.
[16] P. Hirsch, A. Howie, R. Nicholson, D.W. Pashley, M.J. Whelan, Microscopy of Thin Crystals, Krieger Publishing Company Malabar, Florida, 1977.
[17] H. Sheng, G. Van Oost, E. Zhurkin, D. Terentyev, V.I. Dubinko, I. Uytdenhouwen, J. Vleugels, J. Nucl. Mater. 444 (2014) 214–219.
[18] G.J. van Rooij, V.P. Veremiyenko, W.J. Goedheer, B. de Groot, A.W. Kleyn, P.H.M. Smeets, T.W. Versloot, D.G. Whyte, R. Engeln, D.C. Schram, N.J.L. Cardozo, Appl. Phys. Lett. 90 (2007).
[19] G. De Temmerman, et al., Nucl. Fusion 51 (2011) 073008.
[20] H. van der Meiden, R. Al, C. Barth, A. Donee, R. Engeln, W. Goedheer, Rev. Sci. Instrum. 79 (2008) 013505.
[21] Y.Z. Jia, G. De Temmerman, G.N. Luo, H.Y. Xu, C. Li, B.Q. Fu, W. Liu, J. Nucl.

Mater. 457 (2015) 213–219.
[22] L. Buzi, G. De Temmerman, B. Unterberg, M. Reinhart, T. Dittmar, D. Matveev, C. Linsmeier, U. Breuer, A. Kreter, G. Van Oost, J. Nucl. Mater. 463 (2015) 320–324.
[23] K. Heinola, T. Ahlgren, J. Appl. Phys. 107 (2010) 113531.
[24] D.F. Johnson, E.A. Carter, J. Mater Res. 25 (2010) 315–327.
[25] R. Frauenfelder, J. Vac. Sci. Technol. 6 (1968) 388–397.
[26] P. Grigorev, D. Terentyev, V. Dubinko, G. Bonny, G. Van Oost, J.M. Noterdaeme, E.E. Zhurkin, Nucl. Instrum. Meth B 352 (2015) 96–99.
[27] P. Grigorev, L. Buzy, A. Bakaeva, D. Terentyev, G. De Temmerman, G. Van Oost, J.M. Noterdaeme, Phys. Scr. T167 (2016) 014039.
[28] Y. Zayachuk, A. Manhard, M.H.J. t'Hoen, W. Jacob, P.A.Z. van Emmichoven, G. van Oost, Nucl. Fusion 54 (2014) 123013.
[29] G. Bonny, P. Grigorev, D. Terentyev, J. Phys-Condens Mat. 26 (2014).

Paper 2

Impact of plastic deformation on plasma induced damage and deuterium retention in tungsten

A. Bakaeva, D. Terentyev, A. Dubinko

MRS Advances

Volume 2, Issue 55 (2017) Pages 3347-3352

MRS Advances © 2017 Materials Research Society
DOI: 10.1557/adv.2017.428

Impact of plastic deformation on plasma induced damage and deuterium retention in tungsten

A. Bakaeva[1,2], D. Terentyev[1], A. Dubinko[1,2]
[1]Structural Materials Group, Institute of Nuclear Materials Science, SCK·CEN, Mol, 2400, Belgium
[2]Department of Applied Physics, Ghent University, St. Pietersnieuwstraat 41, 9000 Ghent, Belgium

ABSTRACT

Recent theoretical and subsequent experimental studies suggest that the uptake and release of deuterium (D) in tungsten (W) under high flux ITER-relevant plasma exposure is controlled by dislocation microstructure. Thanks to numerical calculations, a comprehensive mechanism for the nucleation and growth of D bubbles on dislocation network was proposed. The process of bubble nucleation can be described as D atom trapping at a dislocation line, its in-core migration, the coalescence of several D atoms into a multiple cluster eventually transforming into a nano-bubble. This view implies that the initial microstructure might be crucial for D uptake and degradation of the sub-surface layer under prolonged plasma exposure. In this work, we apply several experimental techniques to investigate the microstructure and mechanical properties of surface and sub-surface layer of W in recrystallized and plastically-deformed condition exposed to the high flux plasma. We use transmission and scanning electron microscopy, thermal desorption spectroscopy as well as nano-indentation measurements.

INTRODUCTION

Hydrogen embrittlement is a fundamental problem in modern solid state physics, the recognition of which drives research activities in steel and energy industries. Four general mechanisms behind hydrogen embrittlement are identified: (i) formation of a hydride phase, (ii) modification of local plasticity, (iii) grain boundary de-cohesion, and (iv) blister/bubble formation (see [1,2] and refs. cited therein). Importantly, possible synergy of those mechanisms may enhance the embrittlement effect. A good example of such synergy is the plasma-wall interaction (PWI) process in controlled fusion devices (such as ITER, see [3] and refs. cited therein), where PWI materials face simultaneously intense heat and particle fluxes from the fusion plasma. In such severe service conditions the plasma-facing materials (PFM) experience both oscillating thermal stresses (because of the plasma instability) and gas diffusion. The retained hydrogen isotopes accumulate on microstructural defects such as dislocations and grain boundaries [4] and naturally suppress the ability of the material to relieve thermal stress by plastic deformation.

Current theories on H permeation and diffusion [4-7] still lack a comprehensive atomistic-based mechanism that could account for H retention under sub-threshold plasma exposure conditions, where the imparted kinetic energy of H is too low to produce stable Frenkel pairs. A new mechanism providing a good quantitative description of H retention based on dislocation trapping has been recently proposed [8]. Although the model provides a good agreement with experiments for the deposition of H isotopes in stress-free W, the underlying mechanisms should be validated also for the material under stress, as it will occur under operation due to the transient modes induced by plasma instability [9].

Here, we report experimental results obtained by different techniques revealing the microstructure and mechanical properties of surface and sub-surface layer of W exposed to the high flux plasma. In particular, we use transmission and scanning electron microscopy (TEM), as well as nano-indentation (NI) measurements. To reveal the impact of the initial

microstructure on the storage of deuterium and microstructural damage induced by plasma. The exposures were performed using recrystallized and plastically deformed polycrystalline of commercially pure tungsten material.

EXPERIMENTAL DETAILS

The pristine material was recrystallized polycrystalline W of 99.99% purity, provided in rod form by Plansee AG[10]. The annealing was performed at 1600°C for 1 hour. A number of flat tensile samples were cut from the middle of the rod to perform tensile deformation at 600°C with deformation rate of 0.2 mm/min to induce the total strain of 20%. Then, the samples for plasma exposure were prepared from the gauge section of the homogenously deformed tensile sample, which was cut in several square pieces of 10×10×1 mm³ size.
The microstructure of the as-received (henceforth REF) and plastically deformed (henceforth DEF) samples was inspected by electron back scattering (EBSD) techniques and TEM (see Fig.1a). REF material has grains of uniform shape with a size varied in a range 50-150 μm. TEM revealed the presence of subgrains of size 2.5-5 μm, mainly connected by low angle grain boundary interfaces as shown in Fig.1a. The average dislocation density is calculated to be 2.8×10^{12} m^{-2}. The plastic deformation, applied to this material, was mainly expressed in the increase of the dislocation density, which appear a nearly homogenous pattern over grains and sub-grains. Dislocation networks contain both types of dislocations with Burgers vector of $a_0/2\langle111\rangle$ and $a_0\langle100\rangle$, and in some grains a dense tangle dislocation networks (with a significant presence of edge component) are found. The average dislocation density is about 3×10^{13} m^{-2}, but locally can go up to 10^{14} m^{-2}. The composite TEM image of the DEF sample is shown in Fig.2b. More discussions about TEM results can be found in [11].

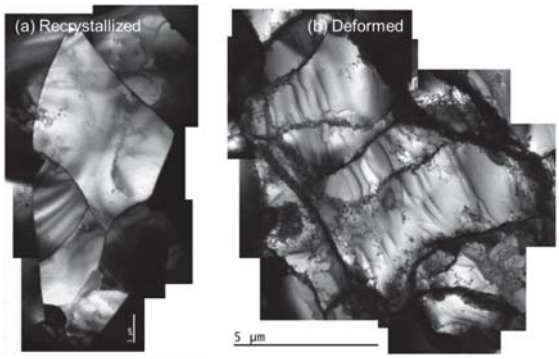

Figure 1. A composite TEM micrograph of the typical bulk microstructure of the (a) REF and (b) DEF material, see text for details.

Exposures using both REF and DEF samples were performed at the linear plasma generator Pilot-PSI [12], using the high-density low-temperature plasmas to mimic the conditions expected in the ITER divertor. The energy of deuterium ions was around 50 eV, while it should exceed 900 eV to initiate atomic displacement in W. A relatively small sample surface ensured a limited temperature variation across the surface (200±10°C) during the 70-seconds exposure, as measured by an infra-red camera (FLIR A645 sc). 10 and 70 seconds exposures were applied as a single shot. 490 sec exposure was as a sequence of 7 shots of 70 seconds

each. The plasma temperature and density were respectively 0.8 eV and 1.6E+20 m^{-3}. The particle flux in the centre of the sample in both cases was in the range (0.8-1.0)×10^{24} m^{-2} s^{-1}, calculated using plasma electron density and electron temperature, as measured by Thomson scattering [13] at a distance of ~25mm upstream from the plasma-facing surface. Special care was taken to perform all exposures at as identical conditions as technically achievable as well as to perform thermal desorption spectroscopy (TDS) in one week after the exposure to be consistent with our previous works on different W grades [14]. Those works revealed very good reproducibility of the TDS spectrum in sequential campaigns.

The surface of the exposed samples was inspected by scanning electron microscopy (SEM) prior to TDS. The TDS measurements used a temperature ramp of 0.5 K/s up to 1000°C K. The D_2 and HD molecule release flux was measured by a quadrupole mass spectrometer. Technical parameters and experimental details are identical to those presented in our earlier work [15].

To clarify the impact of the plasma exposure on the surface hardness, a set of nano-indentation measurements was performed. The samples were tested using an Agilent G200 nano-indenter to measure the Young's modulus and surface hardness. The indentation measurements were performed in continuous stiffness mode (CSM) [16] with the standard XP head equipped with a Berkovich diamond tip. The oscillation amplitude and frequency were respectively 2 nm and 45 Hz. The indentation strain rate was set to 0.05 s^{-1} and the specimens were indented down to a penetration depth h_{NI}=1.5 µm. Two zones on the exposed sample were investigated by performing 25 indents spaced by 60 µm for each zone. The hardness was calculated using the classical Oliver & Pharr method [16].

RESULTS AND DISCUSSION

The SEM micrographs of the REF and DEF samples are shown in Fig. 2 (a) and (b), respectively, for fluence of 5×10^{25} m^{-2} (i.e. 70 sec exposure). Both, blister-rich and blister-depleted zones have been clearly identified in the REF sample (see Fig.3 c and d). Heterogeneous distribution of blisters is in agreement with other studies employing recrystallized W [15]. The inspection of the deformed W sample revealed a significantly more uniform blister distribution and absence of blister-free zones, when compared to the recrystallized sample. The blisters in the DEF sample were more numerous and smaller in size, with a particular feature identified over the entire exposed surface - the presence of small holes on the blisters caps. Nearly every well-defined blister exhibited this feature, as shown more clearly by the magnified inset of Fig. 2c. Given that the SEM images were taken using a secondary electron detector, it is quite easy to identify these features as holes, based on the pronounced contrast between the edge of the hole (appearing as a bright rim) and the hole itself (appearing as a dark dot). It is concluded that most of blisters burst open, probably due to the gas pressure exceeding the strength of the blister cap.

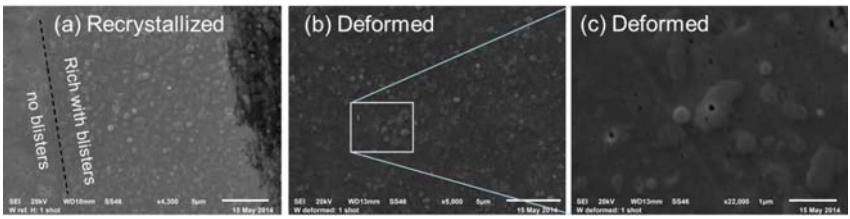

Figure 2. SEM images of plasma-exposed W samples: (a) Reference; (b) Deformed; (c) zoomed area showing ruptured blisters. The image is taken after TDS is done.

Variations in blister density in REF sample is associated with the lattice orientation of surface grains, whereby (111)-oriented grains are most susceptible to blistering [17]. The blisters observed under high flux plasma exposure are so called "high dome" blisters, which result from the plastic deformation and slip induced by the gas pressure [18]. Intensive blistering of (111)-oriented grains can explained by preferential slip of the dislocations, whose slip generates the observed high dome blisters, attracted by the open surface. To clarify whether the heterogeneous pattern of blisters also produces non-uniform change in mechanical properties we perform NI measurements combined with EBSD mapping.

The area selected for the NI was scanned by EBSD, which is shown in Fig.3(a). Traces of the indents are evident, and the results of the NI measurements were grouped depending on the grain orientation. It was possible to single out the indents performed in the grains with {111}, {112} and {101} orientations. The evolution of the hardness as a function of the indentation depth, obtained by averaging the results for each particular grain orientation (over about 5-8 indents per grain), is presented in Fig.3(b). The saturated hardness at a depth of 1.5 μm reaches 6±0.1 GPa, which is in good agreement with 6 GPa and 5.6 GPa reported by Armstrong et.al. [19] and by Zhang et.al. [20] for recrystallized polycrystalline W. This shows that the plasma-damaged area does not spread inside the material deeper than few tens of μm. On the other hand, one can see that the averaged curves for the three grains converge at the indentation depth of 400-500 nm. Below this depth, the hardness in the {111} grain is clearly lower than in the other two grains. At this point, we do not have a clear explanation of this effect, but it could related to the variation in the storage of plasma damage, as also expressed by heterogeneous distribution of blisters, see examples in Fig.3 (c,d). Similar NI measurements are planned to be performed on the DEF exposed sample.

Coming back to the features identified by SEM in the DEF samples, i.e. blisters with punched caps, we present TDS measurements done to clarify impact of plastic deformation on the deuterium release. The TDS spectra for both samples are presented in Fig. 4a. The spectrum of the REF sample reveals two distinct peaks at 525 K and 800 K, in agreement with earlier studies employing similar plasma exposure conditions (see e.g. [15]). At the accumulated dose, the intensity of the first peak should prevail over the blistering peak [15], which was also experimentally confirmed here. However, the TDS spectrum of the DEF sample exhibits a single major peak at 525 K. The intensity of this peak, generically associated with the dislocation microstructure (e.g. see [21]), is by a factor of two higher in the DEF W sample as compared to REF sample. This is consistent with the fact that the dislocation density is much higher in the DEF sample. A minor recovery stage can also be seen on the both spectra as a 'shoulder' around 600-650 K, which could be attributed to the trapping at grain boundaries. The intensity and position of this stage does not differ essentially in the two samples.

Despite the absence of the second peak in the deformed sample, one can distinguish a shallow plateau around 750-850 K, which might be attributed to a weak signal corresponding to gas release from the bubbles. Obviously, the intensity of this release is much smaller than the release from the bubbles in the recrystallized W. Therefore, one may make the reasonable assumption that the small holes found by SEM are indeed a sign of ruptured blisters, which released most of their gas content during the plasma exposure.

Even though some of the blisters in DEF sample were ruptured, the calculation of the total retention (D_2 signal) shows that heavy plastic deformation increases the retention. The integral retention in REF and DEF samples is compared in Fig.4b. Obtained results suggest that the retention in both samples is not yet saturated, and DEF contains nearly 50% more retained deuterium. Clearly, the high density of dislocations originating from the plastic deformation enhances the retention in the currently explored exposure conditions.

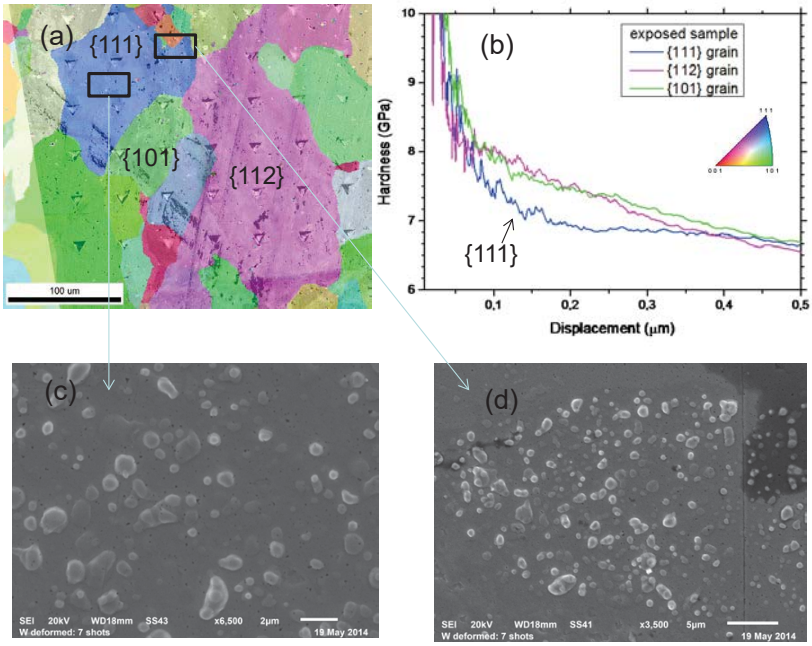

Figure 3. (a) Electron backscattering diffraction inverse pole figure maps of the REF sample exposed to plasma after nano-indentation; (b) Hardness depth profile measured by nano-indentation in the exposed REF sample; (c) and (d) SEM micrographs showing blister-rich and blister-free zones in the REF sample. Exposure fluence was of 5×10^{25} m^{-2}.

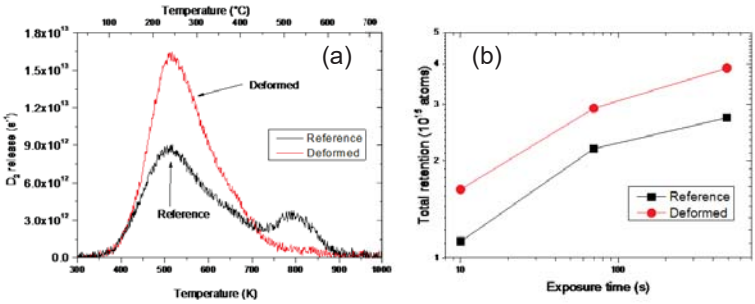

Figure 4. (a) TDS spectra of the reference and deformed samples exposed to a fluence of 5×10^{25} m^{-2} i.e. 70 sec plasma shot. (b) Deuterium retention in the reference and plastically deformed samples as a function of the exposure time.

CONCLUSIONS

We have performed dedicated plasma exposures on commercially pure W, using recrystallized and plastically-deformed samples. Controlled plastic deformation by uniaxial tensile load was applied to the recrystallized material to increase dislocation density by one order of magnitude without modifying other microstructural features (i.e. grain and sub-grain size). Recrystallized W samples in the annealed and plastically deformed state were exposed to D fluence up to 8×10^{24}, 5×10^{25} and 3.5×10^{26} D/m^2.

SEM imaging of the exposed samples revealed that almost all visible blisters in the deformed samples are ruptured, unlike in the recrystallized samples. The gas release spectrum of the deformed samples confirmed the absence of the stage corresponding to gas release from bubbles. In the range of the studied fluence, plastic deformation increases the total D retention by ~50%, as compared to the reference recrystallized sample.

At the same time, the nano-indentation testing applied to the recrystallized sample demonstrated that grains with (111) orientation exhibit different hardness as compared to other high-index oriented grains. This observation is line with the heterogeneous distribution of blisters identified by SEM in the same sample in the NI measured area.

ACKNOWLEDGEMENTS

This project was carried out with financial support from FOD (Belgium). The work was partially supported by the funding received from the Euratom research and training programme 2014-2018 under grant agreement No 633053 (EUROfusion/Enabling Research programme).

References

1. S.M. Myers, M.I. Baskes, H.K. Birnbaum, J.W. Corbett, et al. *Rev. Modern Physics* **64**, 559 (1992).
2. M. Daw and M. Baskes. *Phys. Rev. Lett.* **50**, 1285 (1983).
3. S. Matsuda and K. Tobita. *Journal of Nucl. Sci. Tech.* **50**, 321 (2013).
4. D.F. Johnson and E.A. Carter. *J.Mater.Res.* **25**, 315 (2010).
5. K. Heinola, T. Ahlgren, K. Nordlund and J. Keinonen. *Phys. Rev. B* **82**, 094102 (2010).
6. R. Difoggio and R. Gomer. *Phys. Rev. Lett.* **44**, 1258 (1980).
7. T. Ahlgren, K. Heinola, K. Vortler and J. Keinonen. *J. Nucl. Mater.* **427**, 152 (2012).
8. D. Terentyev, V. Dubinko, A. Bakaev, Y. Zayachuk, W. Van Renterghem and P. Grigorev. *Nuclear Fusion* **54**, 042004 (2014).
9. G. Pintsuk. *Comprehensive Nuclear Materials* **4**, 551 (2012).
10. I. Uytdenhouwen, M. Decreton, T. Hirai, J. Linke, G. Pintsuk and G. Van Oost. *J. Nucl. Mater.* **363-365**, 1099 (2007).
11. D. Terentyev, X.Z. Xiao, A. Dubinko, A. Bakaeva and H.L. Duan. *J. Mech. Phys. Solids* **85**, 1 (2015).
12. G.J. van Rooij, V.P. Veremiyenko, W.J. Goedheer, B. de Groot, et al. *Appl. Phys. Lett.* **90** (2007).
13. H. van der Meiden, R. Al, C. Barth, A. Donee, R. Engeln and W. Goedheer. *Rev. Sci. Instrum.* **79**, 013505 (2008).
14. Y. Zayachuk, M.H.J. 't Hoen, P.A.Z. van Emmichoven, I. Uytdenhouwen and G. van Oost. *Nuclear Fusion* **52**, 103021 (2012).
15. Y. Zayachuk, M.H.J. 't Hoen, P.A.Z. van Emmichoven, D. Terentyev, I. Uytdenhouwen and G. van Oost. *Nuclear Fusion* **53**, 013013 (2013).
16. W. Oliver and G. Pharr. *J Mater Res* **19**, 3 (2004).
17. W.M. Shu, E. Wakai and T. Yamanishi. *Nuclear Fusion* **47**, 201 (2007).
18. C.H. Skinner, A.A. Haasz, V.K. Alimow, N. Bekris, et al. *Fusion Science and Technology* **54**, 891 (2008).
19. D.E.J. Armstrong, P.D. Edmondson and S.G. Roberts. *Applied Physics Letters* **102** (2013).
20. Z.X. Zhang, D.S. Chen, W.T. Han and A. Kimura. *Fusion Engineering and Design* **98-99**, 2103 (2015).
21. O.V. Ogorodnikova, J. Roth and M. Mayer. *J Appl. Phys.* **103**, 034902 (2008).

Paper 3

Impact of plastic deformation on retention under pure D or He high flux plasma expose

A. Bakaeva, D. Terentyev, T.W. Morgan, A. Dubinko, W. van Renterghem, L. Tanure, K. Verbeken

Nuclear Materials and Energy

Volume 15 (2018) Pages 48–54

Nuclear Materials and Energy 15 (2018) 48–54

Contents lists available at ScienceDirect

Nuclear Materials and Energy

journal homepage: www.elsevier.com/locate/nme

Impact of plastic deformation on retention under pure D or He high flux plasma expose

A. Bakaeva[a,b], D. Terentyev[a,*], T.W. Morgan[c], A. Dubinko[a], W. van Renterghem[a], L. Tanure[c,d], K. Verbeken[d]

[a] SCK•CEN, Nuclear Materials Science Institute, Boeretang 200, 2400 Mol, Belgium
[b] Department of Applied Physics, Ghent University, St. Pietersnieuwstraat 41, 9000 Ghent, Belgium
[c] FOM Institute DIFFER, De Zaale 20, 5612 AJ Eindhoven, The Netherlands
[d] Department of Materials, Textiles and Chemical Engineering, Ghent University (UGent), Technologiepark 903, B-9052 Ghent, Belgium

ARTICLE INFO

Keywords:
Tungsten
He-H exposure
High flux plasma
Deformation

ABSTRACT

The retention of deuterium (D) and helium (He) is studied in pure tungsten after high flux mono-plasma exposure. The recrystallized and plastically deformed tungsten samples are studied to clarify the impact of the material microstructure, in particular dislocation density, on the trapping and release of D and He. Thermal Desorption Spectroscopy (TDS) measurements are performed to reveal the release stages and quantify the retention. Preliminary transmission electron microscopy study was applied to clarify the microstructural modifications induced by the plasma exposure to support the discussion and conclusions. It has been demonstrated that plastic deformation causes considerable suppression of He release within the explored limit of the TDS temperature – 1300 K. This is opposite to what is found for the pure D exposure, where the plastic deformation evidently enhances the D retention, given equivalent exposure conditions in terms of surface temperature and ion fluence.

1. Introduction

Due to a number of unique properties, tungsten is considered as the plasma-facing material for the ITER divertor and DEMO first wall [1]. Interaction of tungsten with fusion-relevant plasma ions, such as deuterium, tritium and helium, causes modifications in the surface microstructure (e.g. blistering, swelling, etc.) as well as in its mechanical properties (e.g. increased hardness, appearance of micro-cracks). This originates from the penetration of the gaseous atoms inside the material, the formation of bubbles and local plastic deformation, induced by thermal stresses. The impact on the microstructural changes is defined by the irradiation conditions (see e.g. [2]) and initial microstructural state. Overall, a plasma facing material will undergo modification of its initial properties due to the accumulation of gas atoms in the sub-surface region (see [3] for a recent overview) and lattice defects. In addition to the ion-driven plasma exposure, the plasma surface material/component will be a subject to cyclic thermal loading and neutron irradiation [4]. These processes will cause the plastic deformation and generation of lattice defects such as voids and dislocation loops [5]. To project how the plasma-material interaction will undergo in the material subjected to considerable plastic deformation, it is important to perform comparative study engaging reference and plastically deformed material to clarify possible impact of the plastic deformation with respect to the total retention and kinetics of the release of plasma components.

Our earlier works were dedicated to investigation of the impact of plastic deformation on the retention and release under pure D exposure [6-8] in the ITER specification tungsten subjected to recrystallization at 1600C (referred to “reference material” in this work). It has been generally concluded that under low temperature exposure conditions (i.e. below 600 K) a dislocation network facilitates the nucleation of defects and thereby enhances the trapping of D. Overall, this leads to an increase in D retention seen as amplification of the release stages on the thermal desorption spectrum (TDS), however the positions of the stages do not shift remarkably, implying that similar types of traps operate in the plastically-deformed material.

As of now, there is no experimental information reporting the impact of the plastic deformation on the He trapping and release. Most of the studies were performed to understand the impact of He seeding in the mixed exposures or influence of He energy, flux and fluence. Alimov et al. performed TDS analysis after high flux helium-seeded plasma exposures of recrystallized pure W (ALMT grade) [2]. The energies of D

* Corresponding author.
E-mail address: dterenty@sckcen.be (D. Terentyev).

https://doi.org/10.1016/j.nme.2018.05.014
Received 14 January 2018; Received in revised form 8 May 2018; Accepted 16 May 2018

and He ions were fixed at 38 eV and 76 eV, respectively. The TDS analysis revealed three major release stages at 550 K, 650 K and 800 K. Seeding of He ions into the plasma at exposure temperatures below 350 K did not change strongly the D retention, while at temperatures above 400K the D retention decreases significantly compared to that for the pure D plasma exposure. This was taken as an argument indicating that He seeding results in the confinement of D retention in the subsurface region preventing long range diffusion. With respect to He retention itself, it was found not to depend on the He ion concentration in the D plasma. He retention was seen to increase with the exposure temperature from about 2×10^{19} He·m^{-2} at 340 K up to about 3×10^{20} He·m^{-2} at 810 K. This was interpreted as thermally activated diffusion, which apparently is enhanced above 550-650 K, being the temperature of the release stage of He as measured by TDS.

Baldwin et al. and Finlay et al. [9, 10] also studied He retention under mixed D-He plasma and dual beam ion exposures, respectively. Several important results were demonstrated by Finlay et al.[10]. The addition of 3% He in the ion flux reduces D retention at 300 and 500 K for all probed He/D ion range ratios. He retention is affected by ion energy and temperature, but not by He-to-D ratio. The release peak of D, located around 500K, slightly shifts towards lower temperature due to the addition of He in the plasma, which is probably due to the modification of the binding energy profile in the mixed He-D-vacancy clusters. It was also noted, in line with earlier experiments, that the addition of He greatly decreases D diffusion and increases D trapping up to 1 μm depth, similar to the results reported in [2, 11]. Comparison of D and He depth profiles obtained by NRA showed that addition of He apparently reduces D diffusion and enhances its trapping in a region that extends ~1 μm deeper than the He layer detected. This suggests that the stress field, created by the He bubbles [12], extends much further than the layer of high He concentration.

Yajima et al. [13] has performed in-situ transmission electron microscopy (TEM) analysis to explore features of He trapping and release and related them to TDS measurements. Pure W (recrystallized) was exposed to the high flux He plasma to simulate ITER divertor conditions. Three major peaks around 550 K, 800 K and 1400 K were identified by TDS. The TEM measurements done using the same heating ramp reported that the major part of He bubbles was observed directly after exposure, while under the annealing, almost all bubbles disappeared before the temperature of 1200 K was reached. Hence, the release peak around 1400 K could be attributed to the deep diffusion of He and diffusion controlled (accounting for the re-trapping at the subsurface) release at high temperature.

In this work, we continue our investigation of the effect of plastic deformation on the retention and release of plasma components. In particular, we perform plasma exposure using pure He at temperature of 480 K, and exactly the same W samples, as in our previous works [6-8] done for pure D exposures, to ensure full consistency. The TDS and TEM measurements are provided to make one-to-one comparison between pure D and pure He exposure and clarify the impact of the plastic deformation.

2. Experimental details

Polycrystalline W with purity of 99.99%, provided by Plansee AG was used in this study and in our previous works details on impurities and microstructure could be found [7, 14]. Reference material (REF) represents itself W rod recrystallized at 1873 K for 1 hour. The microstructure of REF sample consisted of randomly oriented grains, separated mainly by high-angle grain boundaries, with a grain size was in the range of 50-150 μm, as shown in Fig. 1(a). The dislocation density is measured by TEM to be (2-4) $\times 10^{12}$ m^{-2}, and typical images of the sub-grains and dislocation lines resolved by TEM are shown in Fig. 2 (a,b).

Plastic deformation was applied by performing tensile loading at 873K in air with a deformation rate of 0.2 mm/min to reach 28% deformation, which approximately corresponds to the ultimate tensile strength of the studied W grade at 873 K (after recrystallization). The microstructure of both REF and plastically-deformed (PD) samples was studied using Scanning Electron Microscopy (SEM) by electron back

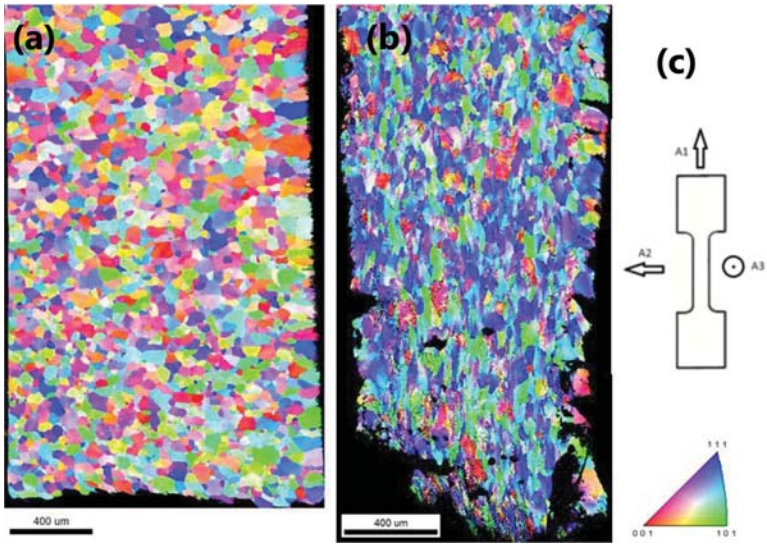

Fig. 1. Inverse polar figure map of the EBSD scan of the (a) REF and (b) DEF samples. A sketch in fig. c shows the tensile sample and direction of the loading applied. On the schematic figure on the right hand side, direction A1 shows the deformation axis, A3 – normal to the EBSD scan.

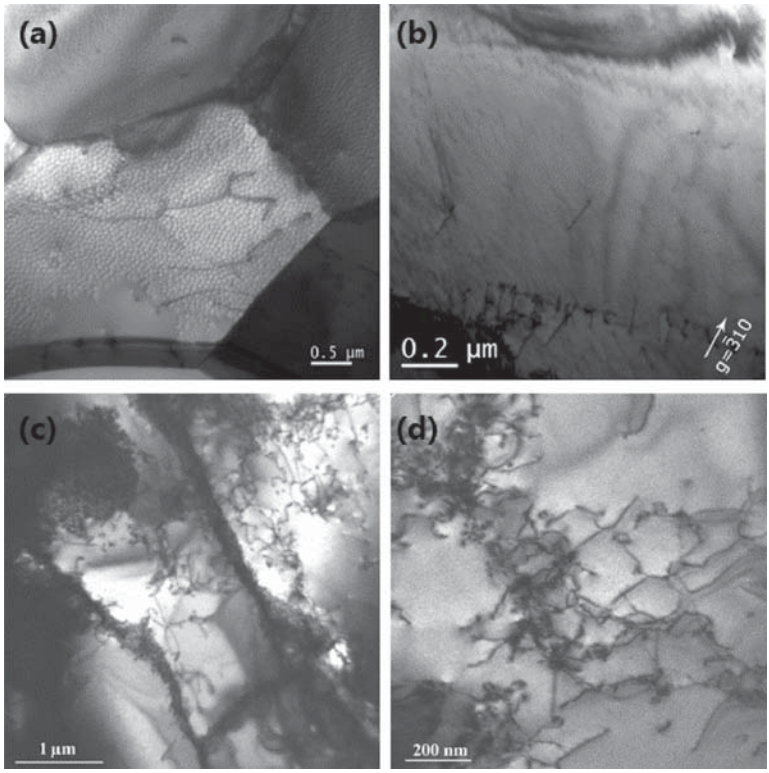

Fig. 2. TEM dark field images of (a,b) REF and (c,d) PD samples in the non-exposed condition. The images are taken to demonstrate the sub-grain structure (a,c) and appearance of dislocation lines inside the grains (b,d).

scattering diffraction (EBSD) analysis. Examples of EBSD inverse polar maps before and after the deformation are given in Figs. 1(a) and (b), respectively. Grains become elongated in accordance with the orientation of the sample with respect to the tensile loading direction, the mean size reduces to 25-80 μm range. The impact of the plastic deformation on the TEM-visible microstructure is shown in Fig. 2 (c,d).

TEM samples were extracted from the middle of the deformed specimen and TEM samples were prepared in the same conventional way as described in details in our previous works [15-17]. The specimens were investigated by means of a JEOL 3010 TEM operating at 300 kV. It has been revealed that after plastic deformation, dislocations became evident everywhere in the sample's visible area. The resulting dislocation density in the PD sample was found to be about 2×10^{14} m^{-2}, i.e. nearly two orders of magnitude higher than that in the REF sample. The dislocation density was measured by counting the number of intersections with dislocation lines made by random strips drawn on micrographs. To ensure adequate comparison of different sub-surface layers, most of the micrographs are oriented with the primary <111> slip directions pointing to the top of the page. The same method was applied to characterise the dislocation density in the plasma-exposed samples.

Exposures to deuterium plasma were performed at the linear plasma generator Pilot-PSI [18], employing a high-density plasma mimicking the 'sub-displacement threshold' plasma-wall interaction conditions expected in the ITER divertor. The energy of the deuterium ions was about 50 eV (controlled by negatively biasing the target), while energies in excess of 900 and 450 eV are required to initiate atomic displacement in W for D and He respectively. Although the plasma beam is non-uniform, the size of the sample corresponded to the full width at half maximum, i.e. 10 mm, which ensured limited temperature and flux gradients across the surface during the exposure, as was measured and confirmed in-situ by an infra-red camera (FLIR A645 sc). The parameters of the exposure are provided in Table 1. The flux was calculated

Table 1
Summary of exposure conditions and parameters.

Material (REF/PD)	He /D	Flux (ions/m^2/s)	Fluence (ions/m^2)	Time (sec)	Temperature (K)
REF	D	1E+24	4.9E+26	490	470
PD	D	1E+24	4.9E+26	490	470
REF	He	2.1E+24	6.3E+26	300	480
PD	He	2.0E+24	6E+26	300	480

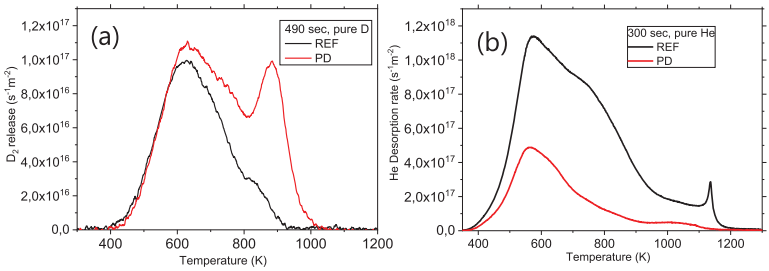

Fig. 3. Comparison of TDS spectra after pure D (a) and pure He (b) exposure of both reference and plastically-deformed samples. Reference sample is labeled as REF, plastically deformed sample is labeled as PD. The results for pure D exposure were published in [7].

from the plasma electron density and electron temperature, as measured by Thomson scattering [19] at a distance of around 25 mm upstream from the plasma-facing surface. Special care was taken to perform all exposures as close as possible to 480 K temperature to remain consistent with our previous studies [6, 7, 20]. Pilot PSI is one of few unique machines which provides an ultra-high flux (up to 10^{24} particles/m^2/s) and hence high power beam which makes it more difficult to precisely control the surface temperature and some variation can occur due to extremely small differences in sample clamping, sample thickness, plasma conditions, etc. That is why, in the case of He exposures the surface temperature was slightly different from that of D exposers. However, the difference of 10K should not impact the conclusions.

After the exposure, TDS was applied to measure the release of He and D in the tungsten samples. The maximum temperature under TDS cycle was 1273 K, the heating rate used was 0.5 K s^{-1} and the holding time at the maximum temperature was 5 min. The release flux of molecular HD and D_2 and He was measured by the quadruple mass spectrometer (QMS). Quantification of the mass four signal (corresponding to the release of D_2 or He) was performed using a calibrated D_2 and He leak. The temperature-dependent deuterium release spectra were analysed on the basis of the standard Gaussian distribution function:

$$I \times \exp\left(-\frac{(T - T_m)^2}{2\sqrt{2\ln(2)}\,\Delta T^2}\right) \quad (1)$$

where I denotes the peak intensity, T_m is the temperature position of the peak and ΔT is the full width at half maximum. Each raw TDS curve was fitted using a linear superposition of three Gaussian functions.

3. Results and Discussion

The TDS spectra measured for the REF and PD samples are shown in Fig. 3. One can clearly see that the integral retention after D exposure is enhanced by the plastic deformation, while the effect is opposite in the case of He exposure. In particular, it appears that plastic deformation defects enhance D retention in the TDS spectra after 600 K. The well-pronounced peak around 900K likely corresponds to the desorption of D from voids which is well known to occur in the temperature range of 800–1000 K (see e.g. [21]). In fact, the high temperature peak is also present in the reference material but it is not so highly pronounced in the current exposure conditions. The detailed study of the TDS spectra on the fluence and exposure temperature under pure D plasma exposure is reported in [7, 8].

In the case of He exposure, the reduction of the He retention is observed over the whole TDS temperature range and visually peak positions for the release do not change with the presence of plastic deformation. This observation suggests that the origin of defects in which He atoms are trapped is the same. The dislocation network, induced by the plastic deformation, clearly does not change the mechanism of trapping but affects its intensity. This can be linked to either the nucleation or growth rate of He bubbles being affected by a high density of dislocations. If one assumes that the dislocation network acts as channels for fast diffusion of He in and outside the bulk, the nucleation of He clusters in subsurface area would indeed be suppressed.

The Gaussian fit of the recorded spectra is given in Fig. 4. The symmetric Gaussian fit reasonably reproduces the TDS spectrum, except for a narrow spike around 1150K registered for He expose in REF sample. It should be noted that such sharp and narrow peaks were also registered in [13] for pure recrystallized tungsten, however, their origin was not discussed. It is reasonable to assume that such a sharp release could be induced by the migration of He bubbles, which in turn leads to an abrupt increase in the release rate, contrary to the more gradual atomic evaporation of He from the He bubbles.

All the spectra could be well fitted with three major release stages, whose characteristics are reported in Table 2. In the case of D exposure, the peaks are located around 600 K, 690-730 K and 840-880 K. In the case of He exposure, the peaks are located around 570 K, 750 K and 1020 K. The release stages after He plasma exposure, performed at 1300 K, are quite close to the results reported previously [13], but in this study the low temperature release stage is found around 330–350 K as reported by Yajima et al. [13]. This deviation might be attributed to the different exposure temperatures employed, which resulted in the formation of fuzz in the case of Yajima's experiment not observed in our study. The positions of the high temperature peaks, located in the range 800-1200K [10, 13], broadly agree with those observed in the present work.

Following the results presented in Table 2, we can state that indeed plastic deformation does not change the positions of the peaks measured in the He-exposed samples. As a result of the plastic deformation, the intensity of the first release peak decreases by a factor of two, for the second one – by a factor of three and for the third peak – by a factor of two. In the case of D-exposure, the applied plastic deformation mainly affected the intensity of the second and the third release stages.

Finally, we can mention that the release of D is completed within about 1000K, which is in general agreement with many previous studies done after pure D exposure (see introduction for references). Whereas, the release of He is very likely uncompleted, given the maximum TDS temperature applied here (being limited by technical capacity). Indeed, one should expect further release of He above 1300 K, and final conclusions can be done only by performing TDS up to 2000 K.

Based on the measured signals in the available TDS temperature range, the total retention in the REF and PD samples is compared in Fig. 5. The latter shows that plastic deformation suppresses the He retention by a factor of three. Keeping in mind that a fraction of He is very likely still retained, a reasonable explanation for the observed effect of the plastic deformation can be the process of backward diffusion of He

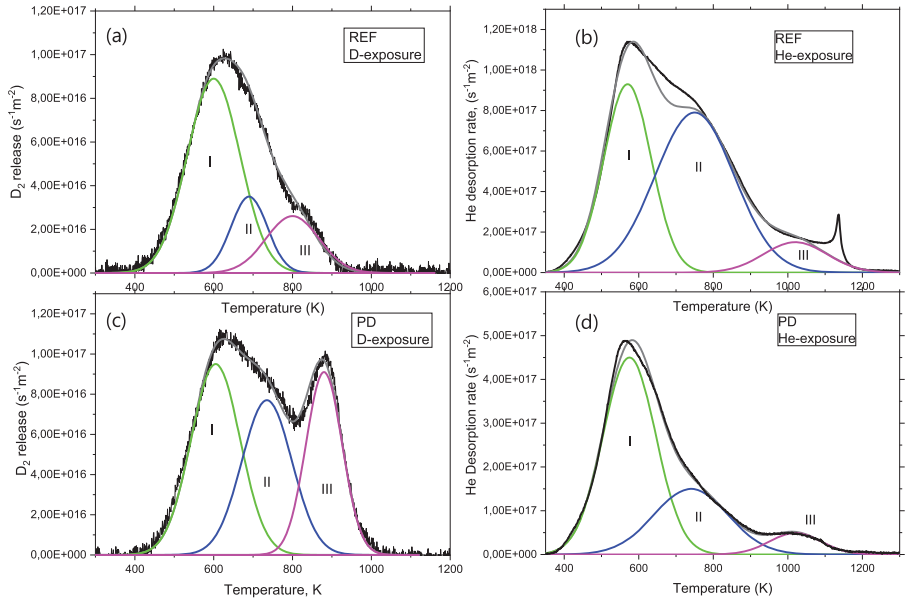

Fig. 4. Decomposition of TDS spectra on the sub-stages. (a,c) D-exposed samples, (b,d) He-exposed samples.

Table 2
Characteristics (temperature position/maximum intensity of the release, measured in particle/m^2) of the release peaks as deduced by the fitting of TDS spectra presented in Fig. 4.

Ion	Stage I	Stage II	Stage III
D Ref	600 K/ 8.9E16	690 K/3.5E16	840 K/2.3E16
He Ref	570 K / 9.3E17	753 K / 7.6E17	1020 K /1.5E17
D PD	607 K / 9.5E16	733 K/7.6E16	883 K/9E16
He PD	575 K / 4.5E17	745 K/1.5E17	1020 K / 5.1E16

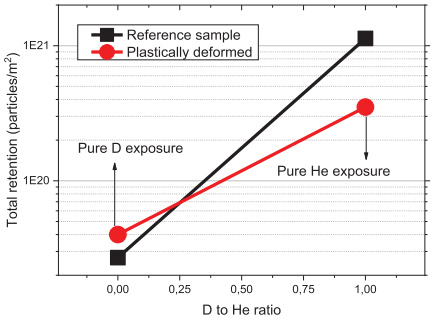

Fig. 5. Comparison of the release of D_2 and He calculated on the basis TDS measured spectra.

via dislocation lines, whose density is much higher in the PD sample. The enhanced diffusion via dislocation lines was at least found for hydrogen in W by means of atomistic calculations [22]. Unfortunately the first principle calculations were not performed for He-dislocation system in tungsten, up to our best knowledge. The presence of the dislocation networks may also suppress the self-trapping of He, which otherwise is considered to be the major mechanism leading to the formation of He-vacancy clusters and their further growth in the bubbles by punching self-interstitials in tungsten bulk (see review [23] and references sited therein). Another explanation could be an increased number density of He bubbles (due to enhanced growth of He bubbles on dislocations) near surface that also enhance backward diffusion. In the current experiment, the exposure conditions were too complicated to easily single out the main mechanism responsible for the observed effect.

In our earlier works, we have performed dedicated TEM analysis to investigate the incident exposed surface and sub-surface region to clarify how deep the plasma-induced microstructural modification penetrates the sample in the case of pure D exposure. In [15-17], it was found that the characteristic depth of the plasma-induced microstructural modification is about 10–15 μm only, and beyond that depth, the material recovers its initial microstructure. At this, the main impact of the plasma exposure on the microstructure is the strong increase in the dislocation density on the top surface (by two order of magnitudes), moderate increase within 1-5 μm range and restoration of the initial microstructure beyond 10 μm.

To clarify the impact of He exposure, we performed TEM analysis of the top surface and sub-surface region at a depth of 1-5 μm. The top surface samples were prepared by singe-side polishing (i.e. removing material from the un-exposed side), the others by standard double-side polishing. It found that acceptable quality of the TEM analysis could be not delivered for the single-side polished sample due to the strong

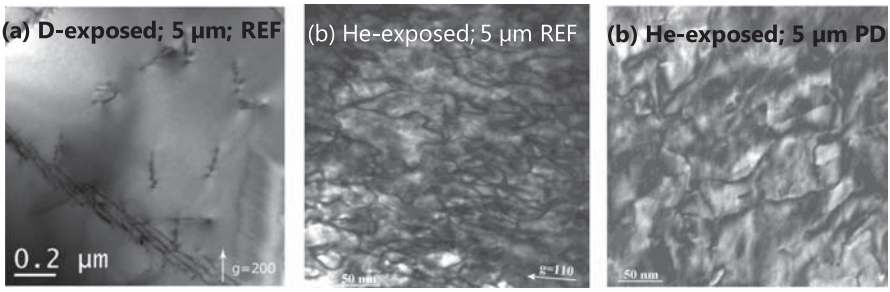

Fig. 6. TEM dark field images of the REF samples exposure to (a) D and (b) He, and (c) PD sample exposed to pure He plasma. The TEM samples were prepared to explore the microstructure at a depth of 3-5 μm below the plasma exposed surface. The dislocation density is measured to be about (2-4) × 10^{13} m^{-2} in D-exposed sample, and (1-2)) × 10^{15} m^{-2} in the He-exposed sample (for both REF and DP samples).

roughness of the exposed surface. This is in line with the well-known fact that He bubbles grow very close to the surface and therefore induce blistering and roughening of the surface. Thus, one-to-one comparison for the surface region could not be delivered. The examples of the TEM images in the sub-surface region of D and He exposed samples are provided in Fig. 6. The TEM analysis was performed for both REF and PD samples. For the D exposed sample, we found the increase of the dislocation density up to (2-4) × 10^{13} m^{-2} i.e. by about one order of magnitude as compared to the reference value. In the He-exposed samples, the increase of the dislocation density was much higher, and in the shown presented region the dislocation density reached a value of (1-2) × 10^{15} m^{-2}.

The complete TEM study of He-exposed samples is undergoing now. Due to the strong impact of He exposure on the surface roughness, it is impossible to apply the same methodology as was applied for pure D exposures in our earlier works. Thus, the preparation of the lamellas with the focus ion beam (FIB) is needed. To clarify the extension of the plasma-induced damage at a depth beyond 5 μm, we used FIB to fabricate the TEM lamella and make SEM scan provided in Fig. 7. Although the surface quality still requires improvement, it can be seen that grain refinement is evident in the sub-surface region with a depth of 1 μm or even less. This points to the fact that the top surface region is indeed heavily deformed (pattern of small sub-grains) while the region within next 10 μm is nearly free of the grain refinement. Thus, He exposure affects the material microstructure much stronger than D exposure, at least within the range of 5 μm from the surface.

4. Conclusions

We have performed a set of pure D and He high flux exposures at 470–480 K. The exposures were performed on the samples made of ITER specification tungsten provided by Plansee AG in the re-crystallized state and plastically deformed condition (28% deformation at 873 K). TDS and preliminary TEM measurements were performed to

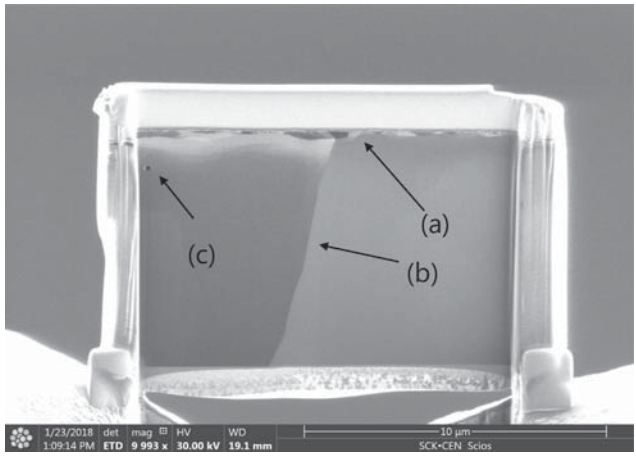

Fig. 7. FIB-cut TEM lamella extracted from the He-exposed REF sample, the image is recorded using the ion beam and it shows (a) plasma-exposed top surface where the grain refinement occurred; (b) grain boundary interface which goes along the whole sample; (c) cavity induced by the plasma exposure.

compare the effect of plastic deformation on the retention and release in the case of D and He exposure conditions. The release was measured by TDS up to 1300 K.

On the basis of the results presented and discussed above, we can summarize the following observations:

(i) In plastically deformed tungsten, three major release stages for He are observed just as in the reference recrystallized material. The positions of the peaks are the same in both types of samples but their amplitudes differ depending on the dislocation density of the material. The positions of the release peaks are in good agreement with the results previously published for pure He exposures. Overall, the plastic deformation reduces the total retention of He by a factor of three following the TDS measurements done up to 1300 K.
(ii) Preliminary TEM characterization performed for REF samples showed that in the sub-surface region He exposure induces much severe increase of the dislocation density as compared to the D exposure. Whereas the depth at which the microstructure recovers to the original bulk patter is similar in both He and D exposed samples, and this depth is about 15-20 μm.

Further study by applying high temperature TDS is needed to substantiate the conclusions regarding the outgassing of He. Earlier studies show clearly that He release may last up to 1600-1800 K. More in-depth TEM investigation is also needed before and after TDS to distinguish clearly the impact of exposure itself and possible annealing induced by the TDS cycle.

Acknowledgements

This work has been carried out within the framework of the EUROfusion Consortium and has received funding from the EURATOM research and training programme 2014-2018 under grant agreement No 633053. The views and opinions expressed herein do not necessarily reflect those of the European Commission.

Supplementary materials

Supplementary material associated with this article can be found, in the online version, at doi:10.1016/j.nme.2018.05.014.

References

[1] G. Pintsuk, Tungsten as plasma facing material, Compr. Nucl. Mater. 4 (2012) 551–581.
[2] V.K. Alimov, W.M. Shu, J. Roth, K. Sugiyama, S. Lindig, M. Balden, K. Isobe, T. Yamanishi, Surface morphology and deuterium retention in tungsten exposed to low-energy, high flux pure and helium-seeded deuterium plasmas, Physica Scripta (2009) T138.
[3] O.V. Ogorodnikova, Fundamental aspects of deuterium retention in tungsten at high flux plasma exposure, J. Appl. Phys. 118 (7) (2015) 074902.
[4] T. Hirai, S. Panayotis, V. Barabash, Use of tungsten material for the ITER divertor, Nucl. Mater. Energy 000 (2016) 1–7.
[5] A. Hasegawa, M. Fukuda, S. Nogami, K. Yabuuchi, Neutron irradiation effects on tungsten materials, Fus. Eng. Design 89 (7-8) (2014) 1568–1572.
[6] D. Terentyev, G. De Temmerman, B. Minov, Y. Zayachuk, K. Lambrinou, T.W. Morgan, A. Dubinko, K. Bystrov, G. Van Oost, Synergy of plastic deformation and gas retention in tungsten, Nuclear Fus. 55 (1) (2015) 013007.
[7] D. Terentyev, G. De Temmerman, T.W. Morgan, Y. Zayachuk, K. Lambrinou, B. Minov, A. Dubinko, K. Bystrov, G. Van Oost, Effect of plastic deformation on deuterium retention and release in tungsten, J. Appl. Phys. 117 (8) (2015) 083302.
[8] A. Bakaeva, D. Terentyev, G. De Temmerman, K. Lambrinou, T.W. Morgan, A. Dubinko, P. Grigorev, K. Verbeken, J. Noterdaeme, Dislocation-mediated trapping of deuterium in tungsten under high-flux high-temperature exposures, J. Nucl. Mater 479 (2016) 307–315.
[9] M.J. Baldwin, R.P. Doerner, W.R. Wampler, D. Nishijima, T. Lynch, M. Miyamoto, Effect of He on D retention in W exposed to low-energy, high-fluence (D, He, Ar), Mixture Plasmas vol 51, (2011) 103021Nuclear Fusion 51(12) (2011).
[10] T.J. Finlay, J.W. Davis, K. Sugiyama, V.K. Alimov, A.A. Haasz, Effects of D and He implantation depth on D retention in tungsten under simultaneous D-He ion irradiation, Physica Scripta T167 (2016) 014042.
[11] O.V. Ogorodnikova, T. Schwarz-Selinger, K. Sugiyama, V.K. Alimov, Deuterium retention in tungsten exposed to low-energy pure and helium-seeded deuterium plasmas, J. Appl. Phys. 109 (1) (2011) 013309.
[12] H.T. Lee, A.A. Haasz, J.W. Davis, R.G. Macaulay-Newcombe, Hydrogen and helium trapping in tungsten under single and sequential irradiations, J. Nucl. Mater. 360 (2) (2007) 196–207.
[13] M. Yajima, N. Yoshida, S. Kajita, M. Tokitani, T. Baba, N. Ohno, In situ observation of structural change of nanostructured tungsten during annealing, J. Nucl. Mater. 449 (1-3) (2014) 9–14.
[14] A. Dubinko, D. Terentyev, A. Bakaeva, K. Verbeken, M. Wirtz, M. Hernandez-Mayoral, Evolution of plastic deformation in heavily deformed and recrystallized tungsten of ITER specification studied by TEM, Int. J. Refract. Metals Hard Mater. 66 (2017) 105–115.
[15] A. Dubinko, D. Terentyev, A. Bakaeva, T. Pardoen, M. Zibrov, T.W. Morgan, Effect of high flux plasma exposure on the micro-structural and -mechanical properties of ITER specification tungsten, Nucl. Instrum. Meth. B 393 (2017) 155–159.
[16] A. Dubinko, D. Terentyev, A. Bakaeva, M. Hernandez-Mayoral, G. De Temmerman, L. Buzi, J.M. Noterdaeme, B. Unterberg, Sub-surface microstructure of single and polycrystalline tungsten after high flux plasma exposure studied by TEM, Appl. Surf. Sci. 393 (2017) 330–339.
[17] A. Dubinko, A. Bakaeva, M. Hernandez-Mayoral, D. Terentyev, G. De Temmerman, J.M. Noterdaeme, Microstructural modifications in tungsten induced by high flux plasma exposure: TEM examination, Physica Scripta (2016) T167.
[18] G.J. van Rooij, V.P. Veremiyenko, W.J. Goedheer, B. de Groot, A.W. Kleyn, P.H.M. Smeets, T.W. Versloot, D.G. Whyte, R. Engeln, D.C. Schram, N.J.L. Cardozo, Extreme hydrogen plasma densities achieved in a linear plasma generator, Appl. Phys. Lett. 90 (12) (2007) 121501.
[19] H. van der Meiden, R. Al, C. Barth, A. Donee, R. Engeln, W. Goedheer, Rev. Sci. Instrum 79 (2008) 013505.
[20] D. Terentyev, V. Dubinko, A. Bakaev, Y. Zayachuk, W. Van Renterghem, P. Grigorev, Dislocations mediate hydrogen retention in tungsten, Nuclear Fus. 54 (2014) 042004.
[21] H. Eleveld, A. van Veen, Void growth and thermal desorption of deuterium from voids in tungsten, J. Nucl. Mater. 212-215 (1994) 1421–1425.
[22] P. Grigorev, D. Terentyev, V. Dubinko, G. Bonny, G. Van Oost, J.M. Noterdaeme, E.E. Zhurkin, Nucleation and growth of hydrogen bubbles on dislocations in tungsten under high flux low energy plasma exposure, Nucl Instrum Meth B 352 (2015) 96–99.
[23] K.O.E. Henriksson, K. Nordlund, A. Krasheninnikov, J. Keinonen, The depth of hydrogen and hellium bubbles in tungsten: a compasiron, Fusion Sci.Technol. 50 (2006) 43–57.